

CRANFIELD UNIVERSITY

Khalifa Aliyu Ibrahim

Design and Performance Analysis of Concentrated Photovoltaic  
Cooling

Water, Energy and Environment  
Energy and Power

Masters by Research  
Academic Year: 2022 - 2023

Supervisor: Professor Patrick Luk  
Associate Supervisor: Professor Upul Kahagala Gamage  
January 2023

CRANFIELD UNIVERSITY

Water, Energy and Environment  
Energy and Power

Masters by Research

The Academic Year 2022 - 2023

Khalifa Aliyu Ibrahim

Design and Performance Analysis of Concentrated Photovoltaic  
Cooling

Supervisor: Professor Patrick Luk  
Associate Supervisor: Professor Upul Kahagala Gamage  
January 2023

© Cranfield University 2022. All rights reserved. No part of this  
publication may be reproduced without the written permission of the  
copyright owner.

## **ABSTRACT**

The use of solar energy as a global energy source has increased over the past two decades. Photovoltaic cells, which utilise the sun to generate electricity, are a promising alternative to fossil fuels that contribute to climate change. However, the high intensity of concentrated solar radiation can cause overheating in photovoltaic cells, reducing their efficiency and power output. Researchers worldwide are improving cooling in concentrated photovoltaic cells (CPV) to enhance temperature uniformity and improve power output. Previous studies have demonstrated that pulsating flow can effectively enhance heat transfer in various fields, including electronics, mechanical engineering, and medicine.

In this research, three flow patterns (continuous flow, uniform pulsating flow, and bio-inspired pulsating flow) were studied in both simulation and experimental designs. Two cooling designs were considered: the conventional design (C-Design) and the parallel design with baffles (W-B) and without baffles (Wout-B). With the implementation of 30 pulses per minute bio-inspired pulsating flow a reduction of 1.96% in solar cell temperature was observed when compared to continuous flow. This reduction in temperature was consistently observed across a range of flow rates from 0.5 to 2.5 L/m, employing the parallel Wout-B design. Notably, the bio-inspired pulsating flow shows better performance in comparison to uniform pulsating flow, as well as the conventional designs with continuous flow and uniform pulsating flow, resulting in notable improvements in cooling efficiency of 1.22%, 2.14%, and 4.00%, respectively.

In terms of a direct comparison, the implementation of uniform pulsating flow in the parallel Wout-B design exhibited a maximum cooling improvement of 0.74% when contrasted with continuous flow. Furthermore, when assessing uniform pulsating flow against the C-design with uniform pulsating flow in the parallel Wout-B design, a noteworthy enhancement of 0.93% was observed. Remarkably, the C-design with uniform pulsating flow demonstrated a superior effectiveness of 1.90% when compared to the C-design with continuous flow.

**Keywords:** Photovoltaic Cooling, power output, pulsating flow, temperature, heat transfer, human thermoregulation

## **ACKNOWLEDGEMENTS**

It gives me great pleasure to express my gratitude to everyone who assisted in completing my research project. My first and primary obligation is to extend my profound appreciation to the All-Mighty Allah (SWT), who has endowed me with the capacities, fortitude, and health to carry out this investigation.

Secondly, this remarkable accomplishment would have been impossible to achieve without the support and guidance of my supervisors. Therefore, I would like to express my gratitude to Prof Patrick Luk and Prof. Upul Kahagala Gamage, who provided me with the necessary support and contribution during this research. I would also like to thank Dr Jerry Luo and the members of his team, especially Fergus Crawley. Additionally, I appreciate the support of Adriana Stawiarska.

Thirdly, I am grateful to the Petroleum Technology Development Fund for providing me with a scholarship. Without this scholarship, gaining access to this life-changing opportunity would have been almost impossible. I am truly grateful to you.

In conclusion, I want to express my gratitude to my family for their unwavering support, especially my wife.

TABLE OF CONTENTS	ABSTRACT	.....	i
ACKNOWLEDGEMENTS	.....	iii	
LIST OF FIGURES	.....	vi	
LIST OF TABLES	.....	xi	
LIST OF EQUATIONS	.....	xii	
LIST OF ABBREVIATIONS	.....	xiii	
1	CHAPTER ONE	.....	1
1.1	General Introduction	.....	1
1.2	Research Gap	.....	3
1.3	Aim and Objectives	.....	3
1.4	Motivation	.....	4
1.5	Report Section Layout	.....	4
2	CHAPTER TWO	.....	6
2.1	Literature Review	.....	6
2.2	Introduction	.....	6
2.3	Types and Classification of Cooling Techniques in solar cell	.....	10
2.3.1	Heat pipes	.....	12
2.3.2	Phase Change Materials	.....	15
2.3.3	Jet impingement	.....	19
2.3.4	Liquid Immersion	.....	23
2.3.5	Micro-Channel Cooling	.....	27
2.4	Novel Approach to CPV Cooling	.....	33
2.4.1	Human Thermoregulation	.....	34
2.4.2	Pulsating Flow	.....	36
2.5	Summary	.....	38
3	CHAPTER THREE	.....	43
3.1	Methodology	.....	43
3.1.1	Design And Specifications	.....	43
3.2	Simulation	.....	49
3.2.1	Simulation Assumption	.....	50
3.2.2	Generating Simulation Pulsating Flow	.....	50
3.3	Experiment	.....	53
3.3.1	Generating Experiment Pulsating Flow	.....	56
3.4	Correlations In Continuous and Pulsating Flow	.....	60
4	CHAPTER FOUR	.....	65
4.1	Simulation Results	.....	65
4.1.1	Effect of Coolant Inlet Temperature	.....	65
4.1.2	Conventional Design (Con-Design)	.....	67
4.1.3	Parallel Design Without Baffles (Wout-B Design)	.....	73
4.1.4	Parallel Design With Baffles (WB-Design)	.....	78
4.1.5	Design Cross Comparison	.....	84
4.2	Experimental Results	.....	86

4.2.1 Conventional Design Experimental Result .....	86
4.2.2 Parallel Design Without Baffles Experimental Result .....	91
4.2.3 Error Analysis .....	102
4.3 Validation .....	105
4.3.1 Conventional Validation.....	105
4.3.2 Parallel Design Validation .....	107
5 CHAPTER FIVE .....	109
5.1 Discussion, Future work, Recommendations and Conclusion .....	109
5.1.1 Discussion.....	109
5.1.2 Future work and Recommendations .....	110
5.1.3 Conclusion .....	112
REFERENCES.....	114
Appendix A Specification of Multijunction Solar cell.....	138
Appendix B Components Specifications .....	139
Appendix C Pulsating Programme Arduino Code .....	142
Appendix D Inlet Temperature Effect and Temperature Contours .....	145
Appendix E Simulation Rerun Comparison.....	148

## LIST OF FIGURES

Figure 1-1 Research and report layout.....	5
Figure 2-1 Classification of photovoltaic.....	6
Figure 2-2 Trend of maximum efficiency in photovoltaics.....	8
Figure 2-3 Statistical charts of articles published and funding countries on CPV cooling. ....	9
Figure 2-4 Heat pipe basic working concept adapted and edited from [50].....	13
Figure 2-5 PV no cooling (a), Integrated PV-TE (b), Hybrid PV-TE-Heat pipe (c) Adapted from [59].....	14
Figure 2-6 Heat pipe attached to PV adapted from [61] .....	14
Figure 2-7 PCM (a), PCM attached to PV (b). PV (c) adapted from [81].....	17
Figure 2-8 PV Model of PCM with and without aluminium matrix with reference PV adapted from [86].....	18
Figure 2-9 PCM integrated with heat sinks adapted from [27].....	18
Figure 2-10 Temperature Variation of photovoltaic (PV), PV- heat sink, and PV-heat sink-PCM based on experimental results from [27] .....	19
Figure 2-11 Jet impingement cooling adapted from [89] .....	20
Figure 2-12 Jet impingement cooling skitch of a side view and experiment set-up adapted from [91] .....	21
Figure 2-13 Jet impingement cooling model adapted from [7].....	21
Figure 2-14 Diagram of CPV, microchannel integrated with Jet impingement heat and spreader adapted from [92] .....	22
Figure 2-15 Immersed PV panel in water according to [96].....	23
Figure 2-16 Rectangular channel (a) Receiver model of the channel (b) Receiver on sun under actual conduction adapted from [101].....	24
Figure 2-17 Experimental results showing the effect of liquid thickness adapted from [103] .....	25
Figure 2-18 A model bubble demonstration effect due to light-adapted from [104]. .....	26
Figure 2-19 Solar Panel Temperature distributions adapted from [27] (a) Uncooled (b) non-immersed heat pipes with active cooling (c) Immersed heat pipes in ethylene glycol (d) immersed heat pipes in normal water.....	27
Figure 2-20 Microchannel (a) Noncircular straight channel with Noncircular manifold channel [62] (b) Circular channel [116] .....	28



Figure 2-21 (a) Drawing of CPV module attached Microchannel (b) module flux pattern microfluidic cooling and (c) module flux pattern passive convection cooling adapted from [121] .....	29
Figure 2-22 CPV and multi-layer microchannel diagram adapted from [122] ...	30
Figure 2-23 Porous media and microchannel diagram for different cases adapted from [125] .....	31
Figure 2-24 CPV and multi-layer microchannel diagram adapted from [126] ...	32
Figure 2-25 CPV and multi-layer microchannel diagram adapted from [127] ...	33
Figure 2-26 Human thermoregulatory system model diagram according to [133–135] .....	34
Figure 2-27 Heat flux in a straight pipe and corrugated tube adapted from [145] .....	36
Figure 2-28 Looped pulsating heat pipe (a) glass showing fluid and air [149] (b) Process diagram adapted from [147].....	37
Figure 3-1 Model Chanel view (A) Conventional snake-type channel design (B) Parallel channel design without baffles and (C) Parallel channel design with baffles .....	43
Figure 3-2 Model sketch and Dimensions. ....	44
Figure 3-3 Model Cover and 5-multijunction solar cell sketch with Dimensions. ....	45
Figure 3-4 Complete Coupled Simulation 3D Model (A and B Top) and Experimental Coupled Built model (A and B Bottom) .....	46
Figure 3-5 Detailed Model Channel View .....	47
Figure 3-6 Model Mesh Sensitivity Analysis .....	50
Figure 3-7 Generating Pulsating Flow Parallel Design UDF (both without and with baffles) for 0.5l/m to 2.5l/m .....	52
Figure 3-8 Generating Pulsating Flow Conventional Design UDF for 0.5l/m to 2.5l/m.....	53
Figure 3-9 Experimental Process flow diagram for conventional Design.....	53
Figure 3-10 Experimental Process flow diagram for the Parallel design .....	54
Figure 3-11 Experimental Set Up .....	55
Figure 3-12 Design Holder .....	55
Figure 3-13 Temperature Sensor Holder.....	56
Figure 3-14 Location of thermocouples on experimental set-up.....	57

Figure 3-15 Wiring Connection set up .....	58
Figure 3-16 Uniform Pulsating Flow Signal for Flow Rate 0.5l/m to 2.5l/m, with a Frequency of 0.5Hz, and period of 2s.....	59
Figure 3-17 Bio-Inspired Pulsating Flow Signal for Flow Rate 1.0l/m, Frequency of 0.5Hz, and period of 2s.....	60
Figure 4-1 Effect of coolant inlet temperature on solar cell temperature .....	65
Figure 4-2 Effect of coolant inlet temperature on cooling pad temperature .....	66
Figure 4-3 Effect of coolant inlet temperature on solar cell temperature contours at 1L/m, 150suns concentration and 305K water inlet temperature (a) Conventional design, (b) Parallel design without baffles, (c) Parallel design with baffles.....	66
Figure 4-4 Effect of coolant Inlet temperature on cooling block temperature contours at 1L/m, 150suns concentration, and 305K water inlet temperature (a) Conventional design, (b) Parallel design without baffles, (c) Parallel design with baffles .....	67
Figure 4-5 Con-design solar cell temperature with continuous flow and pulsating flow at $T = 2$ s, $f = 0.5$ Hz, 30puls/minutes, $Pr = 5.72$ and $Pr = 5.62$ , respectively.....	68
Figure 4-6 Solar cell temperature contours at 1L/m, 150suns concentration (a) Continuous flow, (b) Pulsating flow.....	68
Figure 4-7 Temperature contours at 1L/m, 150suns concentration conventional design (a) Complete 3D view (b) 2D x-y centre cut-view (c) 2D z-y centre channel cut-view.....	69
Figure 4-8 Variation of Nusselt number with flow rate .....	70
Figure 4-9 Variation of Nusselt number against Strouhal number.....	70
Figure 4-10 Pulsating velocity against heat transfer enhancement and Womersley number .....	71
Figure 4-11 Conventional design variation of oscillating Reynolds number ( $Re_{\omega}$ ), and stable components Reynolds number ( $Re_s$ ) against velocity oscillating amplitude at $f = 0.5$ .....	72
Figure 4-12 Relationship of flow rate and heat transfer coefficient.....	72
Figure 4-13 Parallel Wout-B design solar cell temperature with continuous flow and pulsating flow at $T = 2$ s, $f = 0.5$ Hz, 30puls/minutes, $Pr = 5.70$ and $Pr = 5.40$ respectively.....	73
Figure 4-14 Solar cell temperature contours at 1L/m, 150suns concentration (a) Continuous flow, (b) Pulsating flow.....	74

Figure 4-15 Temperature contours at 1L/m, 150suns concentration parallel design without baffles (a) Complete 3D view, (b) 2D x-y centre cut-view (c) 2D z-y centre channel cut-view.....	75
Figure 4-16 Variation of Nusselt number with flow rate .....	75
Figure 4-17 Variation of Nusselt number against Strouhal number .....	76
Figure 4-18 Pulsating velocity against heat transfer enhancement and Womersley number .....	77
Figure 4-19 Parallel design without baffles variation of oscillating Reynolds number ( $Re_{\omega}$ ), and stable components Reynolds number ( $Re_s$ ) against velocity oscillating amplitude at $f = 0.5$ .....	77
Figure 4-20 Relationship of flow rate and heat transfer coefficient.....	78
Figure 4-21 Parallel WB-Design solar cell temperature with continuous flow and pulsating flow at $T = 2s$ , $f = 0.5Hz$ , 30puls/minutes, $Pr = 5.70$ and $Pr = 5.40$ , respectively.....	79
Figure 4-22 Solar cell temperature contours at 1L/m, 150suns concentration (a) Continuous flow, (b) Pulsating flow.....	80
Figure 4-23 Temperature contours at 1L/m, 150suns concentration parallel design (a) Complete 3D view, (b) 2D x-y centre cut-view (c) 2D z-y centre channel cut-view .....	80
Figure 4-24 Variation of Nusselt number with flow rate parallel WB-design .....	81
Figure 4-25 Variation of Nusselt number with Strouhal number parallel WB-design .....	82
Figure 4-26 Parallel WB-design pulsating velocity against enhancement and Womersley Number .....	82
Figure 4-27 Parallel WB-design pulsating amplitude at $f = 0.5$ against oscillating Reynolds number ( $Re_{\omega}$ ), and stable components Reynolds number ( $Re_s$ ) plot against velocity oscillating amplitude .....	83
Figure 4-28 Variations of flow rate versus Reynolds number parallel WB-design .....	84
Figure 4-29 Design cross-comparison with pulsating flow variations of flow rate versus solar cell temperature.....	85
Figure 4-30 Solar cell temperature contours at 1L/m, 150suns concentration, and 30puls/minutes and (a) Conventional design, (b) Parallel design without baffles and (c) Parallel design with baffles.....	85
Figure 4-31 Solar cell temperature with continuous flow and pulsating flow at $T = 2s$ , $f = 0.5Hz$ , 30puls/minutes, $Pr = 5.70$ and $Pr = 5.40$ , respectively .....	87
Figure 4-32 Variation of Nusselt number against Strouhal number .....	87

Figure 4-33 Performance thermal resistance versus flow rate .....	88
Figure 4-34 Pulsating velocity variation with cooling enhancement and Womersley number .....	89
Figure 4-35 Variations of Reynolds number versus pulsating amplitude .....	89
Figure 4-36 Variations of flow rate versus heat transfer coefficient .....	90
Figure 4-37 Solar cell temperature at 1L/m, 150suns concentration, and 30puls/minutes .....	91
Figure 4-38 Variation of Nusselt number against flow rate .....	92
Figure 4-39 Variation of Nusselt number against Strouhal number .....	93
Figure 4-40 Pulsating velocity variation with cooling enhancement and Womersley number .....	94
Figure 4-41 Variations of Reynolds number versus pulsating amplitude .....	95
Figure 4-42 Variations of flow rate versus heat transfer coefficient parallel .....	95
Figure 4-43 Performance thermal resistance versus flow rate .....	96
Figure 4-44 Pulsating velocity variation with cooling enhancement and Womersley Number .....	97
Figure 4-45 Solar cell Temperature conventional and parallel design without baffles experiment result .....	98
Figure 4-46 Cracks on temperature sensor holder due to pulsating flow vibration of uniform pulsation at 30puls/minutes .....	99
Figure 4-47 Solar cell power output .....	100
Figure 4-48 Solar cell current versus flow rate .....	101
Figure 4-49 Solar cell voltage versus flow rate .....	101
Figure 4-50 Pressure drops against flow rate continuous flow .....	105
Figure 4-51 Pressure drops against flow rate pulsating flow .....	106
Figure 4-52 Variations of flow rate versus Reynolds number .....	106
Figure 4-53 Pressure drops variation against flow rate continuous flow .....	107
Figure 4-54 Pressure drops variation against flow rate pulsating flow .....	107
Figure 4-55 Variations of flow rate versus Reynolds number .....	108

## LIST OF TABLES

Table 2-1 A Comparative between conventional solar cell with concentrated multijunction solar cell.....	10
Table 2-2 A Classification of photovoltaic cooling Advantages and Disadvantages .....	11
Table 2-3 Challenges in CPV cooling.....	40
Table 2-4 Heat Transfer enhancement approach in thermal Energy management .....	41
Table 3-1 Model Specifications .....	48
Table 3-2 Flow Rates and Velocity Calculations For UDF.....	51
Table 3-3 Simulation settings and initial conditions .....	51

# LIST OF EQUATIONS

(3-1).....	47
(3-2).....	48
(3-3).....	48
(3-4).....	49
(3-5).....	49
(3-6).....	49
(3-7).....	61
(3-8).....	61
(3-9).....	61
(3-10).....	61
(3-11).....	62
(3-12).....	62
(3-13).....	62
(3-14).....	62
(3-15).....	62
(3-16).....	62
(3-17).....	63
(3-18).....	63
(3-19).....	63
(3-20).....	63
(3-21).....	63
(3-22).....	63
(3-23).....	63
(3-24).....	64
(3-25).....	64
(3-26).....	64
(3-27).....	64
(3-28).....	64

## LIST OF ABBREVIATIONS

CFD	Computational Fluid Dynamic
CNC	Computer Numerical Control
PV	Photovoltaic
CPV	Concentrated Photovoltaic
MJSC	Multiple Junction Solar Cells
UP	Uniform Pulsating Flow
BI	Bio-inspired Pulsating flow
Cont.	Continuous Flow
Con	Conventional Design
Wout-B	Without baffles design (parallel)
WB	With baffles design (parallel)
Nu	Nusselt Number
Pr	Prandtl Number
Re	Reynolds Number
St	Strouhal Number
$\alpha$	Womersley Number
f	Frequency
T	Period
$\omega$	Angular velocity

# 1 CHAPTER ONE

## 1.1 General Introduction

Global energy consumption is continuing to rise, resulting in the emission of pollutants from burning fossil fuels. To decrease carbon emissions and secure future energy sources to meet the demand, various renewable energy technologies are being used [1]. Non-conventional energy is becoming increasingly popular, and more countries are investing in it [1,2]. Solar cells are among the most significant renewable energy sources because they directly convert the sun's rays into electricity. Both external and internal factors impact the performance of photovoltaic panels. Uncontrollable external factors include dust accumulation, ambient temperature, incident radiation rate, and wind velocity, while internal factors, such as PV average temperature, are controllable [3].

The energy from the sun's light appears white because it is made up of several different colours that, when blended, produce white light. The quantity of energy in each direct and indirect radiation in the sun's spectrum varies greatly. To increase the efficiency and energy utilization of the solar spectrum, solar cells can be concentrated or a multijunction solar cell can be used [3–5]. However, when sunlight is focused onto solar cells, some energy is converted to electricity, while the rest is converted to thermal energy, causing overheating within the cell. As a result, a drastic drop in efficiency or even damage to the solar cell can occur, depending on the concentration level and how high the cell area temperatures build up [6–10].

Advances and innovations in photovoltaic technology have allowed the development of smaller and more efficient solar cells, such as multiple junction solar cells (MJSC). MJSC with absorbers of varying band gaps can be utilized to increase the energy utilization of the solar spectrum [5,11–13]. The lost access energy of absorbed photons can be reduced in a concentrated multi-junction solar cell (C-MJSC) with a lens or mirrors [3,4,14–16]. However, the temperature of the solar cell increases to an extent where cooling the cell is mandatory to keep its



performance at its best and prevent the cell from permanent damage [17]. The cooling mechanism must be carefully designed and studied for optimum performance. Cooling photovoltaic (PV) cells is a critical design and operational consideration in concentrated PV (CPV) technology. High cell temperature and uneven temperature distribution result in current mismatching and hot spots on the solar cell, resulting in either decreased efficiency or severe damage due to thermal stresses. The uniformity of temperature across the surface of photovoltaic panels significantly influences the effectiveness of CPV systems, directly increasing cell temperature and series resistance.

Researchers have been investigating the significance of uniform cooling in CPV. Several studies have highlighted various types of uniform cooling mechanisms for solar PV panels, including liquid immersion cooling, heat pipe cooling, microchannel cooling, impinging jet cooling, phase change material cooling, heatsink cooling, and better heat exchanger design cooling. However, the suitability of a cooling method is contingent on the Sun concentration, location, installation, and system output requirements. A CPV's cooling system can be classified as passive or active, depending on the geometry, coolant, and level of sun concentration [18].

In the passive cooling technique, a heat pipe can dissipate flux, and it has been demonstrated that CPV can be cooled using fins/plates. However, the disadvantage of passive cooling is that the heatsink area increases proportionately to the CPV sun concentration [19–21]. Much research has highlighted that passive cooling is unsuitable for higher sun concentration [15,22,23], say above 20 suns. Active cooling to achieve temperature uniformity has been studied. It has been reported that the active cooling system works based on continuous flow [23,24] and is a better option for CPV cooling. Jet impingement and heat pipe systems exhibit significant temperature variations, posing the challenge of temperature non-uniformity. Additionally, jet impingement requires a large volume of coolant and presents design complexities such as diameter spacing, nozzle pitch and number, and spent flow or drainage design problems (liquid drain, leakage, clogging) [26]. The liquid immersion cooling

technique is suitable for high solar concentration ratios; however, it challenges performance degradation due to coolant interaction with CPV. Another challenge is the selection of coolant type to avoid short circuiting of electronic components [27]. Moreover, the overall architecture leads to an increase in weight and requires considerable pumping power.

CPV cooling is essential for achieving more energy-efficient concentrated solar cells with maximum power output. There is a need for an optimal cooling system, and further investigation of techniques is required to increase the efficient power output of a CPV [28]. This research aims to develop and investigate a concentrated, multijunction solar cell cooling system to increase thermal efficiency. To achieve this goal, the current cooling system, including CPV, garments, and human body cooling systems, was reviewed. Simulations using computational fluid dynamics and experimental approaches will be adapted to achieve the objectives highlighted in section 1.2. Two publications have been compiled from this research and will be submitted to two journals.

## **1.2 Research Gap**

Several research studies have highlighted the advantages of pulsating flow in cooling and enhancing heat transfer. It has been applied in various fields such as electronics, data centres, and mechanical and thermal energy engineering. However, to the best of our knowledge, pulsating flow has not been directly applied to CPV cooling. Instead of a continuous flow, which is the basis of current CPV cooling, this research focuses on the performance of CPV cooling with unsteady flow (pulsatile flow). The technique is achieved by integrating solenoid valves with controls and sensors to introduce bio-inspired cooling, mimic human thermoregulation, and improve cooling capabilities.

## **1.3 Aim and Objectives**

This research aims to model and investigate the cooling system performance of a concentrated multijunction solar cell while considering all the factors that affect cooling system performance, including design parameters.

1. Comprehensive Review of CPV cooling techniques.

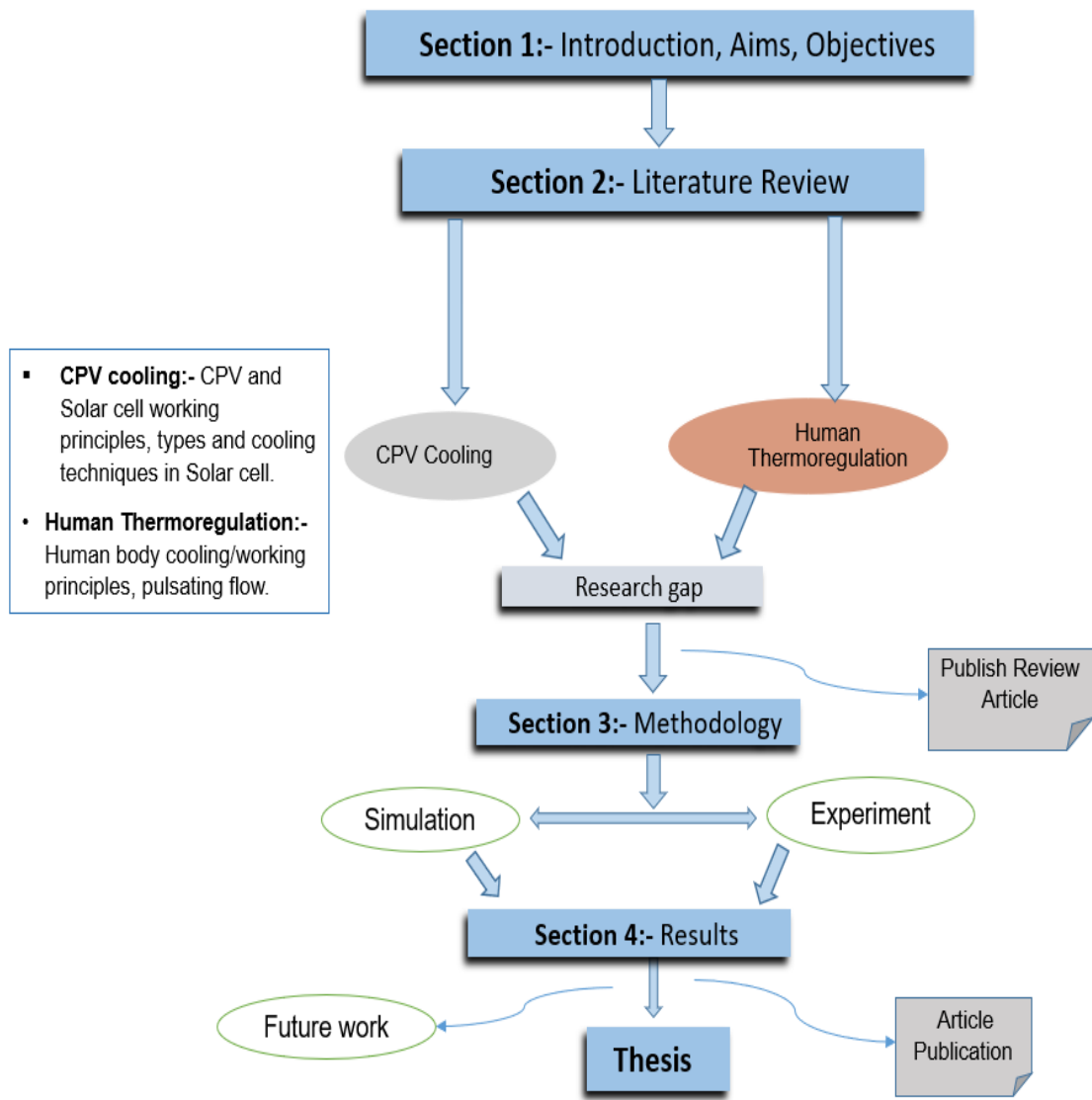
2. Design a cooling system using computer-aided design (CAD) that will be applicable in continuous and pulsating flow.
3. Simulate the performance and investigate the applicability of pulsating flow in cooling using computational fluid dynamics (CFD).
4. Build the prototype design and develop a pulsating flow system experimentally.
5. Investigate and validate the prototype with the pulsating flow, bio-inspired pulsating flow and continuous flow experimentally with the simulated design.

## **1.4 Motivation**

The motivation for this work is to increase the power output of concentrated solar cells, specifically with regards to cooling demands. The need for efficient cooling is inevitable in CPV, and more researchers are becoming interested in this area. Currently, CPV's cooling technologies are almost exclusively based on continuous flow. The first motivation is related to the efficiency of operation compared to conventional cooling technologies. There is a need to have a system that is comparable and efficient when compared to existing technologies. Secondly, the aim is to maximize the solar cell's power output to enable it to operate at its full potential. Finally, it is essential to consider whether pulsating flow can provide an alternative to existing cooling approaches.

## **1.5 Report Section Layout**

This research thesis report comprises sections as indicated in figure 1-1. Each section is designated a chapter, followed by a discussion, recommendations, and references.



- **CPV cooling:-** CPV and Solar cell working principles, types and cooling techniques in Solar cell.
- **Human Thermoregulation:-** Human body cooling/working principles, pulsating flow.

**Figure 1-1 Research and report layout.**

## 2 CHAPTER TWO

### 2.1 Literature Review

This chapter provides a literature review that includes information about the types of solar cells, concentrated solar cells (CPV), and the types and classification of CPV cooling. Based on the available literature, detailed information on the challenges, advantages, and research gaps was discussed. Additionally, a brief insight into the novelty of this research presents an innovative approach to CPV for researchers, using discontinuous flow as a bio-inspired cooling idea (mimicking human thermoregulation) to explore a better solution in CPV cooling systems.

### 2.2 Introduction

The use of solar energy has significantly increased over the past two decades, becoming a major component of the world's total energy mix [1,2,28]. Photovoltaic cells are capable of producing electricity from the sun, and represent a promising alternative to the use of fossil fuels, which contribute to global warming [29–31]. Solar energy is the most abundant and readily accessible source of energy on our planet [32,33], with silicon - sourced from sand - being the primary material used to convert this energy into a usable form [34]. Despite these advantages, current cooling techniques for concentrated solar cells are based on continuous flow, which results in non-uniform temperature distribution throughout the cell and other issues. Photovoltaics are commonly classified into first-generation (1stG), second-generation (2ndG), and third-generation (3rd G), as illustrated in Figure 2-1.

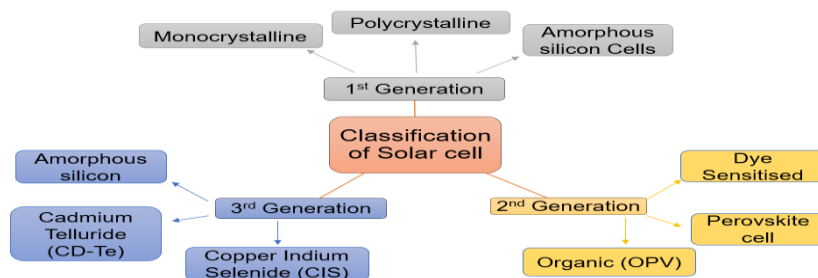
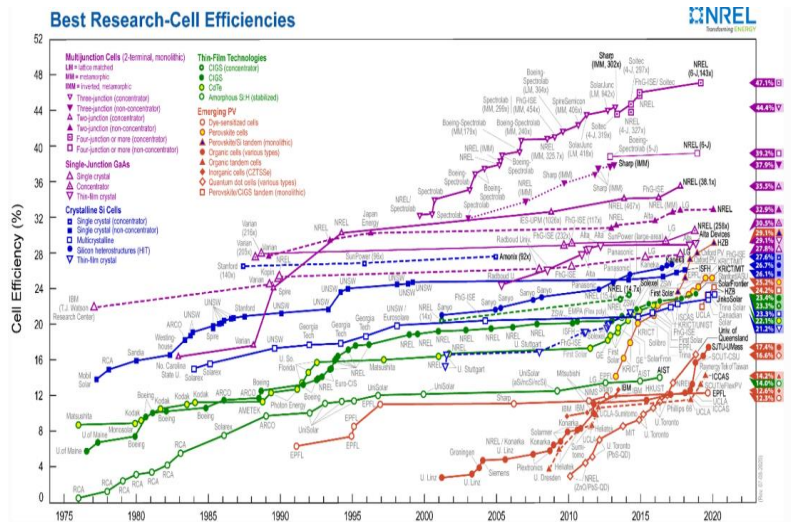


Figure 2-1 Classification of photovoltaic

The first generation (1stG) includes monocrystalline panels, polycrystalline panels, and amorphous solar cells. These photovoltaics were the first commercial photovoltaic cells introduced in 1954. In the 21st century, they are the most commonly used solar cells in residential areas, accounting for about 80% of solar cells sold. 1stG can have an efficiency of up to 26% for monocrystalline and 21% for polycrystalline, according to Green MA and Emery K in 2016. They are made of silicon and have a bandgap of 1.1 eV [34,35].

The 2ndG, with an efficiency of 21.4%, came into existence after 20 years of research and development aimed at achieving lower costs and inherently higher efficiency [34]. However, a disadvantage is that the majority of the components of these cells are becoming increasingly rare and expensive (indium), and some are toxic (cadmium).

The 3rdG is a recent generation that has emerged due to the high costs of 1stG solar cells, material availability limitations, and the toxicity of 2ndG solar cells. Solar cells are made from various new materials in addition to silicon, such as nanomaterials, silicon wires, solar inks created with conventional printing press technology, conductive plastics, and organic dyes [34,36]. In [36], the new generation of solar cell technology is classified as the fourth generation (4thG). It uses a combination of organic and inorganic materials for manufacturing. The advantage of 4thG is the combination of inorganic and organic materials to maintain cost and increase solar to electrical energy conversion efficiency. Figure 2 shows the maximum efficiency in photovoltaics according to the National Renewable Energy Laboratory (NREL) 2020, as cited in [31].

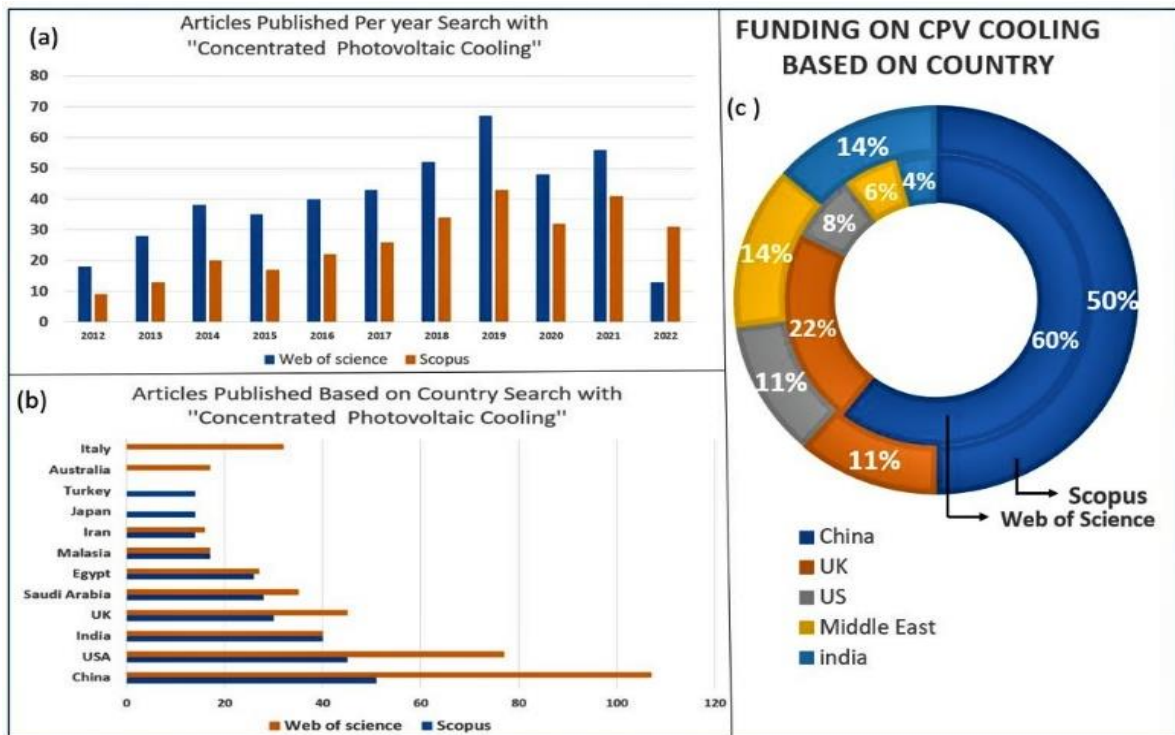


**Figure 2-2 Trend of maximum efficiency in photovoltaics.**

Concentrated Photovoltaic (CPV) technologies are advanced PV systems that operate by focusing the sun's rays onto a solar cell using reflectors, such as mirrors or an optical prism [7,15,23]. The reflector, which is typically a mirror or lens, concentrates the primary solar radiation onto a solar cell located at the reflector's focal point. CPV systems require sun tracking to maintain the radiation's concentration on the solar panel [9]. It has been estimated that with a 1000 Suns solar concentration ratio, the temperature of an uncooled solar cell could rise to 1,360°C [7]. The solar energy falling onto the solar cell's surface is converted into electricity, while the rest is absorbed thermally within the solar cell, increasing its temperature [8]. Over time, an increase in panel temperature leads to decreased conversion efficiency and reduced panel reliability. Consequently, numerous cooling systems have been developed and studied to prevent excessive temperature increases and improve efficiency [32]. Concentrated multijunction solar cells are crucial to realizing a more efficient photovoltaic system. However, cooling CPV systems remains a challenge for researchers [25].

Substantial research on concentrated photovoltaic cooling (CPVC) is ongoing globally, and statistics over the previous decade (2012–2022) demonstrate the increasing interest and relevance of CPV cooling technology. In the past decade, a large number of research publications have been released. According to Scopus and Web of Science, with a search titled "Concentrated Photovoltaic

Cooling," over 288 and 438 papers were published on CPVC from 2012 to May 2022, respectively. Figure 2-3 displays the statistical number of Scopus and Web of Science research released each year (Figure 2-3a), comprehensive information on the first ten nations with the most significant proportion of research papers (Figure 2-3b), and the first five countries with the most funding investment (Figure 2-3c) on the current topic.



**Figure 2-3 Statistical charts of articles published and funding countries on CPV cooling.**

Research by [9] experimented and reported that the output of a concentration solar panel is between 4.7 and 5.2 times that of a non-concentrated cell. The results demonstrate that the solar cell temperature was reduced to below 60°C, generating more electrical output. Research using parabolic concentrators to analyse heat transfer in photovoltaics has been conducted by [37]. It was found that the higher the intensity of incident solar energy, the higher the temperature of the concentrator aperture and the PV cell. A comparative analysis between the most commercially available photovoltaic with a concentrated multijunction solar cell is presented in Table 2-1 based on the following references [3,38–42].



**Table 2-1 A Comparative between conventional solar cell with concentrated multijunction solar cell**

<b>Type of Solar cell</b>	<b>Monocrystalline</b>	<b>Polycrystalline</b>	<b>Thin film</b>	<b>Concentrated Multi-junction</b>
<b>Type of material</b>	Fragments from single wafer crystal	fragments from different silicon crystals	Fragments from single wafer crystal	Combination of different semiconductors
<b>Life span</b>	25 to 30 years	20 to 25 years	10 to 20 years	30 or more years
<b>Efficiency</b>	14 to 26%	12 to 21%	very low	33.8 to 69.1
<b>Appearance</b>	aesthetic	Non aesthetic	aesthetic	aesthetic
<b>Portability</b>	Big, comes in different size	Big, comes in different size	Flexible lightweight	Lightweight, smaller size
<b>Number of Junctions</b>	1	1	1	It can have 2-7
<b>Cost</b>	High	High	Low	Higher

### **2.3 Types and Classification of Cooling Techniques in solar cell**

Research and development in concentrated photovoltaics have heightened the requirement for effective cooling. The essence of an effective cooling system in concentrated solar cells is to ensure that the PV cell operates within its optimal temperature. CPV cooling design should have reduced thermal resistance coefficients with good cell temperature uniformity for maximum efficiency [25]. Additionally, it is vital to consider the cooling system's power consumption, ease of installation, and high level of dependability. The selection of a cooling technique depends on the objective and need situation at hand [25]. However, the suitability of a cooling method is contingent on the Sun concentration, location, installation, and system output requirements [20]. CPV cooling can be classified as passive or active, depending on the geometry, coolant, and level of sun concentration [20]. Furthermore, CPV cooling can be classified based on the nature of heat transfer, such as natural circulation and forced circulation, or the type of coolant, such as passive cooling and active cooling [21,32,43]. [44] reported that passive cooling is suitable for concentrations of less than 20 suns, and active cooling is necessary for high concentrations.

Natural circulation and forced circulation can be air-based cooling and water-based cooling. Air-based cooling is simple and cheaper [43]. However, it has a lower heat transfer coefficient, which varies from 1-10W/m<sup>2</sup>.K for natural circulation to 20-100W/m<sup>2</sup>.K for forced circulation [25]. Water-based cooling has a better heat transfer coefficient of 200-1000W/m<sup>2</sup>.K for natural circulation and 1000-1500W/m<sup>2</sup>.K for forced circulation [37,45,46]. According to [9], the efficiency of a Concentrated solar cell is primarily affected by the amount of heat removal rate, which aids in the PV temperature management. The heat removal rate is primarily determined by the coolant flow rate [9]. Table II provides the advantages and disadvantages of CPV cooling based on classifications.

**Table 2-2 A Classification of photovoltaic cooling advantages and disadvantages**

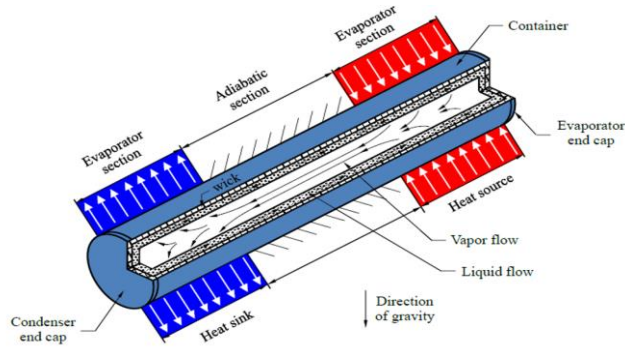
<b>Classification Based on Nature of Heat Transfer</b>		
	<b>Natural Convection</b>	<b>Forced Convection</b>
<b>Advantage</b>	<ul style="list-style-type: none"> <li>• Energy consumption is Low</li> <li>• Low cost</li> <li>• Simpler design</li> <li>• Less Corrosive</li> </ul>	<ul style="list-style-type: none"> <li>• Electrical power is needed</li> <li>• low cost</li> <li>• Design can be complex</li> </ul>
<b>Disadvantage</b>	<ul style="list-style-type: none"> <li>• Limited heat dissipation ability</li> <li>• Prompt to Problem of temperature nonuniformity</li> </ul>	<ul style="list-style-type: none"> <li>• More heat dissipation ability</li> <li>• Temperature nonuniformity is achievable for lower medium concentration</li> <li>• Prompt to corrosion problem</li> </ul>
<b>Classification Based on Nature of Coolant</b>		
	<b>Passive Cooling</b>	<b>Active Cooling</b>
<b>Advantage</b>	<ul style="list-style-type: none"> <li>• Energy consumption not Required</li> <li>• Reliable</li> <li>• Simple design</li> <li>• Suitable lower concentration</li> </ul>	<ul style="list-style-type: none"> <li>• Higher heat dissipation ability</li> <li>• Can be combine with other thermal system</li> <li>• Design can be complex</li> <li>• High cooling capability</li> <li>• Suitable for lower concentration</li> <li>• Can work for more extended period</li> </ul>
<b>Disadvantage</b>	<ul style="list-style-type: none"> <li>• Low cooling capability</li> <li>• Relatively short time of service</li> <li>• Low or Limited heat dissipation ability</li> </ul>	<ul style="list-style-type: none"> <li>• Required leakproof for liquid coolants</li> <li>• Energy consumption Required</li> </ul>
<b>Example</b>	Heat Pipes, Phase change materials, liquid immersion	Jet impingement, microchannel, Active liquid immersion, Hybrid cooling systems

In passive cooling (PC), no external force or energy is used for coolant circulation. The PC technique has been studied through experimental investigation, and it has been reported by [47] that the heat pipe and heat sink have the capacity to dissipate flux in CPV. Both the heat pipe and heat sink were found to be able to cool CPV to 37.8°C and 54.16°C under 25 suns, respectively. Researchers have highlighted that it is a cost-effective cooling method because of its low energy consumption. However, the disadvantage of passive cooling is the size of the heatsink area, which is not economically viable due to the large amount of material required, consisting of larger fins and plate areas depending on the concentration ratio [19,20,48]. In other words, the greater the concentration ratio of the CPV, the larger the area of the heatsink required. Consequently, the feasibility and attractiveness of utilising a passive cooling system to mitigate the temperature of a concentrated photovoltaic system have been significantly diminished.

Active cooling (AC) has been studied to achieve temperature uniformity. In AC, coolant circulates through the cooling system using an active cooling system pump. It collects the heat from the PV and dissipates it using a convector or heat sink. Several researchers have highlighted that active cooling is more efficient and suitable for high concentrations [7,27,47,49]. However, one of the limitations posed by AC includes temperature non-uniformity. A variety of solar cell cooling techniques are discussed in the following sections.

### **2.3.1 Heat Pipes**

Heat pipes are closed evaporator-condenser systems with high heat flux transport capacity, as shown in Figure 2-4. Heat pipes consist of an evaporator, a conduction section, and a condenser section [50]. The working fluid is vaporized in the evaporator section due to the conducted heat to the pipe wall, and vapor pressure forces it through the pipe section into the condenser section, where it condenses and releases its latent heat of vaporization into the provided heatsink. Capillary pressure pumps fluid back to the evaporator section [50,51]. The heat pipe continuously transports the latent heat from the evaporator to the condenser.



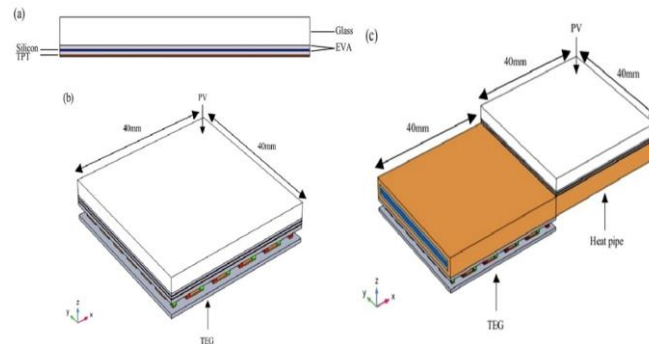
**Figure 2-4 Heat pipe basic working concept adapted and edited from [50]**

Heat pipes are cost-effective and versatile, suitable for various applications. Different working fluids can be used in heat pipes to transport heat energy from the heat source to the condenser section. The heat transport capability of the pipe depends on the type of working fluid used, and this determines their suitability for various applications such as heatsinks in laptop computers, embedded heat pipes for single-board computers, CPUs [52,53], military applications, RF telecommunications applications, lithium batteries, and server cloud computing [54–56].

Heat pipes come in various shapes and sizes and can be fabricated from various materials compatible with the working fluids used. They can be closed or open with refrigerant or water as the working fluid [50]. Open heat pipes are classified as an active cooling type because the coolant circulates using a pump. Proper material choices can reduce the chance of working fluid and material interaction, heat pipe degradation, and failure. Material types include copper, aluminum, and stainless steel. The most common shape is round flat heat pipes. Heat pipes can be bent based on system requirements and generally transfer heat energy from one point to another.

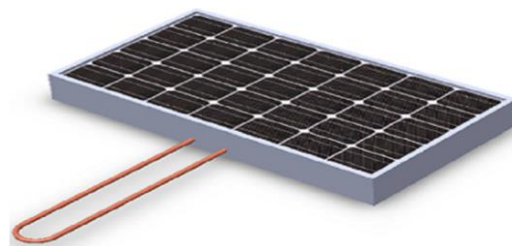
Research reported by [57] shows that a flat-structured plate heat pipe has a higher conversion efficiency of about 3.1% than aluminum substrates. Their results demonstrated that heat pipes could cool a high-concentration CPV system. Another research by [58] shows that the electrical efficiency of a CPV increases from 13% to 20% using heat pipes with 400 concentrations. They stated that as the sun's concentration increases, the outlet temperature of the

coolant increases. Their cost analysis study concluded that heat pipes are a more economical and realistic form of cooling. An experiment using a heat pipe was conducted by [59] to improve photovoltaic performance. Three modules were studied: PV, PV with thermoelectric, and PV with thermoelectric/heat pipe, as shown in Figure 2-5. They reported an efficiency of 1.47% and 61.01% for the module coupled with a heat pipe and the first and second modules, respectively.



**Figure 2-5 (a) PV no cooling, (b) Integrated PV-TE, (c) Hybrid PV-TE-Heat pipe Adapted from [59]**

A CPV cooling method that uses aluminium as a thermal absorber and heat pipes has been reported by [60] using a triple-junction solar cell. Research by [61] applied a heat pipe at the back of solar panels to extract the heat, as shown in Figure 2-6. The results indicated that the PV surface temperature could reach 41.2 °C, 37.2 °C, 33.3°C, and 29.3°C when the concentration ratio was 800 suns, 700 suns, 600 suns, and 500 suns, respectively. The CPV system's electrical efficiency was 20%, and its thermal efficiency was 77% using distilled water. The results indicate that the solar panels integrated with heat pipes have roughly 18% higher electrical efficiency than PV without a cooling system.



**Figure 2-6 Heat pipe attached to PV adapted from [61]**

Heat pipe utilization for cooling CPV systems has received little attention based on available literature. This may be due to the passive nature of heat pipes, which are suitable for low-concentration ratios. Further investigation into the capability of using heat pipes to cool CPV systems is necessary [25]. Heat pipe cooling has been reported to maintain a cell temperature between 32°C and 36°C, with a degree of non-uniformity of approximately 3°C for concentrated systems. Research has also shown that heat spreader heatsink techniques can reduce cell temperatures to 37°C using passive cooling methods [20]. Several review articles and researchers have highlighted the cost-effectiveness of heat pipe cooling [58,62].

Stabilizing nanofluids for long-term use is essential, as highlighted by many researchers. An increasing number of studies show that introducing additives such as nanoparticles slightly enhances thermal performance. However, using nanoparticles has some disadvantages, including corrosion problems [63], high cost [64], stability issues [65,66], sedimentation, agglomeration, and pressure drop [67,68]. Researchers are currently studying homogenizing methods, surfactants, pH, nanoparticle-base fluid combinations, and particle morphology to improve stability. Additionally, further work is needed to prevent agglomeration and sedimentation, reduce pump power, and improve stability [67].

Challenges for heat pipe cooling systems include overheating, oscillatory and reverse thermal flows, and the area-dependent cooling capacity for concentration [20,62]. Additionally, heat pipes work based on a continuous flow, and the problem of solar cell temperature non-uniformity leading to hot and cooling spots remains an area for exploration.

### **2.3.2 Phase Change Materials**

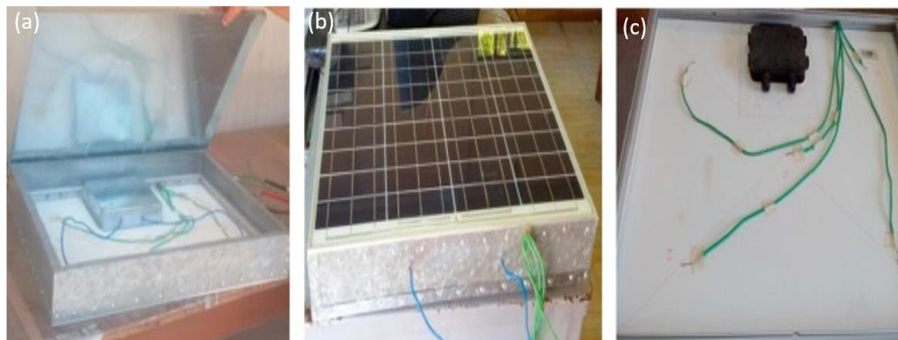
A phase change material (PCM) is capable of storing energy in a hotter environment and releasing it over an extended period [69]. When PCMs are activated and installed, their maximum energy turns solid. As they release their cooling energy, they become liquid. PCM packs can be reactivated repeatedly by simply placing them in the fridge, freezer, or a lower environment. A large amount of heat can be absorbed by phase change material without causing it to become

hotter. The heat stored in PCM can be released later when the surrounding conditions shift or become colder. They are easily used, cost-effective, and have various applications [70]. Currently, PCM is used in electronics [71], waste heat recovery, automobiles, and thermal energy conversion applications [72–74]. The heat fades at night. Packets of PCM can be placed underneath solar panels to prevent heat build-up during the day and release it at night when the panels are not in use [8,75–78]. A wide selection of PCM products is available, each with its temperature range [79].

Cooling with PCM is a more advanced heat management system for photovoltaic (PV) systems [79]. One of PCM's primary advantages is that it can regulate temperature depending on its latent heat, which results in near-form temperature cooling. The thickness (PCM area) and melting point are used to determine the suitability and stability of sustained PCM cooling. The main limitation of PCM passive cooling is that the PCM materials are toxic and corrosive. Another concern is safety and disposal issues at the end of the PCM product's life cycle [20]. Experimental research by [80] demonstrated that PCM could passively cool a CPV. However, they reported limited effectiveness due to low thermal conductivity, crystallisation segregation, and solidification duration. Their results show that adding fins can enhance the control of the PV temperature. The PCM cooling system is a promising future solar cell cooling technique [8,75–78]. However, this technique provides only a modest improvement due to its low thermal conductivity. The heat transfer of the PCM should be enhanced by adding a component to improve its cooling efficiency [32].

Several pieces of research show that introducing fins adjacent to PCM or introducing additives such as nanoparticles slightly enhances the performance of the PCM cooling technique. However, there are limitations including high cost, and stabilising nanofluids for long-term use is essential, as highlighted by many researchers [64], stability [65,67], sedimentation and agglomeration, among others [67]. Studies on homogenising methods, surfactants, pH, nanoparticle-base fluid combinations, and particle morphology are ongoing to improve stability [67]. Figure 2-7 shows PCM attached to PV for an experimental study conducted

by [81]. Using Al<sub>2</sub>O<sub>3</sub> nanoparticles and PCM, their results show a 13.2% and 5.7% increase in efficiency.



**Figure 2-7 (a) PCM (b) PCM attached to PV (c) PV adapted from [81]**

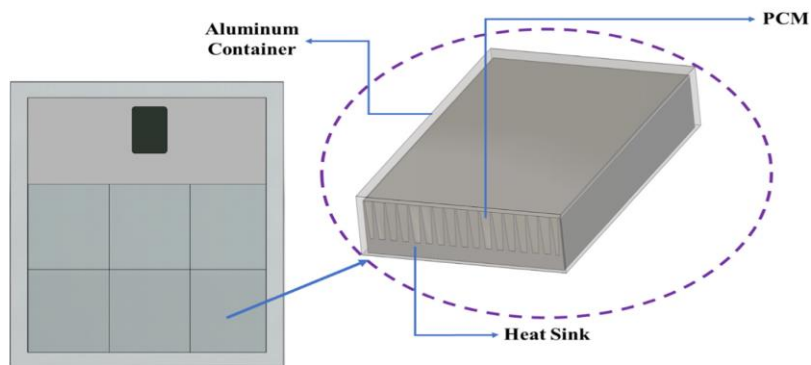
Adding nanoparticles to PCM is an advanced approach to increase the heat transfer of the PCM, more so than adding fins to PCM. However, due to the high cost of nanoparticles, this approach was deemed uneconomical. Introducing porous metal to PCM improves its cooling capability and is more cost-effective than adding nanoparticles [21,32]. Several researchers are debating combining carbon-based materials such as graphite, expanded graphite, and carbon nanotubes to enhance the thermal conductivity of PCM [82–84]. According to experimental results by [85], combining paraffin wax with CuO nanoparticles can increase thermal conductivity and enhance thermal performance. However, they stressed that nanoparticles are not cost-effective compared to a mixture of paraffin wax and nanoparticle. Research by [86] compared the performance of pure PCM and PCM with an aluminium matrix using a serpentine-based tube, as shown in Figure 2-8. Their results showed that the electrical efficiency of the solar cell with pure PCM increased by 3.5%, while the PV with the combined PCM/aluminium had an 8% increase.



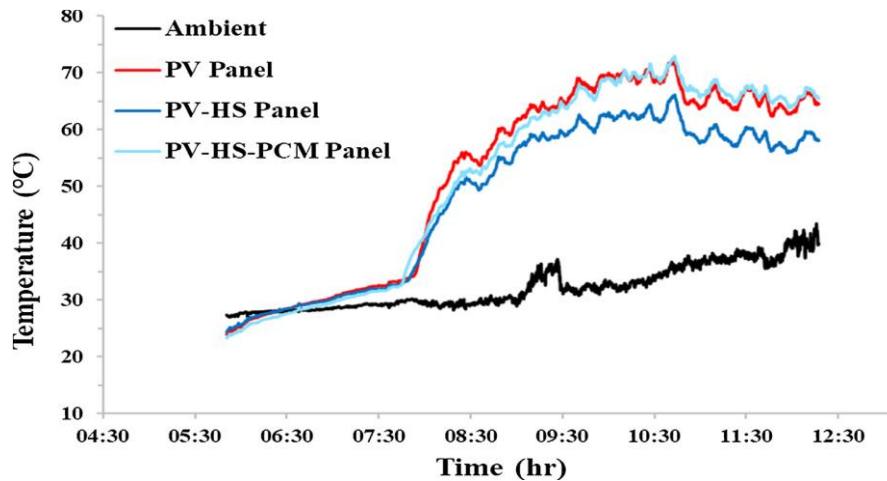


**Figure 2-8 PV Model of PCM with and without aluminium matrix with reference PV adapted from [86].**

Research conducted by [27] investigated the impact of various cooling methods on reducing the operating temperature of photovoltaic panels in Saudi Arabia. Specifically, their research examined how the performance of solar panels was affected by configurations that included heat sink passive cooling and a heat sink surrounded by PCM (Figure 2-9). Based on their results, a lower temperature was achieved for two hours, but as the PCM lost its cooling capacity after melting, the solar cell cooled using just a heat sink became more effective, as seen in Figure 2-10. After two hours, they reported an average of 10°C cooler for the heat sink configuration than the uncooled panel. They concluded that this cooling method is ineffective in locations such as Dammam, where the surrounding temperature could exceed 35°C throughout the year. Different cooling designs could overcome this limitation. However, the method might seem workable and convenient in moderate temperatures.



**Figure 2-9 PCM integrated with heat sinks adapted from [27]**



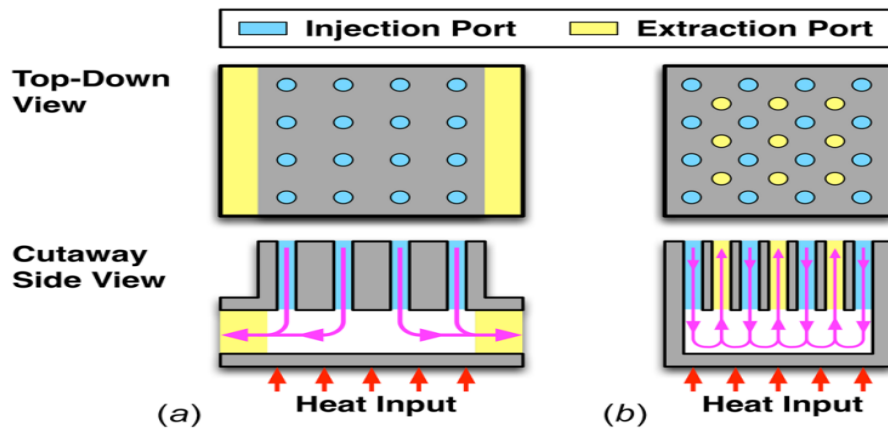
**Figure 2-10 Temperature variation of photovoltaic (PV), PV- heat sink, and PV-heat sink-PCM based on experimental results from [27]**

An article by [20] has stated that the cell temperature can be maintained between 28°C and 65°C by using PCM in combination with other forms of passive cooling. However, the main limitation of PCM passive cooling is that the PCM materials are toxic and corrosive, which is a cause for concern. Additionally, there are safety and disposal issues to consider at the end of the PCM product's life cycle. The amount of energy that can be stored by PCM thermal energy storage is usually limited by the material's specific heat capacity. To store large amounts of energy, either a large mass or a specific temperature interval is required. The system can complete the entire phase change in a short temperature interval, which means that it can use low-quality heat sources. When using PCM for cooling demands, it is necessary to consider the temperature interval of the material.

### 2.3.3 Jet impingement

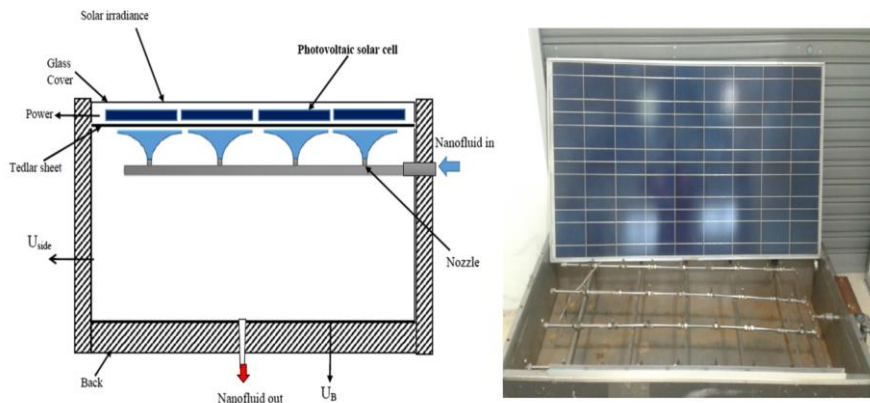
Impinging jets are a cooling method whereby coolant jets directly strike the surface and enhance coefficients for convective heat transfer. It has been reported that jet impingement is a promising technique for cooling CPV [7]. Impinging jet cooling is suitable for high sun concentration and high flux extraction. It can extract a high amount of heat and is used for an extended period in different fields. Researchers have stated that this is due to a decreased thermal boundary layer at the stagnation point. However, there is a decrease in the heat

transfer coefficient as the impinged liquid leaves the injected zone. In this type of cooling, the fluid is injected directly into the heat source utilizing nozzles. The cooling capability depends on the number of nozzles [87,88]. The spent fluid can be extracted at the edges of Figure 11a or using interspersed ports in Figure 2-11b [89]. The complex geometric features include the type of nozzle (rectangular or round nozzle), the nozzle's width, and the number of nozzles.



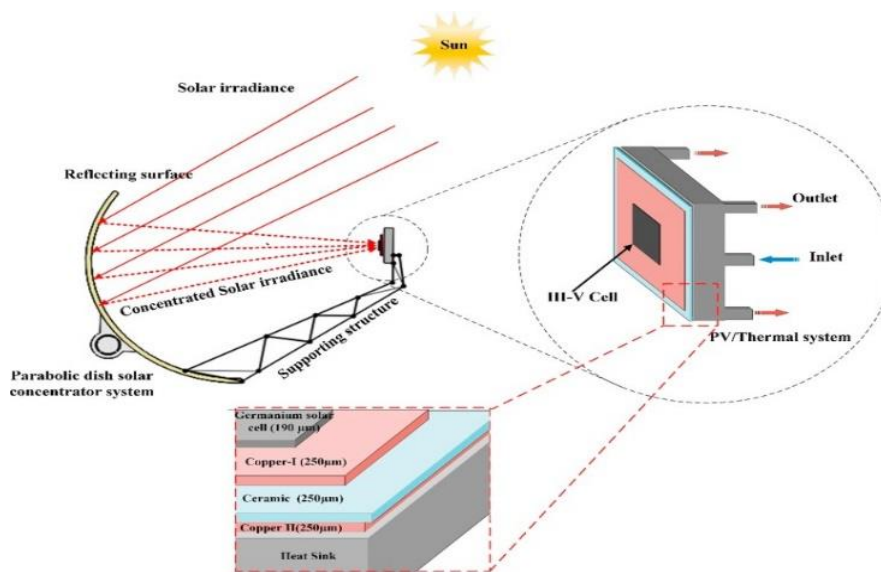
**Figure 2-11 Jet impingement cooling adapted from [89]**

Several studies have investigated the use of active cooling methods, such as jet impingements. For example, a study conducted by [90] used a dummy solar cell and found consistent cell temperatures at a flow rate of 0.049kg/s, with concentration ratios of 373 and 537 and a thermal resistance of  $6.2 \times 10^{-5} \text{ m}^2/\text{W}$ . Another study by [91] examined the electrical and thermal performance of using SiC, SiO<sub>2</sub>, and TiO<sub>2</sub> nanoparticles with water as the base fluid in a system comprising four tubes and 36 injection nozzles that inject fluid directly into the back of the panel collector (Figure 2-12). The average temperature of the solar panel absorber plate was used to determine the power conversion efficiency of the PVT collector. The study reported that water/SiC nanofluid demonstrated 85% thermal and 12.75% electrical efficiencies. The experiment was conducted at a solar irradiance of 1000 W/m<sup>2</sup>, a flow rate of 0.167kg/s, and a surrounding temperature of 30°C.



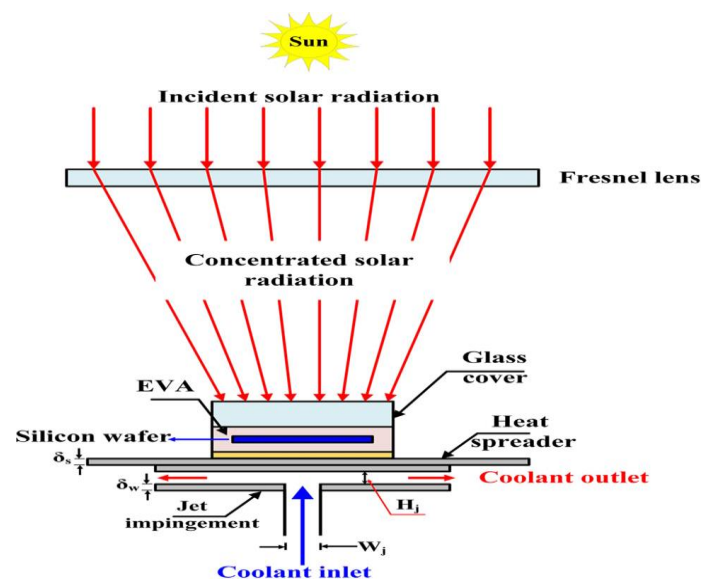
**Figure 2-12 Jet impingement cooling sketch of a side view and experiment set-up adapted from [91]**

Another study by [7] developed a model to investigate jet impingement heat sinks using a triple-junction solar cell with a thermo-fluid. The findings demonstrated that the solar cell's efficiency improved with increasing coolant flow rate and that jet impingement configurations could achieve sufficient temperature uniformity. They highlighted that jet impingement configurations required only 1% pumping power from the solar cell's generated power. Based on their model, the single jet configuration (Figure 2-13) reduced the total local temperature to approximately 65°C from a projected temperature of 1360°C. The single jet design exhibited the highest total exergy efficiency of 53.25%, as determined by energetic analysis.



**Figure 2-13 Jet impingement cooling model adapted from [7]**

Research conducted by [92] modelled a micro-channel heat sink and jet impingement integrated with a heat spreader that was designed for a CPV system (refer to Figure 2-14). The model was solved numerically, and the results were validated. At a sun concentration (SC) of 20, the integrated cooling system achieved uniform silicon wafer temperature distribution with the lowest average temperature compared to other designs. This study demonstrates the efficacy of integrating CPV passive and active cooling techniques.



**Figure 2-14 Diagram of CPV, microchannel integrated with Jet impingement heat and spreader adapted from [92]**

An analytical investigation by [93] has been reported, analysing the efficiency of a photovoltaic-thermal air heater with a jet plate reflector featuring 36 holes. A hybrid bifacial PV system with a jet plate reflector was presented as a novel design. The study reported a packing factor of 0.5 and 0.66 for 12 PV cells. The maximum thermal efficiency obtained was 51.09%, and the highest possible electrical efficiency was reported as 10.73% [93]. When using impinging jets, there are complex geometric considerations to consider, such as determining the appropriate geometric features, such as the type of nozzle (rectangular or round nozzle), the nozzle width, the height from the nozzle exit to the surface, and the impingement area of the cell.

### 2.3.4 Liquid Immersion

An innovative way to cool down CPV systems is by immersing them in a stationary or circulating electrically nonconductive liquid, such as deionised or dielectric liquids. This type of cooling has been applied in different fields, including electronics and data centres. The advantages of immersion cooling (IC) are that the liquid is directly in contact with the CPV, offering a simple way to increase computing capacity and lower equipment, operating and maintenance costs by submerging the CPV entirely in a fluid tank [94]. The fluids remove heat through direct contact with the heat source, raising the fluid to its boiling point. Wang et al. reported that when PV is submerged in water, it improves performance and efficiency [95]. The vapour generated condenses and then falls back into the bath. Emerging two-phase cooling can reduce energy costs compared to conventional air cooling and has been suggested as a viable method to achieve high heat removal rates.

An experiment was performed by [96] to determine the optimal water depth for inserting the PV cell to attain the required level of cooling, as depicted in Figure 2-15. The findings demonstrated that the deeper the water depth, the lower the temperature of the photovoltaic cell and the higher the electrical efficiency of the PV cell. At a depth of 1cm, the PV achieved its highest level of electrical efficiency at 4.76%. This represents a 17.8% improvement in electrical efficiency compared to the PV operating at the water's surface.

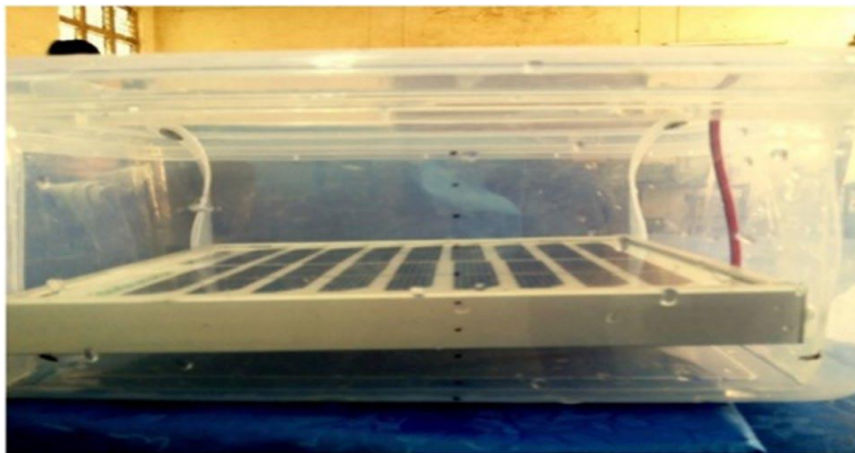
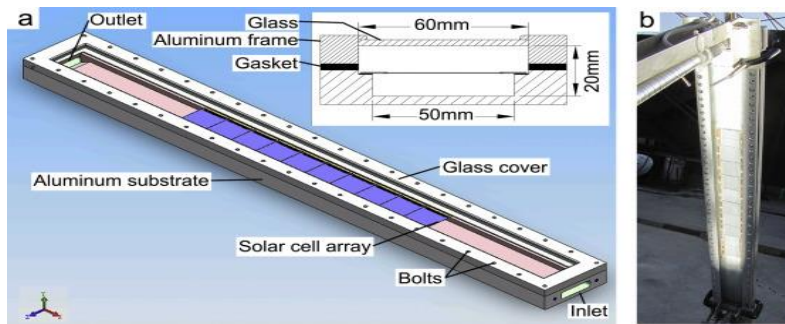


Figure 2-15 Immersed PV panel in water according to [96]



Several studies have been conducted on immersion cooling (IC). One study by [97] investigated the performance of submerged PV panels in water and found that the PV's surface temperature decreased, improving its electrical efficiency. In another study by [98], PV cells were immersed in deionised water using a two-axis dish concentrator tracking system. The results showed that the CPV was cooled to 45°C and 30°C at an irradiance of 920 W/m<sup>2</sup>, respectively. The performance of submerged PV panels was studied at various submersion depths by [99], and the results indicated that electrical efficiency decreased as the depth of the water increased. [100] reported temperature non-uniformity for immersion cooling on PV, and cooling using four different liquids was studied. The non-uniform temperature was observed to be 4°C, 17°C, 12°C, and 32°C using DI water, IPA, ethyl acetate, and dimethyl silicone oil, respectively. Under certain operating conditions, using these liquids for immersion cooling led to a low-temperature profile, increasing CPV output power.

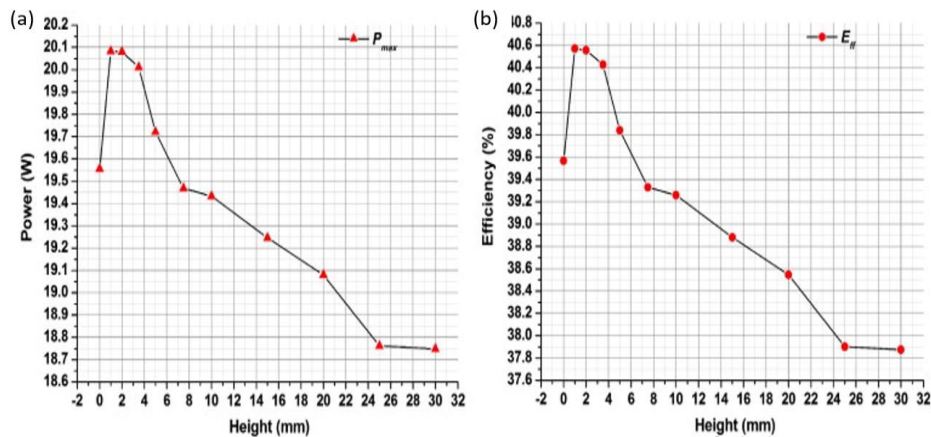
[101] reported using dimethyl silicone oil as an immersion liquid to directly cool CPV. To minimize the build-up of liquid, a receiver with a narrow rectangular channel was developed, as shown in Figure 2-16, and its thermal properties were studied under 9.1 suns concentration. Using real-time weather conditions, the results showed temperatures ranging from 20°C to 31°C at an irradiance of 920 W/m<sup>2</sup>. The cell temperature rose linearly with a 0–35°C silicon oil temperature change. Temperature variation along axial and lateral directions was less than 3°C, resulting in a consistent temperature distribution across the cell array. They reported that the configuration was stable for up to 270 days.



**Figure 2-16 Rectangular channel (a) Receiver model of the channel (b) Receiver on sun under actual conduction adapted from [101]**

In another study, [102] tested silicon PV cells in DI water, dimethyl silicone oil, ethyl acetate, and isopropyl alcohol (IPA). Higher concentration ratios produced higher power output in experiments with 10, 20, and 30 suns, and a 1.5mm liquid film increased cell efficiency by 8.5% to 15.2%. However, the PV cell performance was unstable when submerged at a depth of 9mm in deionised water. The study also highlighted that silicon CPV degradation was observed at 1.5mm, possibly due to silicone sealant, IPA, and ethyl acetate interaction.

[103] conducted research using a triple-junction PV cell submerged in dimethyl silicone oil at 500 suns. The experiments showed that cell electrical performance decreases with oil thickness, as depicted in Figure 2-17. Oil thickness of 1.0-30mm was studied, and the maximum output power and conversion efficiency of 20.083W and 40.572% were observed at an oil thickness of 1.0mm, respectively. Conversely, 39.567% and 19.556W were recorded when the oil thickness was greater than 6.3mm, indicating lower cell efficiency and output power.

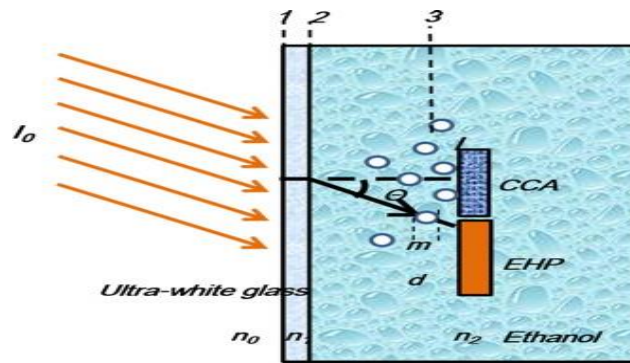


**Figure 2-17 Experimental results showing the effect of liquid thickness adapted from [103]**

An investigation into a high-concentrating photovoltaic system cooled using ethanol as an immersion liquid has been conducted [104]. Ethanol acts as a phase-change liquid immersion coolant. It was reported that the cooling system modulates and operates autonomously without consuming additional energy under concentration ratios ranging from 219.8 to 398.4 suns. The experimental results demonstrated that the surface heat transfer coefficient of the PV cell was



as high as  $46.98 \text{ kW/m}^2 \cdot \text{K}$  under 398.4 suns. However, it was highlighted that a decline in electrical performance was observed due to the formation of bubbles, resulting in light loss within the ethanol, as depicted in Figure 2-18. The current and maximum power of the triple-junction PV cells dropped by 10.2% and 7.3%, respectively.

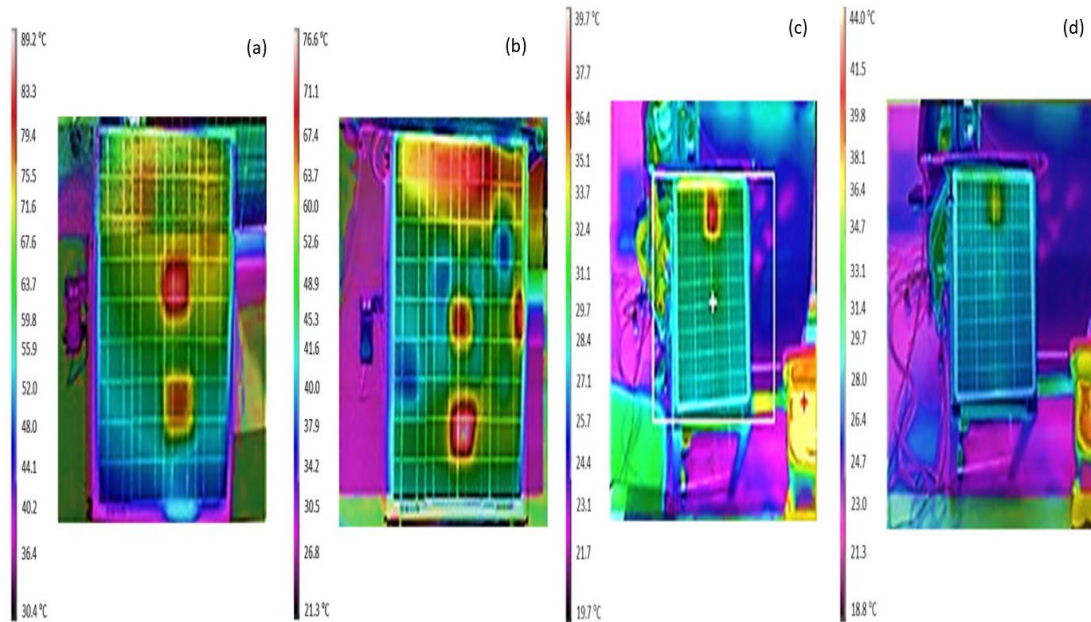


**Figure 2-18 A model bubble demonstration effect due to light-adapted from [104].**

Research conducted by [105] investigates the impact of continuous water flow-cooling using a lab test rig under  $87.38$  to  $359.17 \text{ W/m}^2$  solar radiation. Results demonstrate that the use of different coolant flow rates (3, 5.3, and 6.2 L/min) in the cooled PV system increases energy production by 18% compared to the uncooled system. In continuous feeding, 0.6 L/min resulted in a 29% power increase.

Research in [27] examines the impact of various immersion cooling approaches on decreasing the operating temperature of photovoltaic panels in Saudi Arabia. Specifically, the research investigates how the performance of solar panels is affected by various configurations (both immersed and non-immersed). Four panels were utilized to test the use of ethylene glycol, water, and engine oil as immersion fluids. The paper reported that the maximum average temperature decreased by approximately  $13^\circ\text{C}$  without immersion fluid; however, red-hot spots were discovered on the solar panel surface, as depicted in Figure 2-19a-d. This obstacle was overcome using an immersion fluid mechanism, resulting in a consistent temperature distribution. Compared to the cooling performance without cooling, active cooling with heat pipes reduced the solar panel temperature by approximately 53%, 48%, 25%, or 21%, with water, ethylene

glycol, engine oil, and without immersion, respectively. In addition, the voltage increases of the solar cell cooled with combined heat pipes immersed in normal water improved by 13% relative to the uncooled panel. At the same time, there were 12.4%, 7.5%, and 5.9% increments for ethylene glycol, engine oil, and no immersion, respectively. The best temperature uniformity was observed with water as an immersion fluid, as depicted in Figure 2-19d.



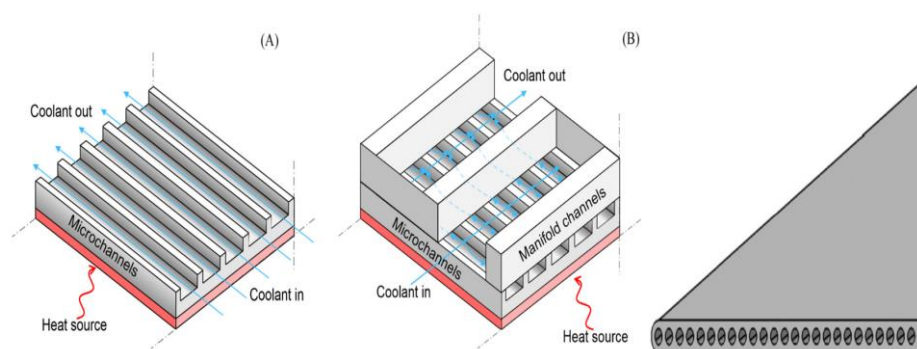
**Figure 2-19 Solar panel temperature distributions adapted from [27] (a) Uncooled (b) Non-immersed heat pipes with active cooling (c) Immersed heat pipes in ethylene glycol (d) Immersed heat pipes in normal water**

The liquid immersion cooling technique is suitable for high solar concentration ratios. However, in CPV cooling, its research potential is limited by a salt deposition issue. Other challenges must be resolved [25]. [20] states that the stable performance of photovoltaic strings when connected to electricity using immersion cooling is a future challenge. In general, limitations of immersion cooling include cell performance degradation, pressure drop, type of liquids, increase in weight, and design architecture.

### 2.3.5 Micro-Channel Cooling

The use of microchannel (MC) cooling is an innovative approach to cooling concentrated photovoltaic systems to achieve a higher heat transfer rate.

Microchannel technology has applications in various fields, including electronics, industrial heat exchangers [110–112], and solar cell cooling [113–115]. Microchannels can be open (for passive cooling) or closed (for active cooling), circular or rectangular, parallel, or a manifold (see Figure 2-20). The terms "microchannel" and "micro tube" are used interchangeably in heat transfer literature to refer to any flow channel with a hydraulic diameter of 1mm or less [116–118]. According to some studies, the microchannel cooling method can significantly and feasibly reduce the temperature of photovoltaic cells compared to other cooling technologies [114].



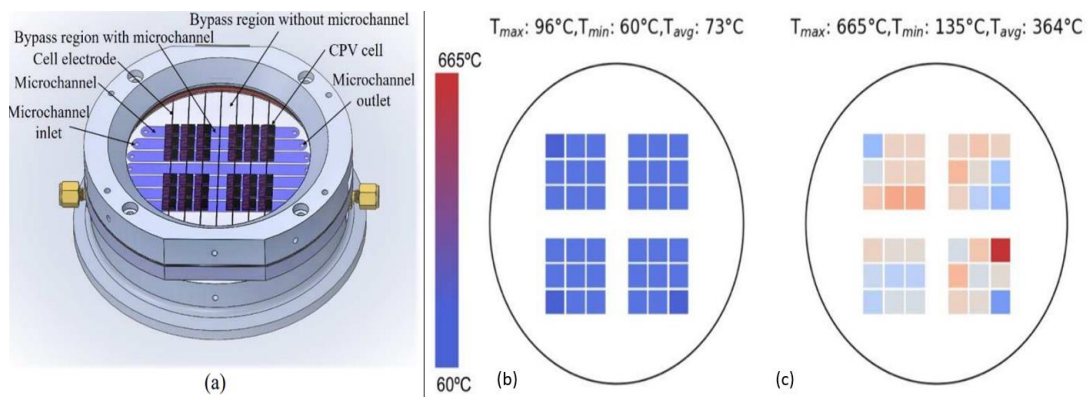
**Figure 2-20 Microchannel (a) Noncircular straight channel with noncircular manifold channel [62] (b) Circular channel [116]**

A numerical analysis of micro-channel cooling has been reported by [113]. A model of parallel microchannels was developed and optimized. Results show that microchannels provide high heat transfer, and the parallel flow configuration produces low-pressure drops along the channel. A temperature rise was observed along the micro-channel. Research shows that nanoparticles can enhance heat transfer and PV electrical efficiency in a parallel microchannel [119].

Research by [120] investigated CPV cooling techniques incorporating multi-layer manifold microchannels to improve surface temperature dispersion. The microchannel multi-layer manifold was tested with three solar cells in series. Under 28 suns, the CPV temperature dropped from 44.1°C to 20.4°C with a flow rate of 0.00535kg/s to 0.0232kg/s. A minimal surface cell temperature difference was reported to be less than 6.3°C. Microchannel cooling using water-AI\_2O\_3

and water-SiC nanofluids have been reported using 10, 20, and 40 suns concentration. It was found that water-SiC nanofluid reduced CPV temperature more than water-Al<sub>2</sub>O<sub>3</sub> nanofluid. The experiments showed that CPV/T systems could perform better using nanofluids than pure water, with PV temperature dropping to 38°C and 19% electrical efficiency [114].

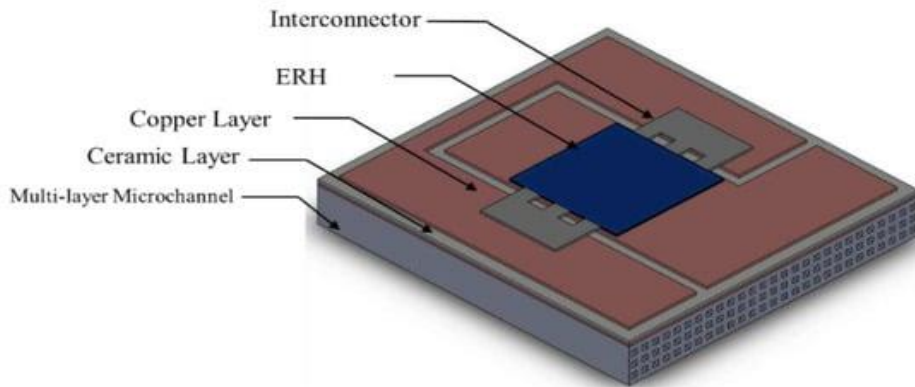
Research by [121] has been reported using seven parallel microchannels attached to CPV module cells. Optical flux map analysis and thermal modeling were used to predict the cooling system's performance. The module's performance attached to the cooling system was tested experimentally under different conditions. Results show that at 157 suns, the peak temperature of the cell was obtained to be 69°C (way below the maximum of 110°C). Their prediction shows that at 550 suns without active cooling, the cell temperature can reach up to 665°C (see Figure 2-21). A 13psi pressure drop across the microchannels with a maximum flow rate of 16.7 g/s, 4.3 m/s (Re=953) maximum microfluidic fluid speed, and  $1.7 \times 10^4$  W/m<sup>2</sup>K (Nu = 5.36) convection coefficient was reported.



**Figure 2-21 (a) Drawing of CPV module attached Microchannel (b) module flux pattern microfluidic cooling and (c) module flux pattern passive convection cooling adapted from [121]**

Findings from [122] suggest that microchannel multi-layered (MML) cooling is more thermally efficient than a single-layered system. The thermal behavior of a multi-layered microchannel was examined experimentally and numerically using a triple-junction solar cell. The results showed that increasing the number of layers from one to four reduced the temperature from 88.55°C to 73.57°C with a

30 W/cm<sup>2</sup> heating load and 30 mL/min coolant flow rate. The MML heat sink with a single layer had the most non-uniformity in temperature compared to those with a larger number of layers. An increase in the number of layers from one to four resulted in a decrease in pressure drop from 162.79 Pa to 32.75 Pa. The diagram of the MML is shown in Figure 2-22.

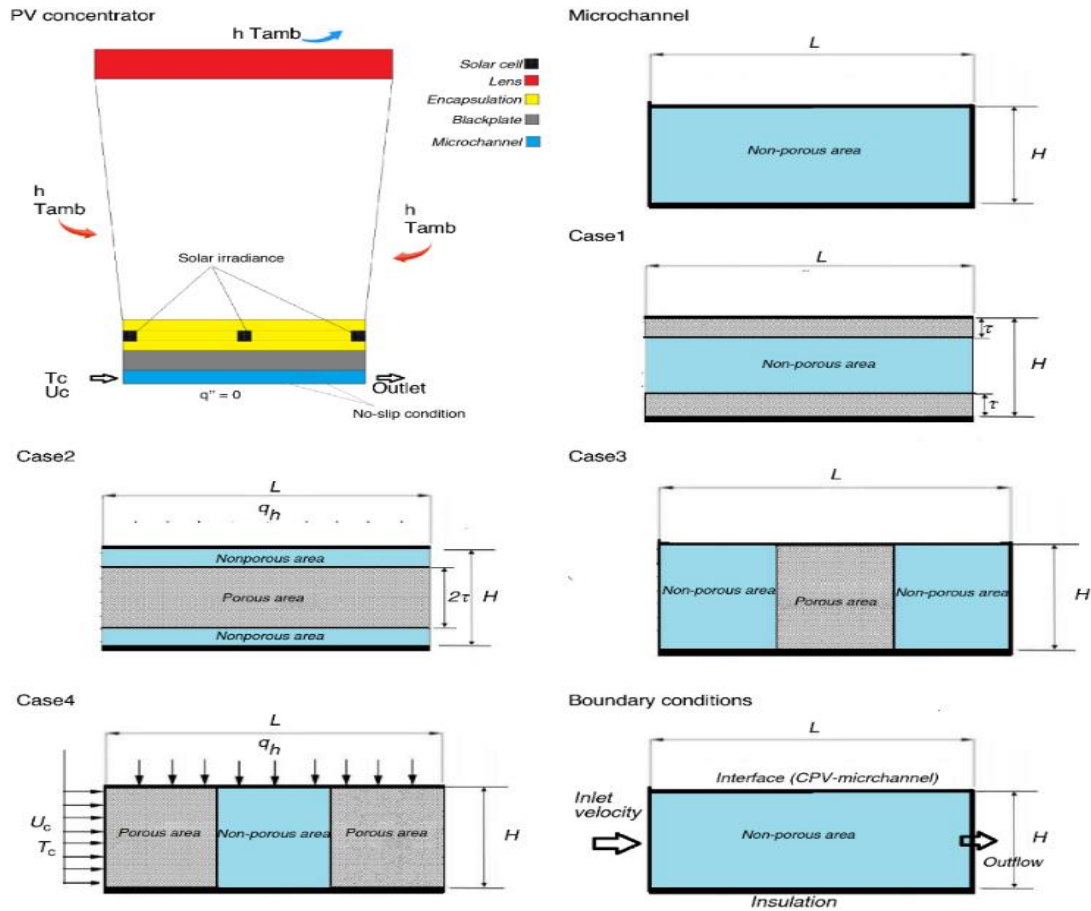


**Figure 2-22 CPV and multi-layer microchannel diagram adapted from [122]**

As highlighted by many researchers, clogging and photoresist residue formation are one of the primary causes of poor cooling performance in MC [123]. To address this, a proposed approach involves integrating microchannels into PV-device backside metallization. The approach includes evaporating a titanium and copper seed layer, and selectively electroplating copper around a photoresist microchannel pattern to avoid clogging and photoresist residues. In [124], it was reported that using nanofluids with carbon nanotubes can improve heat transfer, and it was suggested that they be used as working substances in a microchannel CPV/T system.

In [125], studies were conducted for CPV cooling with a microchannel-porous layer and CPV with fins using numerical simulation for four cases (Figure 2-23). The results show that the CPV-microsystem temperature of the CPV with a porous layer is much lower than in a CPV system with fins, which leads to about 10% of the CPV electrical efficiency. The effect of adding nanoparticles to the base fluid shows that the CPV temperature is lowered in the microchannel in all the cases considered. An increase in the nanofluid volume lowered the cell temperature by 1%-52% with an intensity 100-1000W/m<sup>2</sup>.





**Figure 2-23 Porous media and microchannel diagram for different cases adapted from [125]**

[126] investigated a microchannel double-layered heat sink to cool a CPV using a three-dimensional (3D) simulation model. The cooling orientations of parallel flow (PF) and counterflow were studied, as shown in Figure 2-24. Different sun concentration (SC) levels of 5, 10, 15, and 20 were considered using ethanol as a coolant. It was reported that an increase in the inlet flow rate lowered cell temperatures. The temperature uniformity index was best for the counterflow operation. The temperature uniformity index reported at 1200 ml/hr was 99.87% at SC 5 suns. At an SC of 20 suns, the average temperature of the silicon layer was reported to be 369.76 K at 200 ml/hr. This average temperature decreased by about 3.9% with a 1200 ml/hr increase in flow rate. Similarly, under SC 15, 10, and 5 suns, the average temperature drop in the silicon layer was reported to be 3.1%, 2.13%, and 1.9%, respectively. As such, 13.38% to 16.90% electrical

efficiency for PF operation and 13.19% to 16.86% for counterflow operation were achieved.

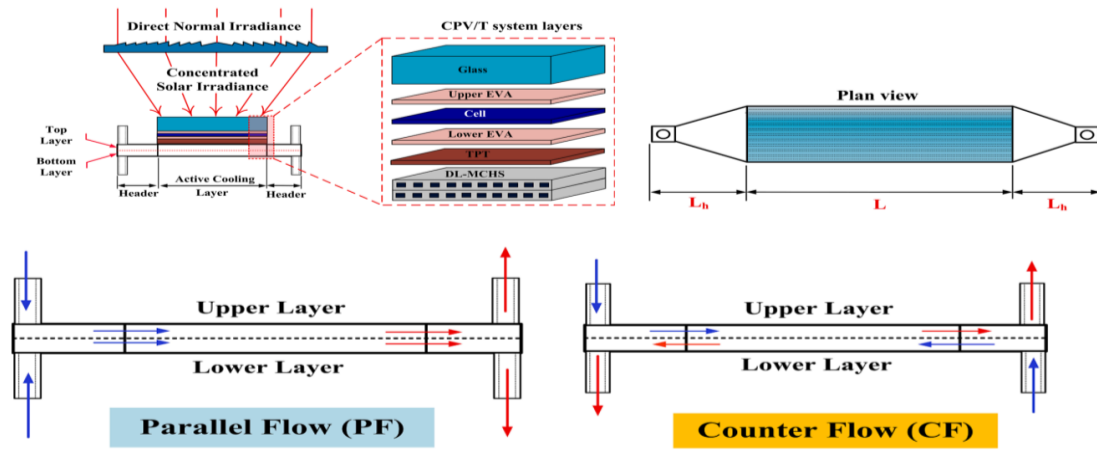
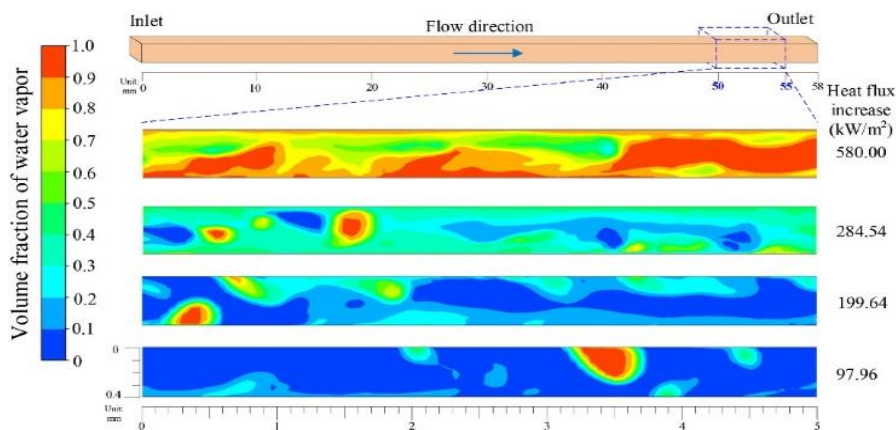


Figure 2-24 CPV and multi-layer microchannel diagram adapted from [126]

[127] investigated the effects of heat flux on transient two-phase flow in a microchannel. Numerical simulations were used to analyse the flow characteristics of deionized (DI) water in the microchannel under flow boiling conditions. The study reported that different heat fluxes resulted in variations in the flow patterns (refer to Figure 2-25). The results showed that as the heat flux increased from  $97.96 \text{ kW/m}^2$  to  $580 \text{ kW/m}^2$ , the vapour volume fraction increased from 0.104 to 0.8064, and the length of bubbles in the dry zone increased from 0.3 mm to 1.5 mm. At the same heat flux, the development period increased from 0.03 s to 0.066 s, and there was an increase in pressure drop from 2.43 kPa to 14.51 kPa, and the vapour volume fraction within the microchannel increased from 3.3 times to 25.6 times.



**Figure 2-25 CPV and multi-layer microchannel diagram adapted from [127]**

The one of the primary limitations of microchannel cooling for concentrated solar cells is its tendency to cause pressure drop, corrosion, temperature non-uniformity, higher manufacturing costs, and increased power requirement due to the coolant's larger pressure drop [20,25]. Specifically, pressure drop is the most significant challenge associated with using microchannels for CPV cooling [127].

## **2.4 Novel Approach to CPV Cooling**

The literature review indicates that concentrator photovoltaic (CPV) systems face the challenging task of maintaining cell temperature. Concentrating solar energy on a solar cell can increase its electrical and thermal output, but the thermal stresses caused by the concentration can also raise the cell temperature to levels that could damage the whole system. Thus, an efficient cooling mechanism is required for CPV to achieve higher net output power and run safely.

CPV cooling remains a challenging area for researchers to explore. Several studies have highlighted the non-uniformity of concentrated solar cell temperatures resulting in hot regions and cooled spots that need further investigation. Immersion cooling is limited by cell performance degradation, pressure drop, liquid type, weight, and design. Impingement jets pose challenges of temperature non-uniformity, spent fluid, and design complexity. Heat pipe cooling systems encounter overheating, reverse thermal flows, and area-dependent cooling issues. Phase change cooling has limits on storing energy, mass weight dependent on cooling capacity, and utilization of low-quality heat sources. Microchannel cooling faces fundamental limitations such as pressure drops, corrosion, temperature non-uniformity along the channel, higher manufacturing costs, and power consumption.

The current conventional cooling method for CPV works based on continuous flow, which increases the likelihood of non-uniform temperature distribution. Another challenge is the continuous fluctuation of solar radiation intensity due to uncontrollable conditions such as clouds, making it a significant obstacle since our environment is subject to changes depending on the weather.



This review proposes a novel approach to cooling CPV based on discontinuous flow inspired by human thermoregulation as a new research direction. To achieve this, the concept of the most sophisticated cooling system, the human body, is discussed in the following section to provide insight into the concepts.

### 2.4.1 Human Thermoregulation

The human body actively controls its temperature. Even when inactive, the body's system loses heat due to basal metabolism [128,129]. A faster metabolism produces more body heat [130]. However, it has been reported that the maximum body temperature is 40°C [130,131]. According to an article published by the Centre for Health and Social Care Research, Sheffield Hallam University UK, the hypothalamus regulates body temperature to maintain the whole body function. It is a brain processing center that regulates the body's temperature [129]. This is achieved by causing changes in the body's systems, such as the skin and muscles, and controlling hair. The four mechanisms responsible for transferring heat to the environment are radiation, conduction, convection, and evaporation of sweat [132]. Figure 2-26 shows the active human thermoregulation system adapted from the literature. However, the process involves much more than the cooling operation of CPV.

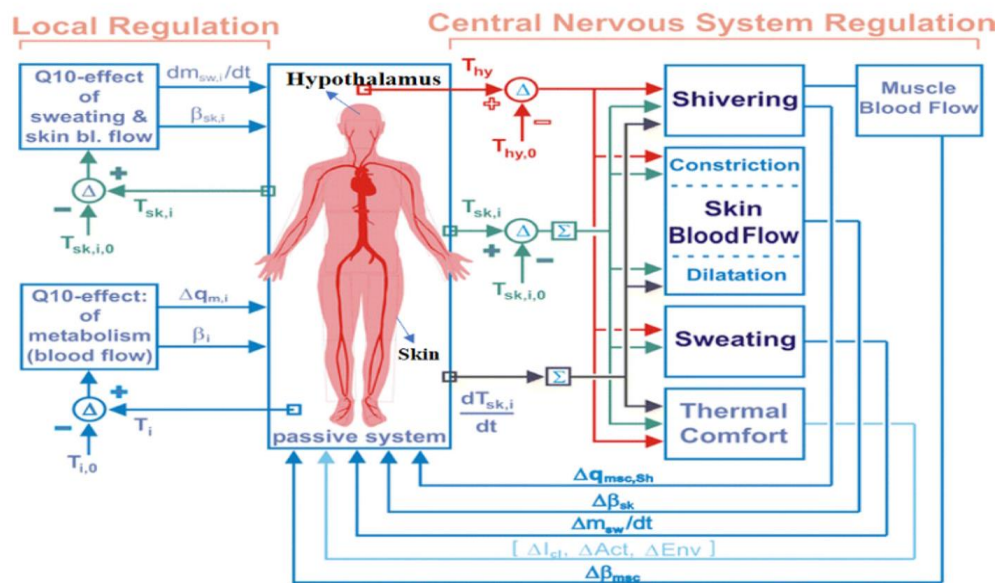


Figure 2-26 Human thermoregulatory system model diagram according to [133–135]

As shown in Figure 2-26, if a person's internal temperature is too high or too low, the processing center will send nerve impulses to the skin. The skin can increase or decrease the heat lost from the body surface in two ways. First, the hairs found on the skin are better at retaining heat. Second, the minuscule muscles found in the skin could quickly pull the hairs upright to reduce the heat lost or lay them down flat to increase the heat lost. In addition, if the body's internal temperature is too high, glands in the skin will produce sweat, which will then be secreted onto the surface to increase the heat lost through evaporation [132–135]. This cools the body.

As the body temperature normalizes, sweating slows. When the environment is warm, blood vessels dilate or swell to maintain the supply of warm blood to the skin. This allows blood to flow nearer or farther away from the skin's surface, depending on the environmental condition. In addition, rapid muscle contraction causes heat to be produced during shivering in a cold environment. It warms surrounding tissues, giving the body a comfortable temperature [129,133–135].

It has been reported that the blood temperature in the human body continually changes as it flows [136]. The heart is responsible for circulating the blood with continuous fluctuation in velocity and blood pressure at regular intervals [137,138]. Pulsatile blood from the heart changes speed and pressure [137]. This means that the time-varying velocity, blood flow pressure, and circulation of the body depend on environmental conditions. Research shows that pulsating flow enhances heat transfer [139–143].

The hypothalamus appears to be a key temperature sensor that integrates information from other body parts in the form of sensors. The hypothalamus happens to be the body's thermostat. The body's metabolic rate and temperature rise when exposed to cool air. The body increases its metabolic rate in a cooled environment to produce an elevated body temperature. On the contrary, when the body is exposed to a warm environment, the hypothalamus triggers responses to maintain the body temperature. The heart circulates blood at varying speeds and pressures in a pulsating flow. The blood flows and temperature are reportedly time-varying depending on environmental conditions.

Several research studies have shown that pulsating flow increases heat transfer. These concepts can be applied to CPV cooling using solenoid valves and controls to improve thermal transfer. These will bring about some control to tackle solar radiation intensity fluctuation since the CPV temperature changes depending on the environmental weather or cloud. The following section provides a discussion on pulsation flow.

### 2.4.2 Pulsating Flow

Blood flow is crucial for maintaining human life, and the body's biology is based on pulsatile flow, which is determined by the heartbeat [144]. The heart's beating action generates a pulse flow, and the flow speed varies significantly throughout a single heartbeat. The lining of the arteries contains receptors that are sensitive to the pulse's strength and respond to changes in pulse strength by signalling for the constriction or dilation of capillaries, thus achieving proper blood distribution within the body. Research reported by [145], using a corrugated tube to enhance heat transfer inspired by a fish vascular heat exchanger, has been reported. The corrugated tube's cross-section varies with a constant hydraulic diameter to mimic flow-changing behavior in fish. Improvement in heat transmission at a minimal pressure drop has been observed. Figure 2-27 shows the heat flux plot for straight and corrugated pipe flow. Experimental results have shown that corrugated tubes increase the Nusselt number by 500% compared to straight tubes. The corrugated tubes' thermo-hydraulic performance is 160% higher than that of straight tubes.

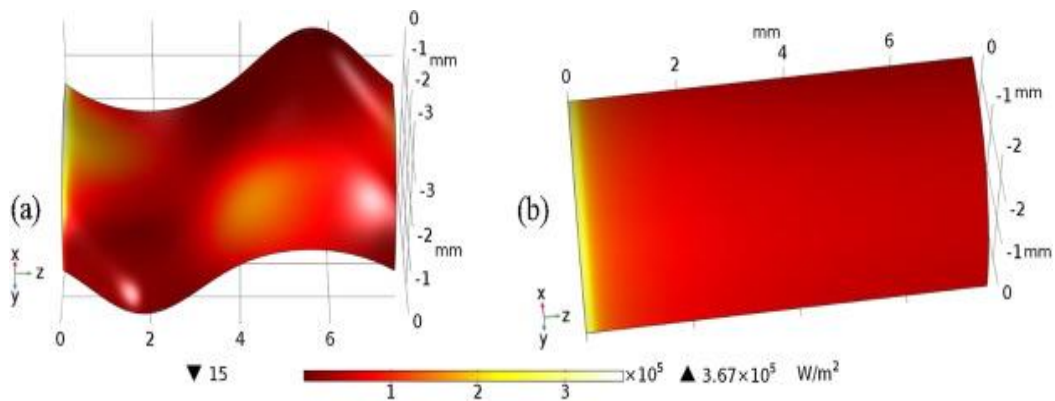
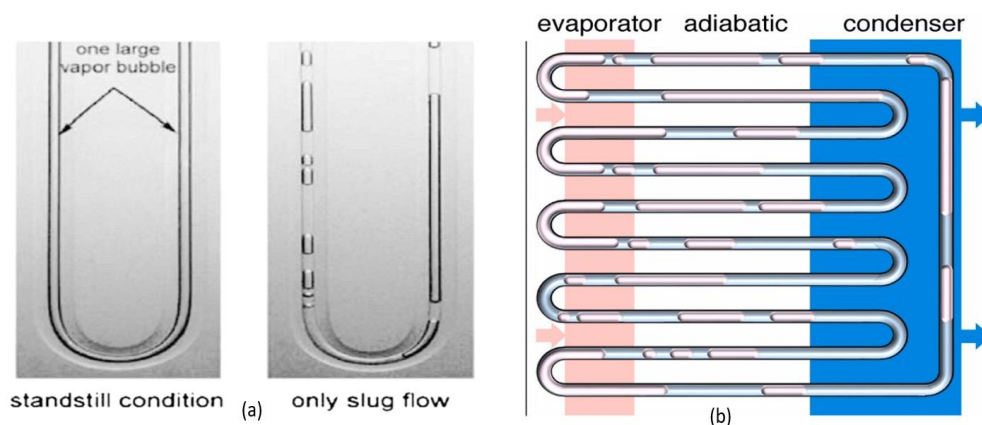


Figure 2-27 Heat flux in a straight pipe and corrugated tube adapted from [145]

Pulsating heat pipe technology has been used in electronic devices and electrical components to enhance heat transfer using two-phase liquid. It was introduced in the 1990s as an oscillating heat pipe [146]. [50] reported that pulsating heat pipes are applied for cooling electronic equipment within a short distance or where space is relatively compact. Researchers suggested that the heat pipe is filled with a fraction of 40-60% of the heat transfer working liquid in a small capillary tube diameter [50,147,148]. The phase change liquid boils or evaporates, causing pressure increase in the section where heat is applied. Due to the pressure difference, the vapor in the heating section moves to the cooling liquid section, and the liquid cooling moves to the heating section (Figure 2-28). These processes continue to happen, making the liquid in the tube continuously oscillate. This process forms a pulsating flow within the two sections of the tube. The advantages of heat pipe pulsating flow include less weight since it requires a fraction of liquid and air within the tube and works with a smaller diameter [50]. Pulsating heat pipes (PHP) are an emerging subject of study for researchers, with dozens of articles published each year. However, limited knowledge of their performance and a lack of scientific modelling tools restrict practical application [147].



**Figure 2-28 Looped pulsating heat pipe (a) Glass showing fluid and air [149] (b) Process diagram adapted from [147]**

It has been demonstrated that the flow pattern within PHPs switches from an oscillatory pattern to a circulation pattern, ultimately enhancing overall thermal performance [150]. An experiment was carried out using a high-speed camera to

visualize PHP flow. It was reported that an increase in the channel's inner diameter shifted the flow pattern from an oscillatory pattern to a circular form, which correlated with an increase in thermal performance [151]. Several researchers have reported that shifting pulsating flow to circular flow increases the base and helps vapour plugs from the evaporation section to recirculate more, enhancing thermal performance [151–155].

## **2.5 Summary**

Continuous flow in cooling creates a boundary layer that hinders heat transfer [156]. Pulsating flow may boost heat transfer by disrupting the boundary layer and mixing the fluid [157]. Pulsation flow is transient, adding complexity to analytical investigation [158,159]. Many modelling and computational fluid dynamics studies are available in the literature. However, experimental work is limited due to inadequate technology to measure pulsating properties. Velocity measurement is more challenging in pulsed flow than in continuous steady flow. However, with research and development over the years, technology has improved to address these challenges [159]. Another challenge is that flowmeters cannot record exact results at high frequencies due to their weak reaction time. Temperature prediction is also highlighted as a challenging task [159]. Important parameters to consider in pulsating flow include frequency, amplitude, axial position, relaxation time, pulsation source, Womersley number, Reynolds number, distance, and Nusselt and Prandtl number all impact heat transfer in pulsating flow [160]. [127] reported that transient heat flux in CPVs leads to flow regularly boiling in microchannels; therefore, more work needs to be done to have some control technology [127]. Lack of control parameters in boiling and irregular oscillation is still a challenge in boiling and PHPs. With current research and development, using valves to control the nature of the oscillation is an area to explore.










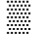
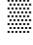




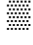





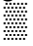
Based on the literature search, cooling with pulsations has not been applied to CPV cooling. Based on the articles reviewed in this paper, bio-inspired fluid flow, like human thermoregulation, increases heat transfer. Researchers working on CPV cooling can consider integrating pulsating flow into the existing CPC cooling

techniques to enhance heat transfer. Some articles that provide detailed information on pulsation flow include [61,137,144,148–150,152,161].

The most critical problem to solve in concentrated PV to boost photoelectric efficiency and protect the solar cell is the cooling problem. Concentrated photovoltaic (CPV) increases efficiency and power output, which comes with an overheating problem due to the high intensity of concentrated radiation. A cooling mechanism to get rid of heat efficiently needs to be developed to encourage more people to use CPV technology. Many CPV cooling techniques are available, classified as active or passive, using air or water cooling. Passive cooling is simple, with zero or low energy requirements. However, this type of cooling is suitable only for low to medium concentrations. Active cooling is best for high-concentration systems. However, temperature non-uniformity and other challenges have made it hard to stick to existing cooling methods. As such, CPV cooling has been receiving more and more attention from researchers in recent years. Reverse thermal flows and area-dependent cooling capacity are all concerns in heat pipe cooling systems.

In PCM cooling, the specific heat capacity of PCM thermal energy storage limits how much energy it can store. As a result, it can operate on low-quality heat sources. When it comes to impinging jet cooling, there are many complex geometric considerations, such as the type of nozzle (rectangular or round) and the nozzle width. For high solar concentration ratios, liquid immersion cooling is a good option. Cell performance degradation, pressure drop, type of liquids, increased weight, and design architecture are all associated with immersion cooling limitations. Pressure drops, corrosion, temperature non-uniformity along the channel, higher manufacturing costs, and more power requirements due to coolant pressure drops are the main limitations of microchannel cooling on concentrated solar cells. More research is required on the economic viability of CPV cooling. Table 2-3 summarizes research availability limitations and current challenges of CPV cooling.




**Table 2-3 Challenges in CPV cooling**

Limitations and Challenges in the Existing method of CPV cooling			
Cooling Technique	Method of Study	Concentration	Main Challenges
Heat Pipe and Fins	Experiment  Theoretical  Numerically  Simulation 	Lower Medium High*	Overheating, uncontrollable oscillatory thermal flows, reverse thermal flows, area-dependent cooling capacity, temperature non-uniformity
PCM	Experiment  Theoretical  Numerically  Simulation 	Lower Medium High*	Limited cooling capacity at higher concentrations, limited amounts of heat energy storage, acidic nature, issue of disposal after lifetime used, mass/weight cooling capacity dependant
Jet Impingement	Experiment  Theoretical  Numerically  Simulation 	Lower Medium High	System design complexity, draining spent flow, temperature non-uniformity, manufacturing costs
Immersion Liquid	Experiment  Theoretical  Numerically  Simulation 	Lower Medium High	Salt deposition issue, cell performance degression, pressure drop, type of liquid, increased weight, design architecture
Microchannel	Experiment  Theoretical  Numerically  Simulation 	Lower Medium High	Pressure drops, corrosion, temperature non-uniformity, higher manufacturing costs, more power requirements, more studies are needed to commercialise
<p>Level of Research Reported in CPV cooling: -   = Good number of study available       = Limited number of study available                      Level of Concentration ©:  <i>Lower:</i> - <math>C &lt; 20</math> suns, <i>Medium:</i> - <math>20 &lt; C &lt; 100</math>, <i>High:</i> - <math>C &gt; 100</math>.      *With a hybrid system configuration</p>			




One promising method to enhance thermal performance is by using nanofluids. However, there are limitations, such as high cost, corrosion problems, pressure

drop, sedimentation, and agglomeration. Researchers have been studying hybrid CPV technology to improve electrical and thermal performance. A hybrid system, such as jet impingement cooling, microchannels, or impingement cooling, and heat pipes, facilitates a high heat dissipation rate in concentrated systems. Integrating a heat recovery system into a CPV thermal system can also increase the capabilities of CPV cooling. Using the Organic Rankine Cycle (ORC), maximum waste heat utilisation can create a win-win situation between cell temperature reduction and system output enhancement. Several restrictions exist on concentrated photovoltaic/thermal (CPV/T) hybrid systems. Design complexity in incorporating two or more methods remains a challenge for researchers. The initial cost of installing the proposed system's components is greater than that of conventional power systems, limiting the system's economic viability. The compatibility of components within a single system is another challenge. The availability of platforms and integrated model packages to investigate different hybrid systems to minimise experiment costs and errors is also a challenge. Table 2-4 summarises the research gap and limitations of the current CPV heat transfer enhancement approach.


**Table 2-4 Heat transfer enhancement approach in thermal energy management**


<b>MHTE Approach</b>	<b>Area of Approach</b>	<b>Current State of Art</b>	<b>Research Gap and Limitations</b>
Use of Nanofluid	Type coolant		Corrosion problems, stability issues, sedimentation issues, agglomeration issues, pressure drop, high cost
Hybrid Cooling	Overall system		Compatibility issues, cost economic viability, integrating components within a single system
Boiling Heat Pipes (PHP)	Phase change liquids		Limited modelling tools, no flow pattern control, little experimental work, and availability of components to measure flow.

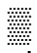



Magneto hydrodynamics (MHD)	Type coolant and overall system		Limited experimental work, more numerical models and simulations research are required, and additional cost
Electro Osmotic Flow (EOF)	Porous material under the influence of an electric field		Limited modelling tools, effects of channel geometries on the EOF, design optimisation
Pulsating Flow	Flow and overall system		Limited theoretical study, more research is needed combined with porous media, contradicting results, additional cost due to using of solenoid valves, other means to provide pulsation can be explored, may lead to system complexity

Level of Research Reported: -

 = Applied to CPV cooling, and a good number of studies are available

\* = Good number of studies available with limited research in a ground couple/ ORC systems

 = Limited number of studies are available and have been in the field of electronics

 = Study is available mainly in the field of medicine, electronics, and mechanical engineering but has not been applied to CPV cooling

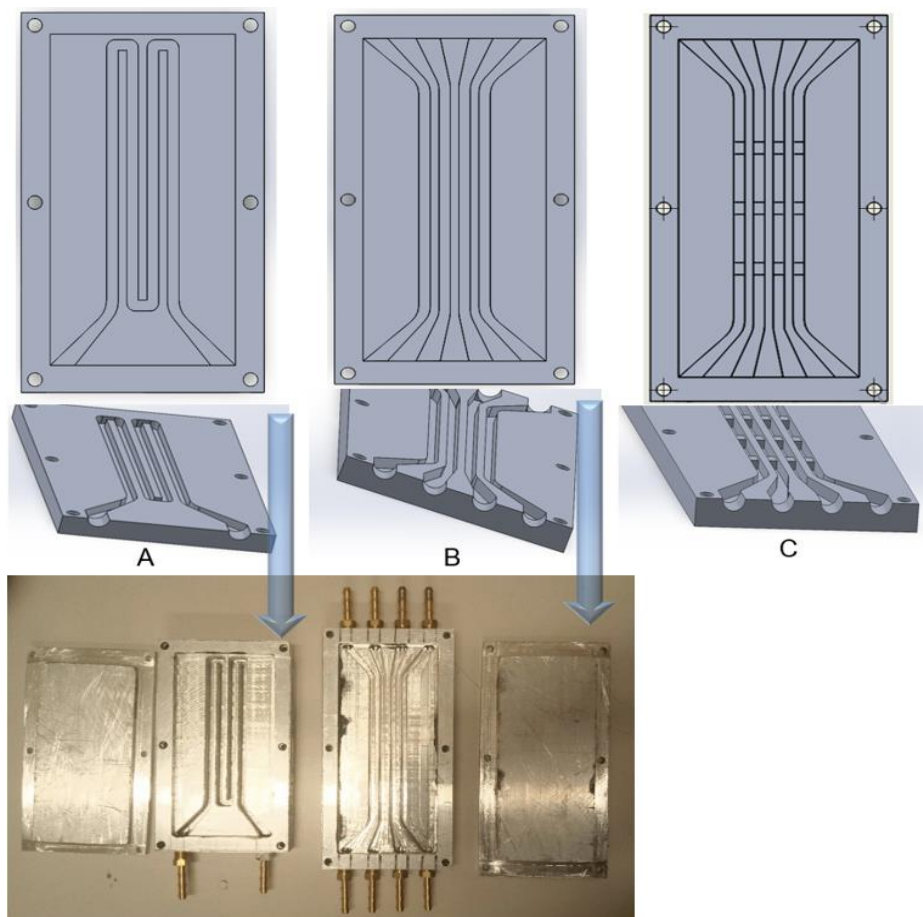
## 3 CHAPTER THREE

### 3.1 Methodology

This section discussed the model design, including its specifications and dimensions. The model used for simulation was fabricated and used for the experiment. Both simulation and experiment methodology adapted in this research are discussed.

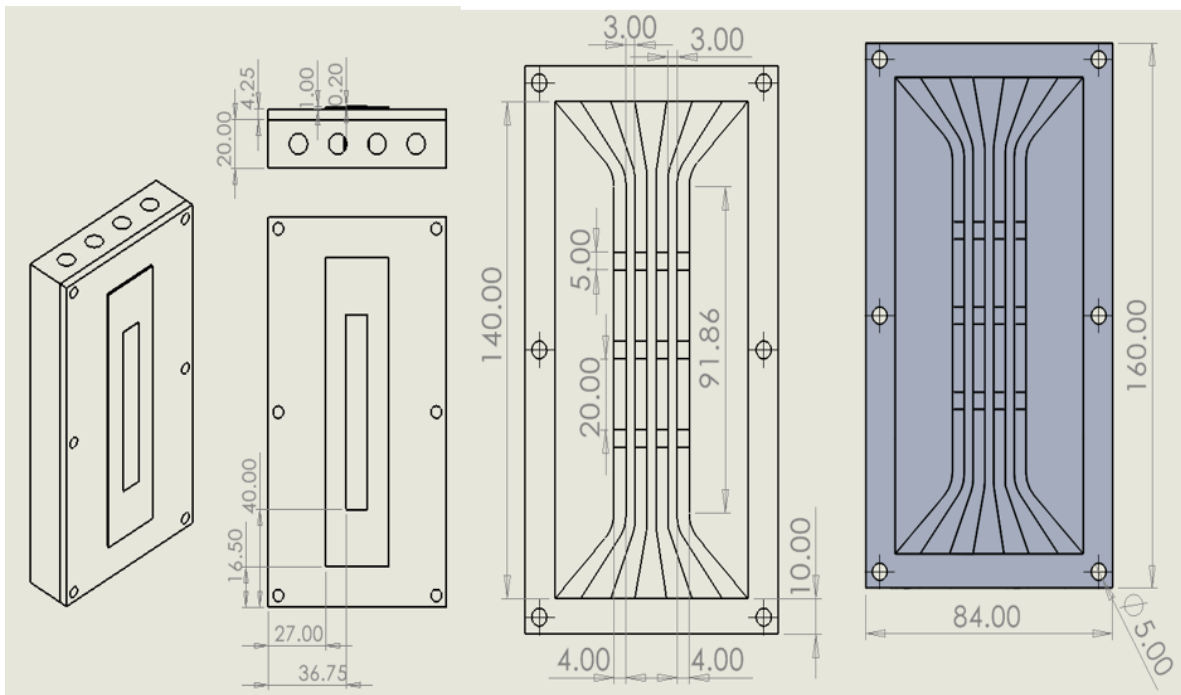
#### 3.1.1 Design And Specifications

Three cooling block model channel designs were considered (Figure 3). A 3D model design was developed using computational fluid dynamics to investigate pulsing flow into CPV. The model design was created using SOLIDWORKS, and Ansys Fluent software was used for the analysis.



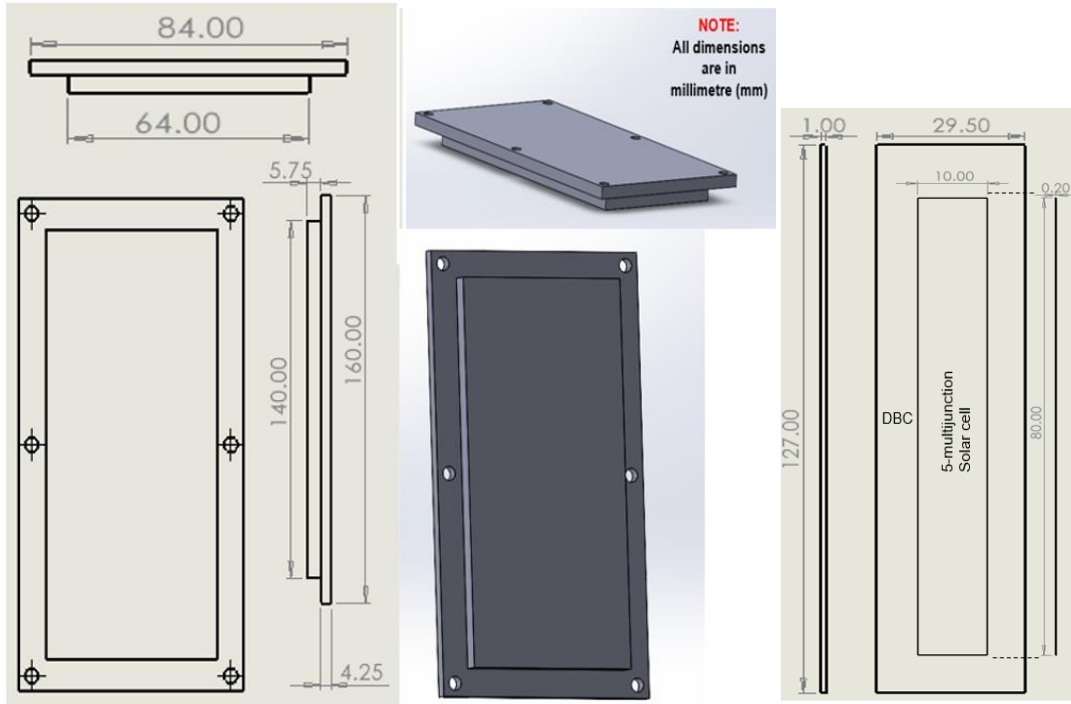
**Figure 3-1 Model chanel view (A) Conventional snake-type channel design (B) Parallel channel design without baffles and (C) Parallel channel design with baffles**

The conventional snake-type channel design (Figure 3-1A Top), parallel channel design without baffles (Figure 3-1B Top), and parallel channel design with baffles (Figure 3-1C Top) were considered for the simulation. While the conventional snake-type channel design (Figure 3-1A bottom) and the parallel channel design without baffles (Figure 3-1B bottom) were built and used for the experiment. The design dimension was the same for all three designs considered. The cooling block sketch design and dimensions adapted for both simulation and experiment is shown in Figure 3-2 below (all dimensions are in millimetre).



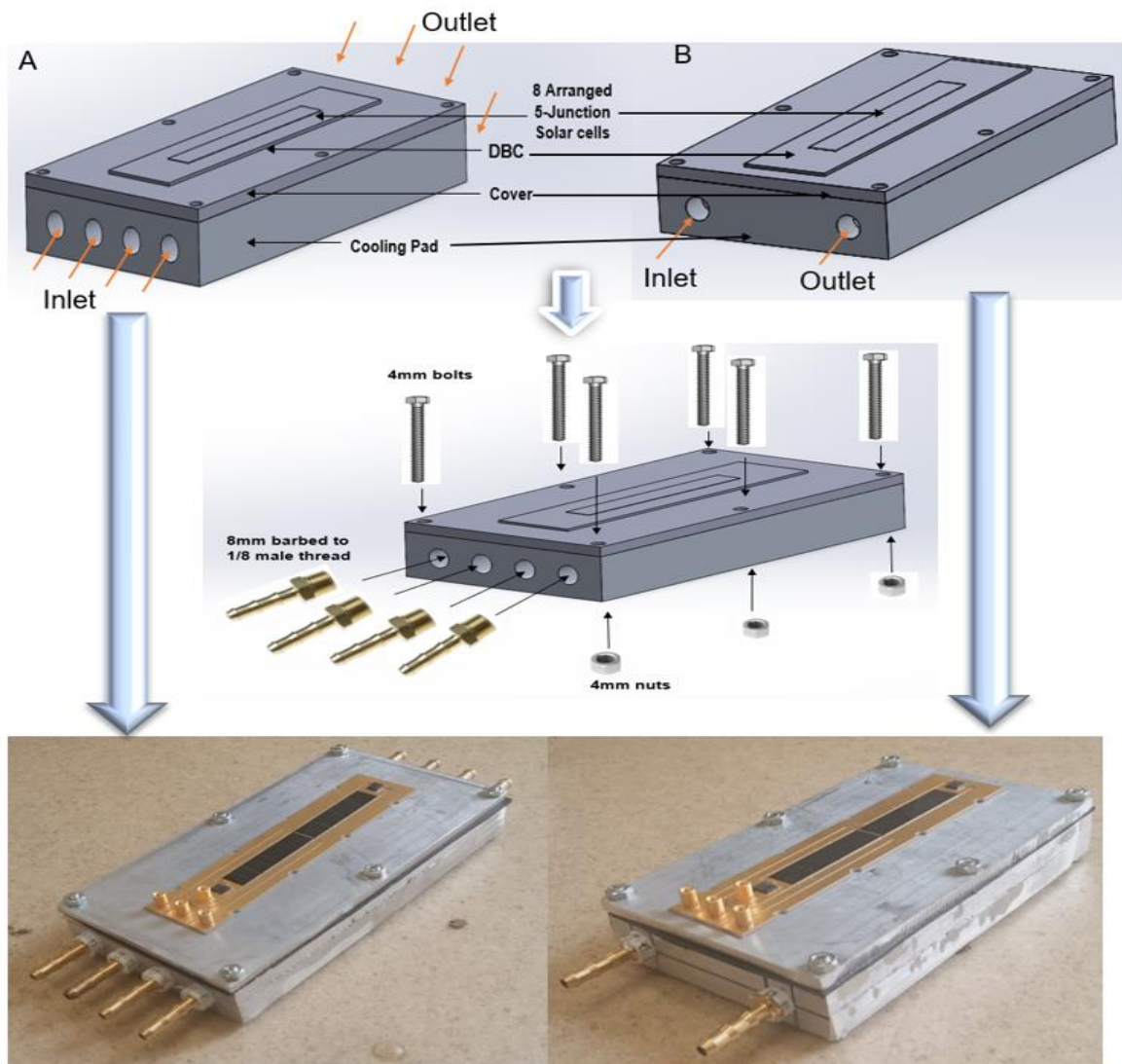
**Figure 3-2 Model sketch and dimensions.**

Figure 3-3 shows the sketch and dimension of the model cover (Figure 3-3 Left) and the multijunction solar cell (Figure 3-3 Right).



**Figure 3-3 Model cover and 5-multijunction solar cell sketch with dimensions.**

The complete coupled 3D model is shown in Top-Figure 3-4A (Parallel channel designs used for simulation) and Top-Figure 3-4B (Conventional snake-type channel design used for simulation). Bottom-Figure 3-4A and Bottom-Figure 3-4B shows the actual coupled model built using a three-axis Computer Numerical Control (CNC) machine. An aluminium 6082T6 flat plate material was used because it is compatible with the CNC machine. Six 4mm bolts and 4mm nuts were used in each model to couple the cover and the cooling pad (cooling block). Eight 8mm barbed were used as fittings for the inlet and outlet in the Parallel design and conventional design.



**Figure 3-4 Complete coupled simulation 3D model (A and B top) and experimental coupled built model (A and B bottom)**

The complete cooling pad design, detailed specification, and solar cell dimensions considered for both simulation and experiment are shown in table 3-1. Moving from bottom to top in Figure 3-5, a detailed channel view is shown based on the design considered. The Inlet/outlet is circular to provide provision of using inlet/outlet fittings in the actual built model during the experiment. The flow from the Inlet having a circular area  $A$  would flow through the first rectangular section having a rectangular area  $A_1$  and then proceed to the actual straight rectangular channel with area  $A_2$ . In each section with constant flow rate  $Q$ , as shown in equation 3-1, the velocity and Reynolds number will change due to the

change in the area, like the hydraulic diameter. As such, a flow rate of  $Q$  with inlet area  $A$  and velocity  $V_{inlet}$  will change to  $A_1 V_1$  along rectangular section 1 and  $A_2 V_2$  along the straight rectangular section 2 (Figure 3-5).

$$Flow\ Rate\ (Q) = \frac{Volume\ Ad}{Time\ t} = Av \quad (3-1)$$

Since,  $Q_{Circular\_Inlet} = Q_{Rectangular\_Channel1} = Q_{Rectangular\_Channel2}$   
 then,  $Q_{Circular\_Inlet} (Av_{Inlet}) = A_{1\_channel} v_{1\_channel} = A_{2\_channel} v_{2\_channel}$

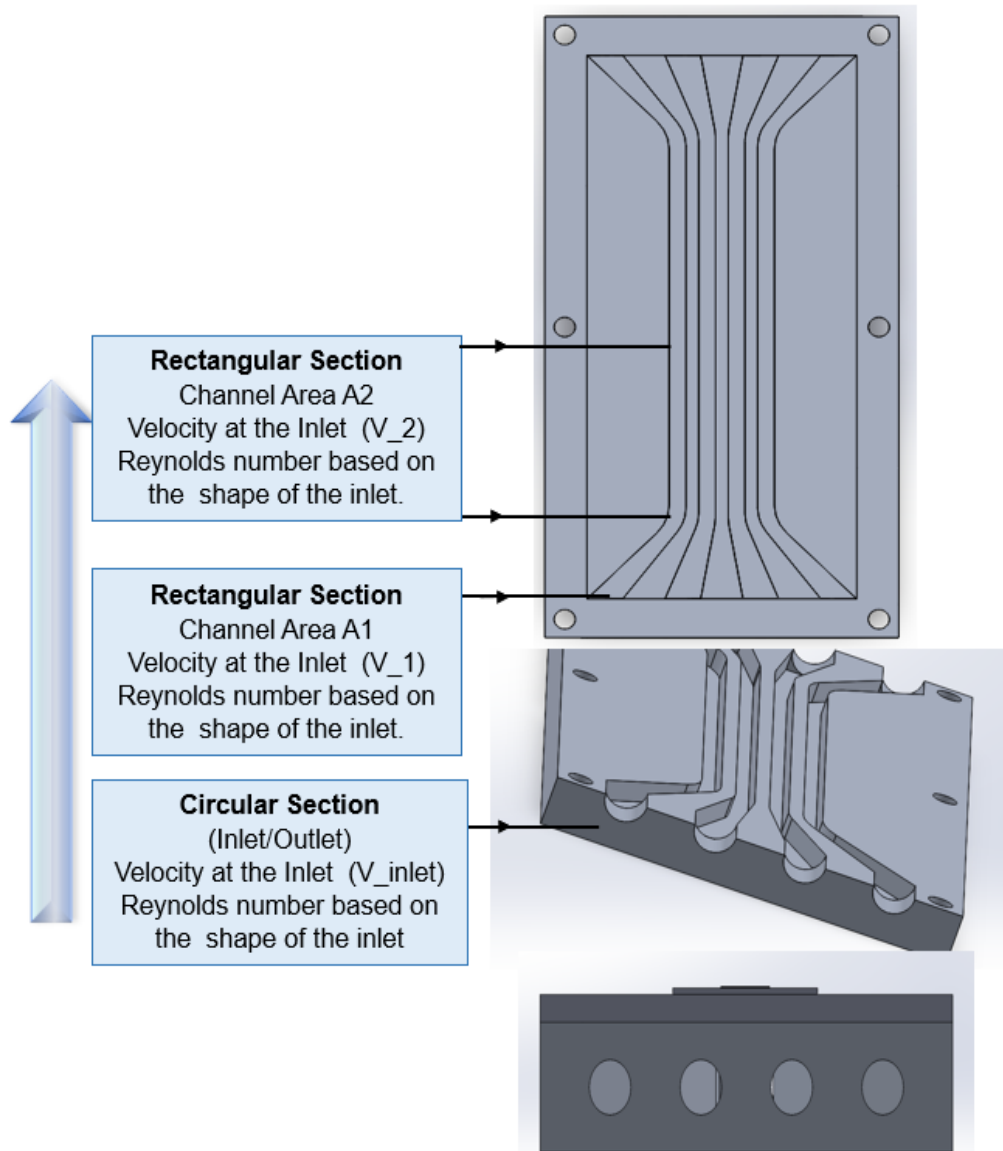


Figure 3-5 Detailed model channel view

**Table 3-1 Model specifications**

Parameter	Parameter	Design Specifications	Hydraulic Diameter (Dh)
Circular Inlet Section	Circular Inlet Diameter (m)	0.0085	0.0085
	Inlet radius (m)	0.0043	
	Cross section Area ( $m^2$ ) $\times 10^{-5}$	5.67	
Rectangular Channel Section	Inlet channel Area ( $m^2$ ) $\times 10^{-5}$	7.22	0.0054
	Actual Channel area ( $m^2$ ) $\times 10^{-5}$	3.4	
Channel length (m)		0.4	
Single Solar cell length (m)		0.01	
Single Solar cell width (m)		0.0103	
Single Solar cell Area ( $m^2$ ) $\times 10^{-4}$		1.03	
Heat flux Area ( $m^2$ ) $\times 10^{-4}$		8.22	
Model Cover thickness (m)		0.0058	
Aluminium thermal conductivity (w/m. K)		180	
Thermal Resistance (K/W)		0.039	

The hydraulic diameter ( $D_h$ ) is given by equation 3-1 below, where P is the perimeter, and A is the area.

$$D_h = \frac{4A}{P} \quad (3-2)$$

For a circular inlet, the perimeter is given by  $P = 2\pi r$ , and the area is given by  $A = (\pi r^2)$ . Where  $r$  is the radius. Therefore, equation 3-1 becomes;

$$D_h = \frac{4(\pi r^2)}{2\pi r} = 2r = d \quad (3-3)$$

For a rectangular inlet, the perimeter is given by  $P = 2(a + b)$ , and the area is given by  $A = (ab)$ , where  $a$  and  $b$  are the length and width, respectively. Therefore, equation 3-1 becomes;

$$D_h = \frac{4(ab)}{2(a+b)} = \frac{2ab}{a+b} \quad (3-4)$$

While for a square inlet, the perimeter is given by  $P = 4a$ , and the area is given by  $A = (a^2)$  Where  $a$  is the side. Therefore, equation 3-1 becomes;

$$D_h = \frac{4(a^2)}{4a} = a \quad (3-5)$$

The model thermal resistance was calculated using equation 3-6, where  $t$  is the thickness of the model cover, and  $k$  is the thermal conductivity of the material, which in this research is 180w/m. K for Aluminium 6082T6, and  $A$  is the area of the heat source, which in this research is the solar cell.

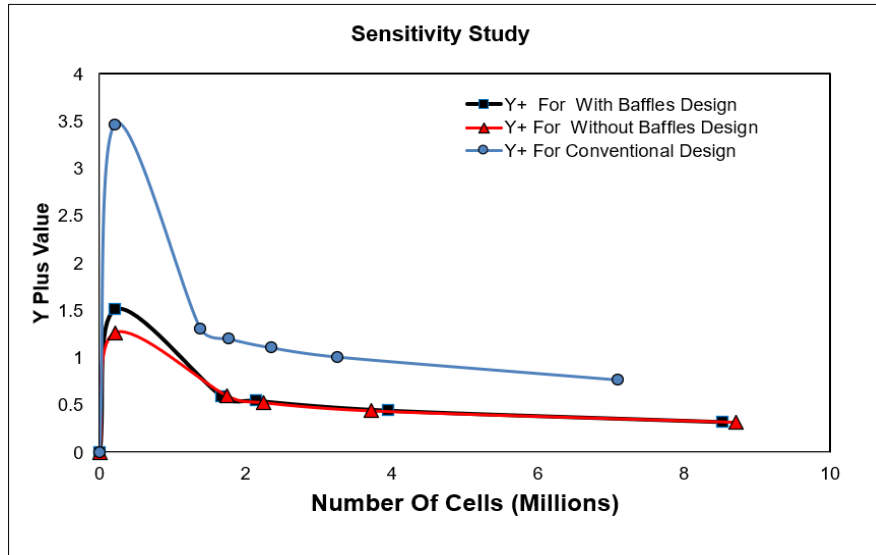
$$R_{model} = \frac{t}{kA} \quad (3-6)$$

## 3.2 Simulation

The 3D model was created with SOLIDWORKS. Computational fluid dynamics (CFD) codes are used to solve the Navier-Stokes equations for mass, momentum, and energy. Ansys meshing and FLUENT 2021R1 software were used for the analysis. The model was validated experimentally using the conventional continuous flow of CPV cooling, and a user-defined function (UDF) was used to generate the pulsation for the simulation. Germanium material was used as the solar cell, while aluminium was used as the cooling pad material in the fluent. The Reynolds averaged Navier Stokes (RANS) problem was solved numerically by dividing it into many equations and solving the dominant equation. Lamina model corresponding to 1482.41 Reynolds number (Re) at 0.5L/m was used, and the  $k-\epsilon$  model with enhanced wall function corresponding to 1-2.5L/m with Re increase from 1482.41 to 8372.26 was used for the simulation as adapted in [162–166]. A residual of  $10^{-6}$  coupled with the SIMPLE method, was considered a converged solution. A total of  $150000W/m^2$  heat flux was used in the simulation, equivalent to 150suns concentration of the sun's simulator used



for the experiment. A mesh sensitivity analysis was conducted by increasing the number of cells until the  $y^+$  value was less than one (Figure 3-6). The mesh with a  $y^+$  value less than 1 was considered a fine mesh for all three model designs and therefore was used for the simulation analysis.



**Figure 3-6 Model mesh sensitivity analysis**

### 3.2.1 Simulation Assumption

The numerical simulation analysis was conducted based on the following assumptions:

1. Flow is single phase, incompressible, and flow with Reynolds number ( $Re$ )  $\leq 2100$  was associated as laminar; above was considered turbulent flow.
2. Fluid coolant thermo-physical properties are considered constant.
3. No radiation heat transfer.

### 3.2.2 Generating Simulation Pulsating Flow

A Simulation was conducted with the continuous and pulsating flow. A frequency of 0.5Hz and a period of 2s were used to generate the pulsation. In other to generate pulsating flow at the inlet, a user-defined function (UDF) was created for a 0.5l/m (0.0085kg/s) to 2.5l/m (0.0425kg/s) flow rate. The equivalent velocity was used in the UDF, which was imported to FLUENT software. Then boundary conditions at the walls, inlet, and outlet were defined. Table 3-2 shows each

flowrate considered, and velocity calculated using equation 3-1 and design specification in table 3-1. Figures 3-7 and 3-8 show the conventional and parallel designs file, respectively.

**Table 3-2 Flow rates and velocity calculations for UDF**

Flow Rate (L/min)	Flow Rate ( $m^3/s$ ) ( $\times 10^{-5}$ )	Flow Rate (kg/s) ( $\times 10^{-2}$ )	Velocity (m/s)	
			Conventional Design	Parallel Design
2.5	4.17	4.25	0.734	0.184
2	3.33	3.40	0.587	0.147
1.5	2.50	2.55	0.441	0.110
1	1.67	1.70	0.294	0.0734
0.5	0.833	0.85	0.147	0.0367

**Table 3-3 Simulation settings and initial conditions**

Parameter	Value/Properties	
Fluid	Type	Water
	Density ( $kg/m^3$ )	998.2
	Viscosity ( $kg/m^3$ )	0.001
	Energy	ON
	Gravity $m/s^2$	-9.8 along Y-axis
	Specific heat Cp (j/kgK)	4182
	Thermal conductivity (w/mK)	0.6
Boundary conditions	Inlet	Velocity inlet
	Outlet	Pressure outlet
	Walls	Aluminium
	Solar cell material	Germanium
	Cooling pad material	Aluminium
Time	Timestep size,	0.1
	Number of time steps,	100
	Maximum iteration/time step	5
Initialization	Type	Standard
	Reference Temperature (K)	298
Turbulence model	Pressure-based, transient, k-epsilon, realizable enhance wall treatment	

Pulseflow\_Parallel\_design\_4inlet\_0.0085kg\_s - Notepad

File	Edit	Format	View	Help
Pulseflow		5	5	1
time	vel1	vel2	vel3	vel4
0	0.03671	0.03671	0.03671	0.03671
1	0.03671	0.03671	0.03671	0.03671
1	0	0	0	0
2	0	0	0	0
2	0.03671	0.03671	0.03671	0.03671

Ln 8, Col 1 | 100% | Windows (CRLF)

Pulseflow\_Parallel\_design\_4inlet\_0.017kg\_s - Notepad

File	Edit	Format	View	Help
Pulseflow		5	5	1
time	vel1	vel2	vel3	vel4
0	0.07342	0.07342	0.07342	0.07342
1	0.07342	0.07342	0.07342	0.07342
1	0	0	0	0
2	0	0	0	0
2	0.07342	0.07342	0.07342	0.07342

Ln 8, Col 1 | 100% | Windows (CRLF)

Pulseflow\_Parallel\_design\_4inlet\_0.0255kg\_s - Notepad

File	Edit	Format	View	Help
Pulseflow		5	5	1
time	vel1	vel2	vel3	vel4
0	0.11013	0.11013	0.11013	0.11013
1	0.11013	0.11013	0.11013	0.11013
1	0	0	0	0
2	0	0	0	0
2	0.11013	0.11013	0.11013	0.11013

Ln 8, Col 1 | 100% | Windows (CRLF)

Pulseflow\_Parallel\_Design\_4inlet\_0.034kg\_s - Notepad

File	Edit	Format	View	Help
Pulseflow		5	5	1
time	vel1	vel2	vel3	vel4
0	0.14684	0.14684	0.14684	0.14684
1	0.14684	0.14684	0.14684	0.14684
1	0	0	0	0
2	0	0	0	0
2	0.14684	0.14684	0.14684	0.14684

Ln 8, Col 1 | 100% | Windows (CRLF)

Pulseflow\_Parallel\_design\_4inlet\_0.0425kg\_s - Notepad

File	Edit	Format	View	Help
time	vel1	vel2	vel3	vel4
0	0.18355	0.18355	0.18355	0.18355
1	0.18355	0.18355	0.18355	0.18355
1	0	0	0	0
2	0	0	0	0
2	0.18355	0.18355	0.18355	0.18355

Ln 8, Col 1 | 100% | Windows (CRLF)

**Figure 3-7 Generating pulsating flow parallel design UDF (both without and with baffles) for 0.5l/m to 2.5l/m**

Pulseflow\_Conventional\_design\_1inlet\_0.5L\_m-2.5L\_m - Notepad

File	Edit	Format	View	Help	
Pulseflow		6	5	1	
time	vel1	vel2	vel3	vel4	vel5
0	0.14684	0.29367	0.44051	0.58735	0.73418
1	0.14684	0.29367	0.44051	0.58735	0.73418
1	0	0	0	0	0
2	0	0	0	0	0
2	0.14684	0.29367	0.44051	0.58735	0.73418

Ln 8, Col 1 | 100% | Windows (CRLF)

Figure 3-8 Generating pulsating flow conventional design UDF for 0.5l/m to 2.5l/m

### 3.3 Experiment

An experiment using a high-flux sun simulator was conducted with both continuous and pulsating flow. Figure 3-9 and Figure 3-10. shows the experimental process flow of the piping and Instrumentation diagram adopted for both conventional and parallel design. The complete 3D model and channels were built using three-axis Computer Numerical Control (CNC) machine with Aluminium 6082T6 flat plate material. The pulsating flow was generated using a coding programme with an Arduino microcontroller integrated with solenoid valves. A 5-multijunction solar cell was coupled to the built model (referred to as a cooling pad in this research). The solar cell more information is available in Appendix A.

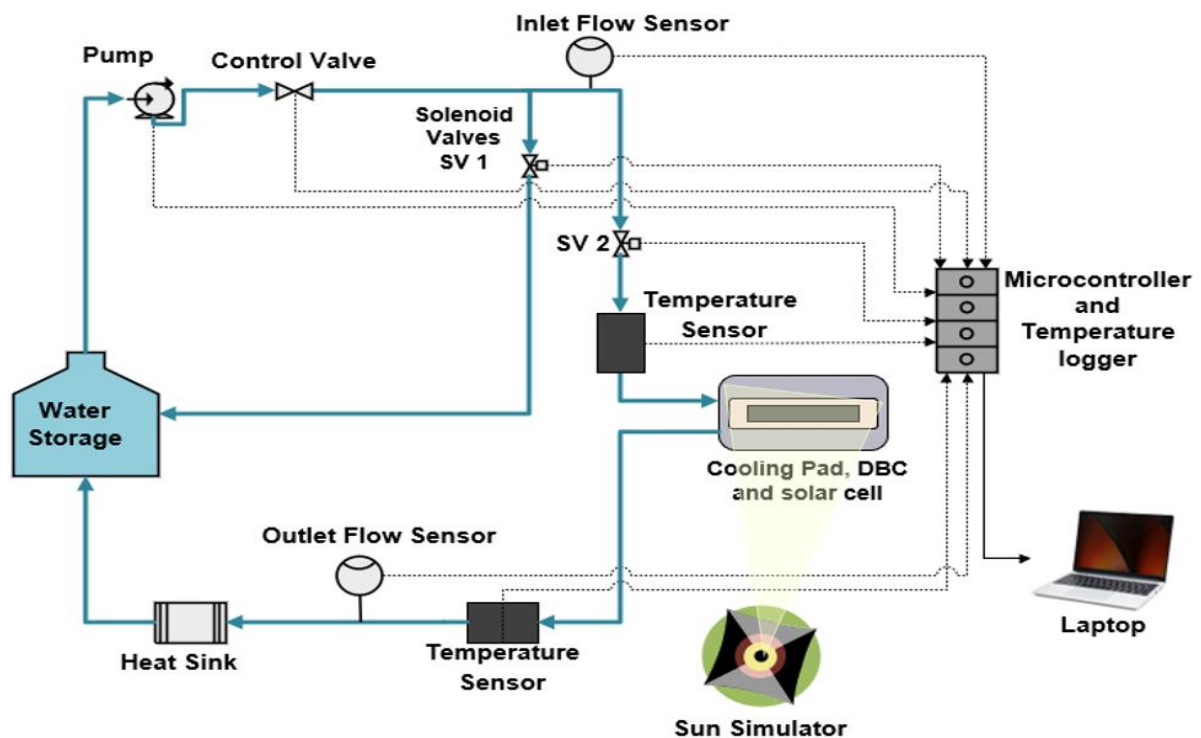
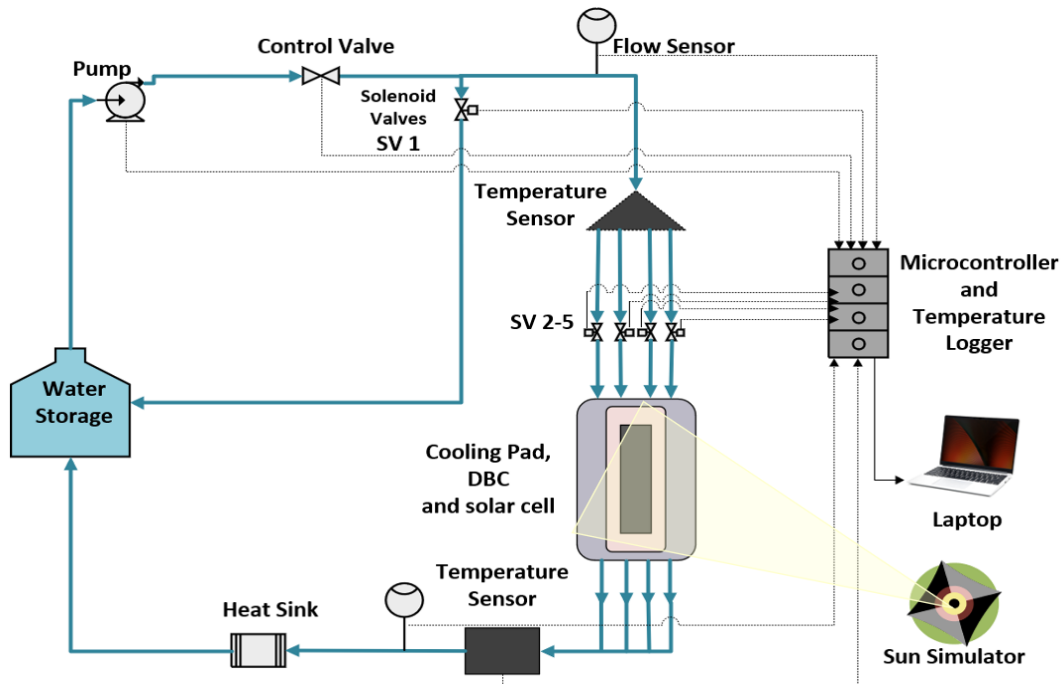
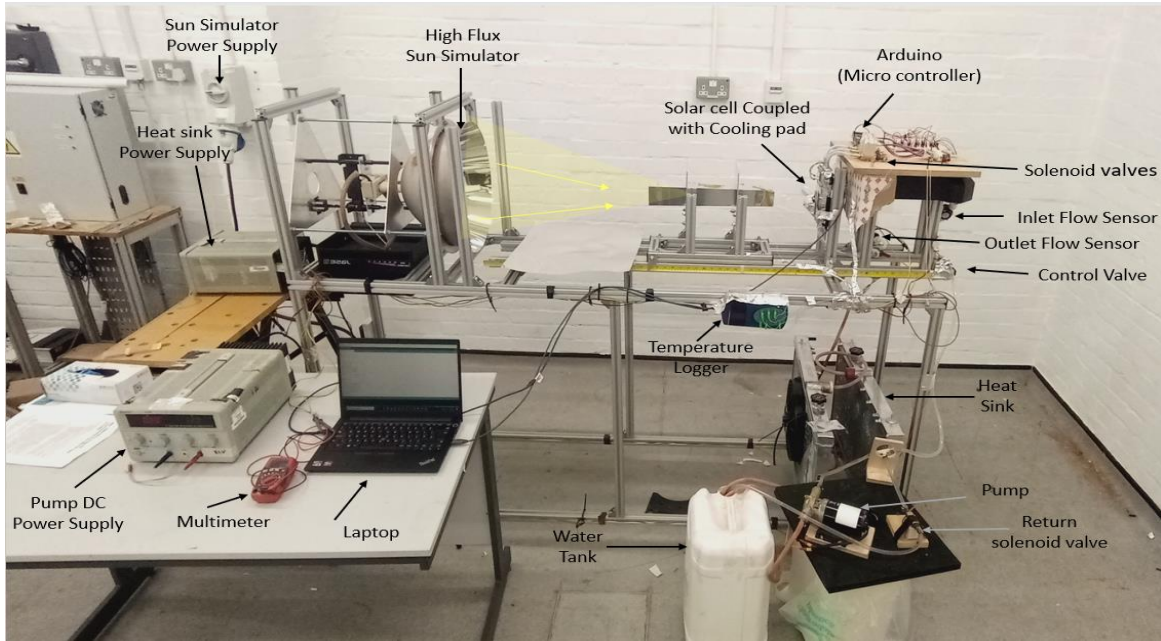


Figure 3-9 Experimental process flow diagram for conventional design



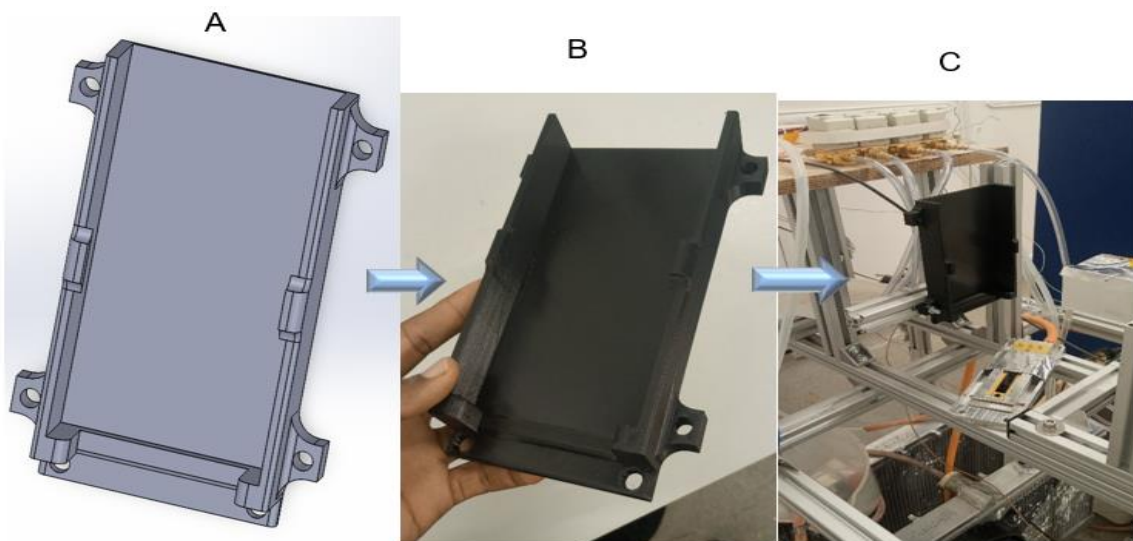
**Figure 3-10 Experimental process flow diagram for the parallel design**

Figure 3-11 Shows the actual experimental setup built using a high flux concentrated sun simulator with complete piping and Instrumentation. The sun simulator was ON for 10 minutes based on the recommendation highlighted in the sun simulator user manual, after which the shutter was opened to concentrate the light unto the cell. The cooling starts to run for 5 minutes to stabilise the cell's concentration. The experiment data was run for 25 minutes and an interval of 5 minutes on a single flow rate. The flow rate is from 0.5L/m to 2.5L/m, the same as the simulation. Data are recorded after every minute, and the average after 5 minutes was used. An adequate heat sink would affect the coolant (water) inlet temperature working in circulation. The maximum cooling capacity theoretically required by the solar cell was 823W. Two large radiators connected in series integrated with a fan were used as the heat sink (Figure 3-11).



**Figure 3-11 Experimental set up**

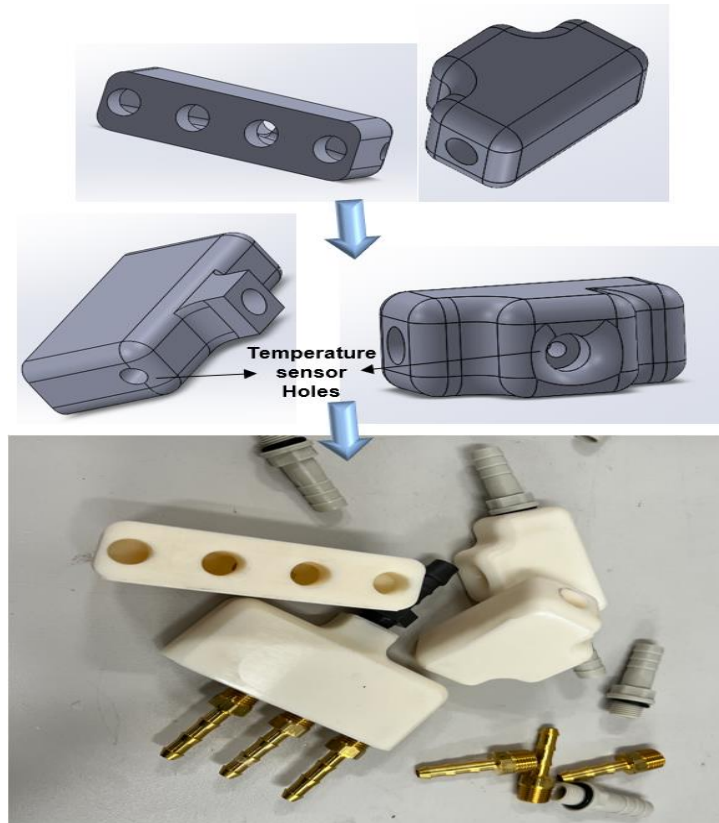
A holder to fix the sun simulator's cooling design was designed and 3D printed using an Anycubic Vyper 3D Printer with PLA filament (Figure 3-12). The printer has an operational nozzle temperature of  $\leq 260^{\circ}\text{C}$  and an operational hot bed temperature of up to  $\leq 110^{\circ}\text{C}$ , making it suitable. Ultimaker Cura version 5.1.0 was used as slicing software to generate the G-Code. Figure 3-12A shows the computer-aided design, Figure 3-12B shows the printed design, and Figure 3-12C shows the mounted holder on the sun simulator.



**Figure 3-12 Cooling pad design holder**



A temperature sensor holder suitable with the cooling pad design was designed and printed for both conventional and parallel design Figure 3-13. Anycubic Photon Mono X 3D printer was used with white resin. The Anycubic UV 3d resin has good hardness and toughness, making it suitable. Moving from top to bottom of Figure 3-13 top shows the computer-aided design, and the bottom shows the actual printed design.

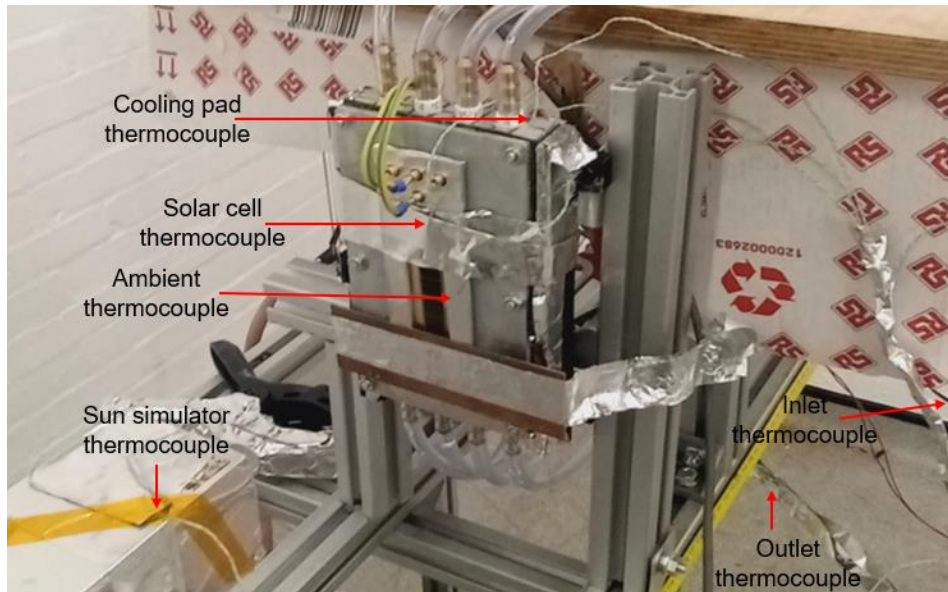


**Figure 3-13 Temperature sensor holder**

### **3.3.1 Generating Experiment Pulsating Flow**

The pulsating flow was generated during the experiment using an Arduino microcontroller integrated with solenoid valves SV1 and SV2 in Figure 3-9 and SV1 and SV2-5 in Figure 3-10. The solenoid valve was operated with a frequency of 0.5Hz and a period of 2s (the same as the simulation). A 5-multijunction solar cell was coupled to the built model. The location of thermocouples used in the experimental set-up are shown with red arrow in Figure 3-14, which include Inlet, outlet, cooling pad, solar cell ambient, and sun simulator. A 25-litre water tank

was used as coolant. Thermal paste with thermal conductivity of 8.5 W/mK was used between the back of the solar cell and the cooling pad design to make good contact. A complete technical specification of the components used in the experiment is available in Appendix B.

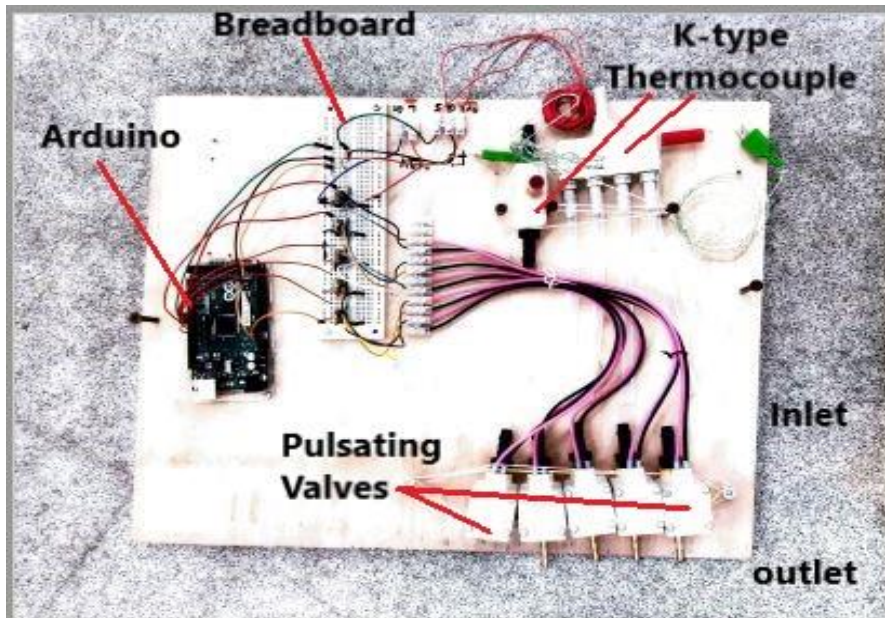


**Figure 3-14 Location of thermocouples on experimental set-up**

The solenoid valve was used to generate the pulsating flow. Two were used in the conventional design, while five were used for the parallel design. The control valve used with model number 390-7667 was produced by RS PRO. The Pico TC-08 thermocouple temperature data logger can measure temperatures from -270°C to +1820°C, making it suitable for this research. The metal-oxide-semiconductor field-effect transistors and resistors were used in constructing the electrical circuit that controls the solenoid valves. Which serves as a switch that opens and closes the solenoid valves to generate pulsation. Arduino Mega 2560 R3 was chosen for the experiment because of its features. It is a microcontroller suitable for controlling solenoid valves and collecting data from the flow sensor. A 8mm barbed brass and nylon 1/8 male thread fitting manufactured by Legris was used in the cooling pad design. Both 4 mm and 8 mm inner diameter piping tube was used to connect the solenoid valve and pump, water flow sensor, and temperature sensor, respectively. A 25-litre water tank used as the cooling fluid. A thermal paste with thermal conductivity of 8.5 W/m K used between the back



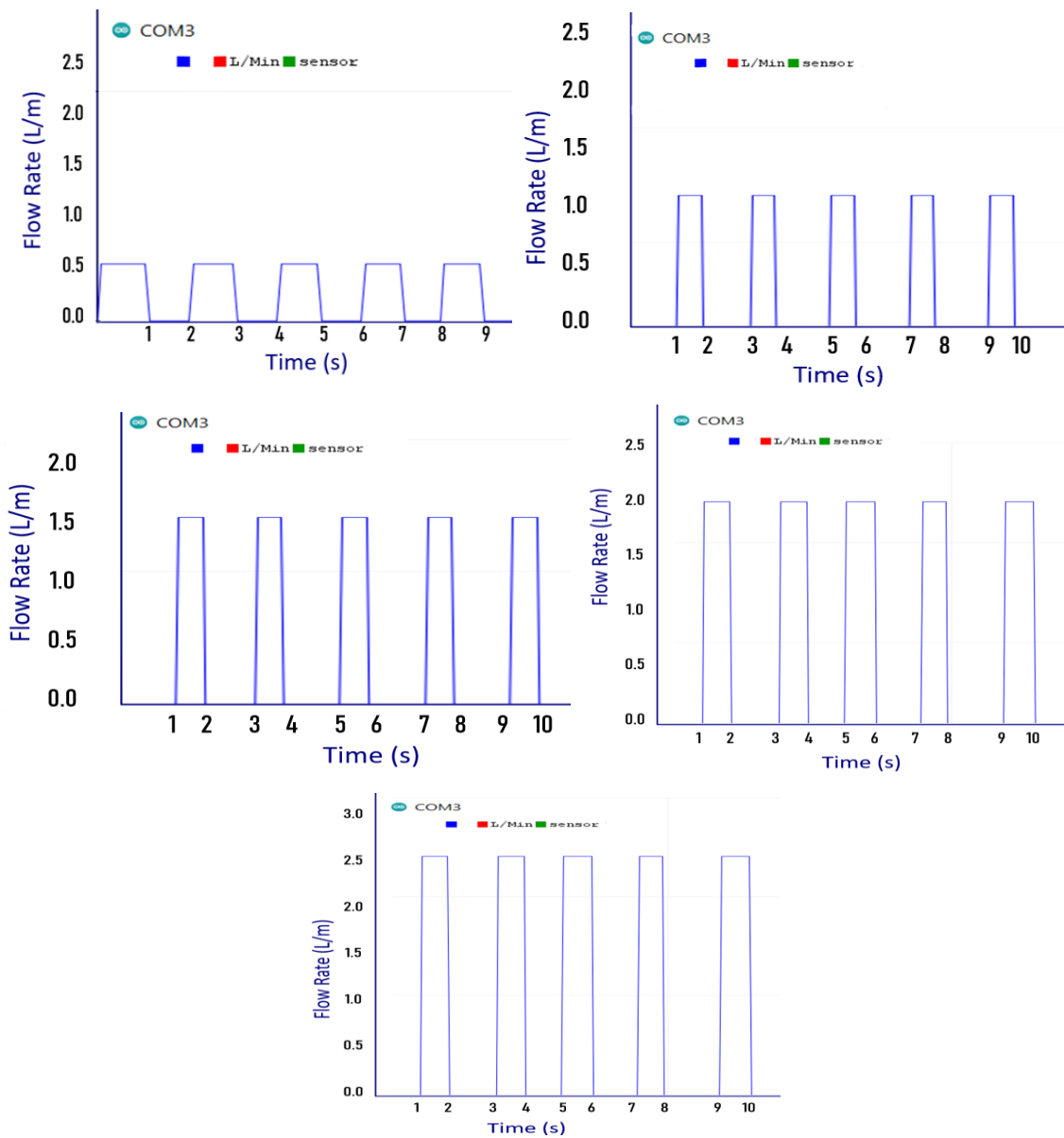
of the solar cell and the cooling pad design to make good contact. A female thread 8mm barber 1/2 manufactured by Sourcing Map was used as the flow sensor fitting. A 0.5-30L/m water flow sensor was used to measure the flow rate at the inlet and outlet. It's a Lieve brand with model number FS200A, 1.2Mpa and G1/2 thread available with grandado UK. A Type-K thermocouples temperature sensor with a 1.5mm diameter and -75 to +250 °C temperature range was used. A hose clip was used to tighten the tube piping connections. Two large radiators integrated with a fan was used as the heatsink. A complete technical specification of all the components are available in Appendix B. Figure 3-15 shows the wiring circuit of the Arduino with MOSFET, resistor and diode on the breadboard where control is established, and data was collected.



**Figure 3-15 Wiring connection set up**

Figure 3-16 shows the pulsating flow signal generated for the experiment using a programme developed by an Arduino microcontroller. A rectangular profile signal was recorded. A MOSFET was used as an ON/OFF switch to switch the solenoid valve ON (for 1 second) uniformly and OFF (for 1 second) uniformly to generate a uniform pulsating flow in the channel. The uniform pulsating flow splits the total flow ON/OFF into four at a time in the case of Parallel design because it has four inlets/outlets. At the same time, the total flow was ON/OFF for

conventional design without any splitting because of a single inlet/outlet. The code is available in Appendix C.



**Figure 3-16 Uniform pulsating flow signal for flow rate 0.5l/m to 2.5l/m, with a frequency of 0.5Hz, and period of 2s**

Figure 3-17 shows the bio-inspired pulsating flow signal generated for the experiment using a programme developed by an Arduino microcontroller. In this approach, two solenoid valves (V) are switched ON (for 1 second) uniformly and OFF (for 1 second) uniformly to generate a Bioinspired pulsating flow. A MOSFET was used as an ON/OFF switch; therefore, a rectangular profile signal was

recorded. It is bioinspired because, unlike uniform pulsating flow, the total flow was split into two (two valves open at a time) and passed through two channels simultaneously. The code is available in Appendix C.

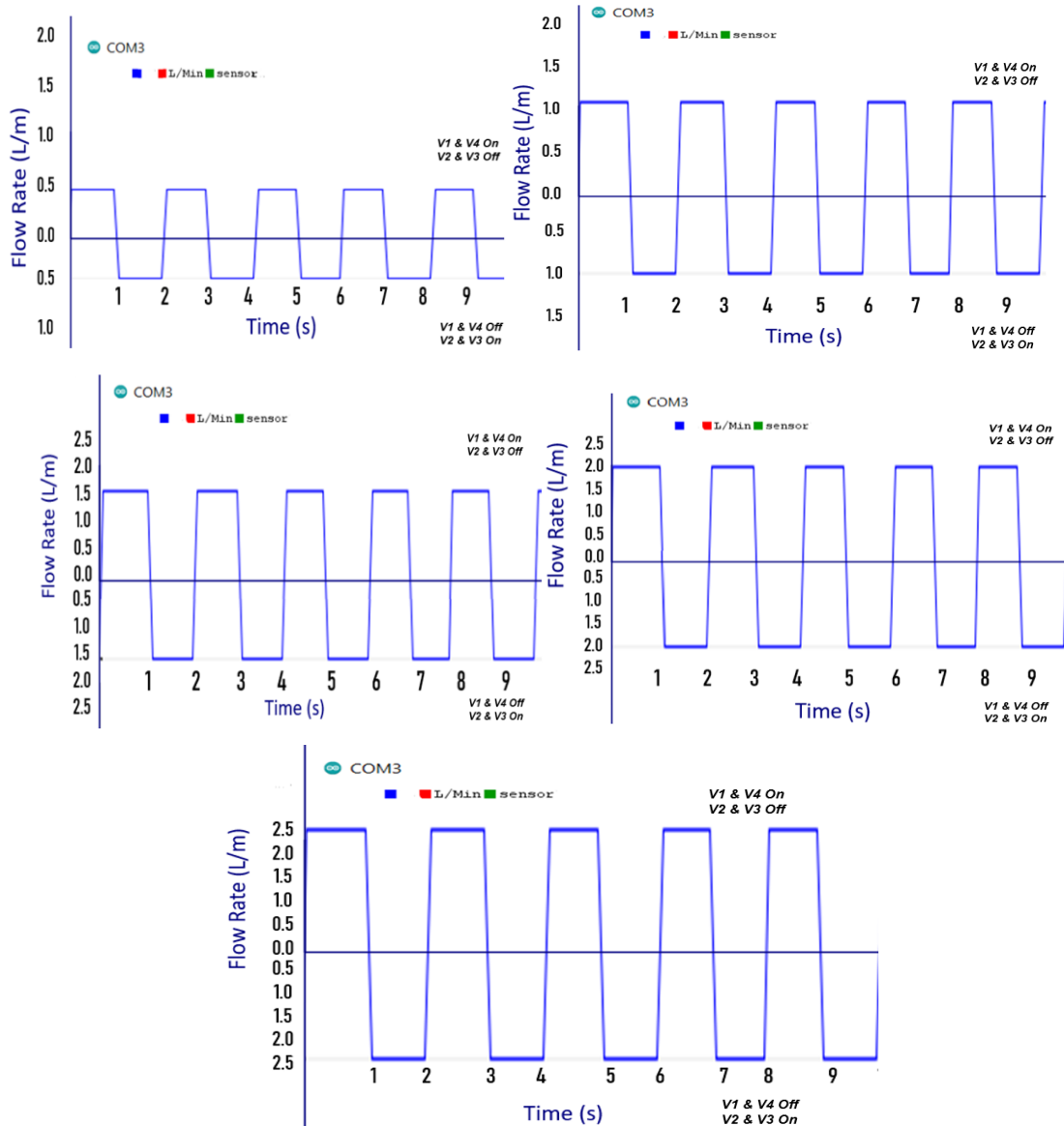


Figure 3-17 Bio-inspired pulsating flow signal for flow rate 1.0L/m, frequency of 0.5Hz, and period of 2s

### 3.4 Correlations In Continuous and Pulsating Flow

The correlations for both continuous [120,167–169] and pulsating flow [61,137,170–173] are as follows.

In continuous flow, the Reynolds number ( $Re$ ) is a parameter that differentiates between turbulent flow and laminar flow. For a continuous flow, it's given by equation 3-7 where  $D_h$  is the hydraulic diameter,  $\rho$  is the density,  $\mu$  is the dynamic viscosity,  $v$  is the velocity,  $\nu$  represents kinematic viscosity.

$$Re = \frac{\rho v D_h}{\mu} = \frac{v D_h}{\nu} \quad (3-7)$$

Nusselt number ( $Nu$ ) is the ratio of the amount of heat transferred by convection and the hydraulic diameter to the thermal conductivity of the coolant, in this case, water.  $h$  is the heat transfer coefficient,  $k$  is the thermal conductivity.

$$Nu = \frac{h D_h}{k} \quad (3-8)$$

The heat transfer coefficient was calculated using equation 3-9 according to [167,174], where  $m$  is the mass flow rate,  $c_p$  is the specific heat capacity,  $T_{out}$  and  $T_{in}$  is the fluid inlet and outlet temperature,  $T_s$  and  $T_f$  Are the cooling pad temperature and average fluid temperature, respectively.

$$h = \frac{m c_p (T_{out} - T_{in})}{A (T_s - T_f)} \quad (3-9)$$

Pressure Drops as a function of friction factor were calculated using equation 3-10, where for a smooth rectangular channel, the friction function  $f = 68.34/Re$  for lamina flow, and  $f = 0.31/Re^{0.25}$  for turbulent flow, according to [169].

$$\Delta P = f \times \frac{l}{D_h} \times \frac{v^2}{2} \times \rho \quad (3-10)$$

In pulsating flow, the pulsating velocity (instantaneous velocity) is given by  $u_p = v(1 + \sin\omega t)$ ,  $\omega = 2\pi f$  refers to the angular velocity of the pulsation, and  $v$  is the average velocity [170]. Were  $f = 1/T$  is the frequency of pulsation and  $T = T_1 + T_2$  is the period where  $T_1$  and  $T_2$  are the first and second half periods of pulsating

[175]. Equations 3-11 and 3-12 are given the pulsating velocity for a rectangular and triangular profile.

$$u_p = \frac{\sin [-K \sin \omega t]}{\text{Sin}^{-1}(-K)} \quad (3-11)$$

$$u_p = \frac{\tanh [K \sin \omega t]}{\tanh K} \quad (3-12)$$

The Reynolds number in pulsating flow is associated with the oscillating Reynolds number ( $Re_\omega$ ), and stable components Reynolds number ( $Re_s$ ) given by equations 3-13 and 4-14, respectively [171]. The dimensionless amplitude of pulsation is given by  $A_o = UD_h/\nu$  [176].

$$Re_\omega = \frac{A_o^2}{\nu \omega} \quad (3-13)$$

$$Re_s = \frac{u_p D_h}{\nu} \quad (3-14)$$

In pulsating flow, the Nusselt number is considered a time average Nusselt number used to determine the heat transmission properties. Equation 3-15 and Equation 3-16 gives the expression according to [171] and [140], respectively.  $\bar{h}$  is the time average heat transfer.

$$\overline{Nu} = \int_0^L \int_0^T Nu(x, t) dt dx \quad (3-15)$$

$$\overline{Nu} = \frac{\bar{h} D_h}{k_f} \quad (3-16)$$

The average heat transfer coefficient is given by equation 3-17 as a function of the log mean temperature where  $Q = mc_p(T_{out} - T_{in})$ , and  $A_s$  It is the heat transfer area.

$$\bar{h} = \frac{Q}{A(T_s - T_f)} \quad (3-17)$$

In the context of an oscillating flow, the Womersley number is an expression of the influence of frequency on which force, inertia, or viscosity will dominate. It's given by equation 3-18 according to [171].

$$\alpha = (2\pi ReSt)^{1/2} \quad (3-18)$$

$$\alpha = L \left( \frac{\omega}{\nu} \right)^{1/2} \quad (3-19)$$

The Strouhal number is another dimensionless number used in a pulsating flow, according to [171]. It expresses the frequency divided by the velocity as equation 3-20.

$$St = \frac{fL}{u} \quad (3-20)$$

The pressure drops can be expressed as equation 3-21 for  $\alpha < 1$  or equation 3-22.

$$\Delta P = \frac{8\mu L Q}{\pi R^4} \quad (3-21)$$

$$\Delta P = f\rho \left( \frac{l}{D_h} \right) \left( \frac{v^2}{2} \right) \quad (3-22)$$

The following correlations are used for calculating thermodynamic properties adapted in this research as a function of fluid temperature T (K) reported by [122,177–179].

$$\text{Density } \rho(T) = 8338.46 + 1.40T - 3.01 \times 10^{-3}T^2 + 3.01 \times 10^{-3}T^2 \quad (3-23)$$

$$\text{Specific Heat } Cp(T) = 12010.14 - 80.40T + 30.98 \times 10^{-2}T^2 - 5.38 \times 10^{-4}T^3 + 3.62 \times 10^{-7}T^4 \quad (3-24)$$

$$\text{Thermal conductivity } K(T) = -86.90 \times 10^{-2} + 8.94 \times 10^{-2}T - 1.58 \times 10^{-5}T^2 + 7.97 \times 10^{-9}T^3 \quad (3-25)$$

$$\text{Dynamic viscosity } \mu (T) = 1.37 - 21.22 \times 10^{-3}T + 1.36 \times 10^{-4}T^2 - 4.64 \times 10^{-7}T^3 + 8.90 \times 10^{-10}T^4 - 89.07 \times 10^{-13}T^5 + 3.84 \times 10^{-16}T^6 \quad (3-26)$$

The thermal resistance of the model designs was calculated as a function of the thickness ( $t$ ) of the model cover, thermal conductivity ( $K$ ) of the material (aluminium), and total heat flux ( $q$ ) from surface contact using equation 3-27.

$$R_{thermal\ Resistance} = \frac{t}{Kq} \quad (3-27)$$

The heat transfer enhancement ( $E$ ) can be obtained by equations 3-28, where  $N_p$  is the pulsating average Nusselt number and  $N_{np}$  is the non-pulsating Nusselt number [170].

$$E = \frac{N_p}{N_{np}} \quad (3-28)$$

## 4 CHAPTER FOUR

### 4.1 Simulation Results

#### 4.1.1 Effect of Coolant Inlet Temperature

Sunlight on a solar cell change continually. The continuous fluctuation of solar radiation intensity due to uncontrollable conditions, such as clouds, is inevitable. This leads to fluctuations in the ambient and coolant temperatures at the inlet of a cooling system. Therefore, we study the effect of the coolant (working fluid) inlet temperature on cooling using continuous flow. Figure 4-1 shows the effect of the coolant inlet temperature on the model design. With an increase in the inlet temperature of the coolant from 298K to 318K, the solar cell and cooling pad temperatures increased from 301.93K to 321.91K and 305.88K to 325.87K, respectively. This shows that the coolant temperature directly affects the system's cooling performance. Hence, a well-suited heat sink must be used during the experiment. Furthermore, it was observed that the temperature of the solar cell and cooling pad was lower in the parallel channel model design with and without baffles (WB-Design and WoutB-Design) compared to the conventional design model (C-Design). To visualize the impact, temperature contours of the solar cell and cooling block channel were plotted at 1L/m (Figure 4-3 and Figure 4-4).

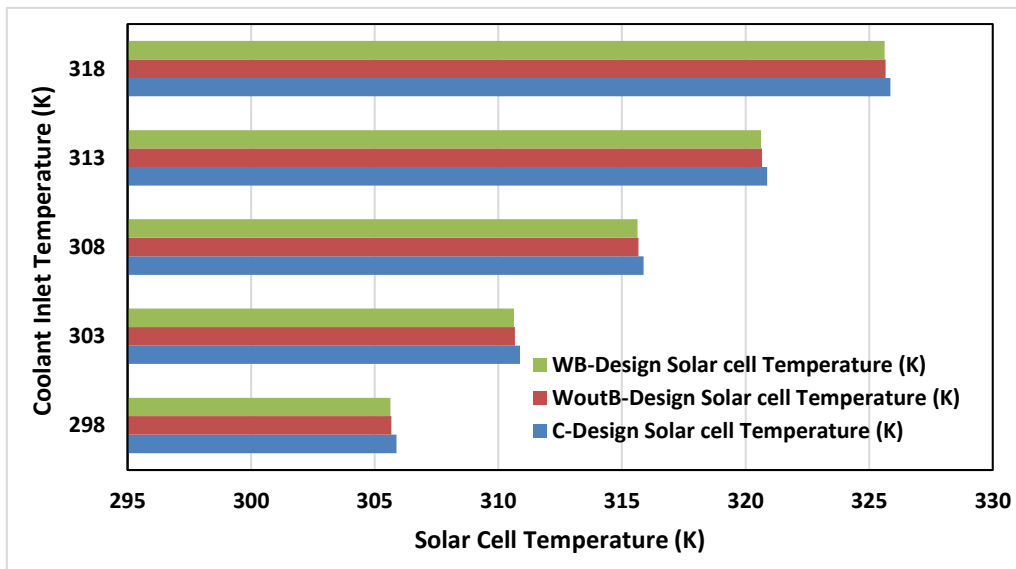
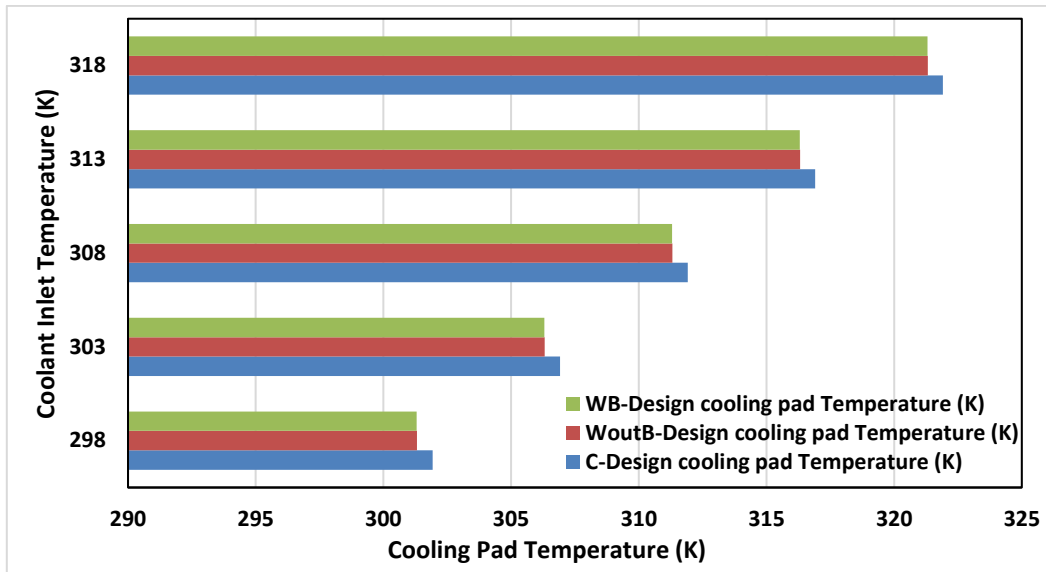


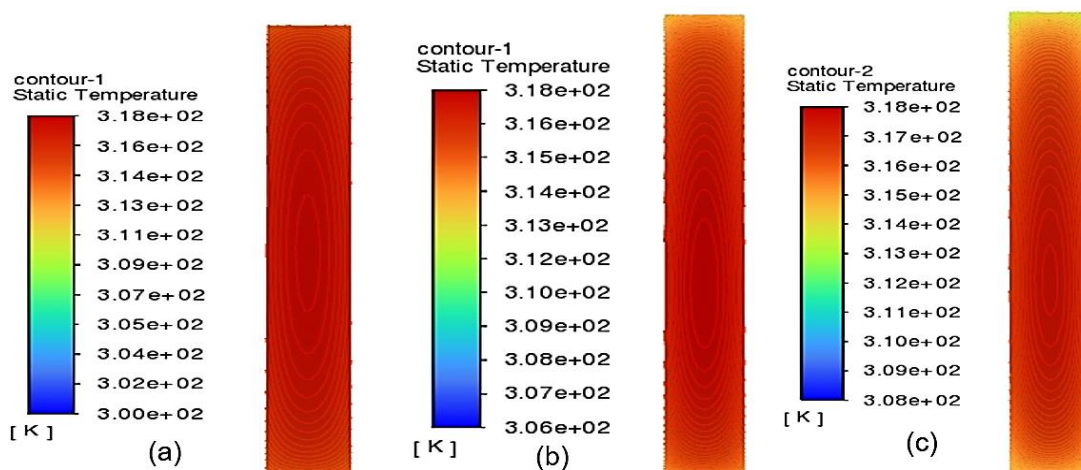
Figure 4-1 Effect of coolant inlet temperature on solar cell temperature



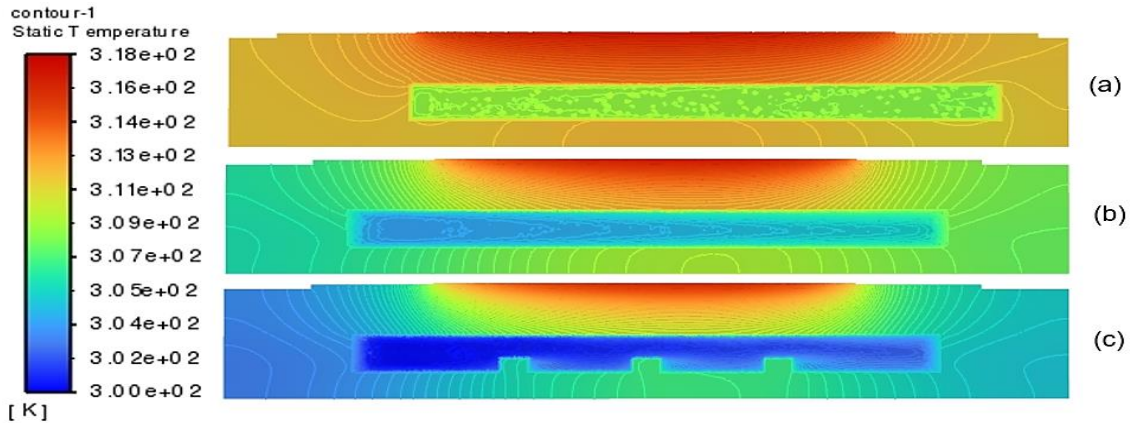


**Figure 4-2 Effect of coolant inlet temperature on cooling pad temperature**

The temperature contours of the solar cell and channel view at a flow rate of 1L/m, a flux of 150,000W/m<sup>2</sup> (150 suns), and a water inlet temperature of 305K were shown in Figures 4-3 and 4-4, respectively. The parallel design exhibits lower temperatures with equal maximum and minimum temperature intervals. The cooling block demonstrates lower temperatures compared to the solar cell due to the cooling water's initial contact with the block. Consequently, the temperature of the solar cell relies on the effectiveness of the cooling block's cooling, aligning with Newton's law of cooling.



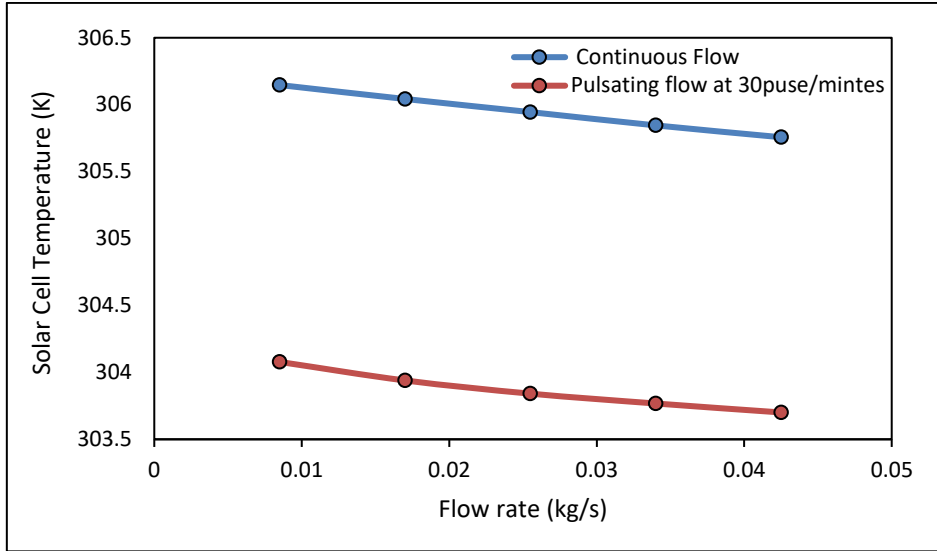
**Figure 4-3 Effect of coolant inlet temperature on solar cell temperature contours at 1L/m, 150suns concentration and 305K water inlet temperature (a) Conventional design, (b) Parallel design without baffles, (c) Parallel design with baffles**



**Figure 4-4 Effect of coolant Inlet temperature on cooling block temperature contours at 1L/m, 150suns concentration, and 305K water inlet temperature (a) Conventional design, (b) Parallel design without baffles, (c) Parallel design with baffles**

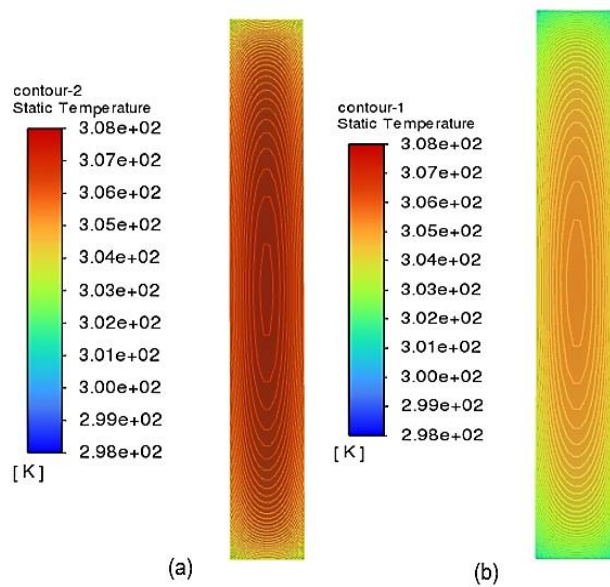
#### 4.1.2 Conventional Design (Con-Design)

Research has reported that an increase in flow rate leads to a decrease in cell temperature [120]. Similarly, in this research, the temperature of the solar cell decreases for both continuous and pulsating flow with an increase in flow rate. Figure 4-5 illustrates the solar cell temperature against flow rate for both continuous and pulsating flow. It was observed that as the flow rate increased from 0.0085kg/s to 0.0425kg/s (5L/m-2.5L/m), the solar cell temperature dropped from 304.08K to 303.70K with pulsating flow at 30 pulse/min, and from 306.15K to 305.76K with continuous flow. The solar cell temperature with pulsating flow is lower by 3.2% compared to continuous flow. The difference between the temperatures of the solar cell from an initial temperature of 298K was found to be 7.76k and 5.70K for continuous and pulsating flow, respectively. Therefore, the pulsating flow exhibits greater uniformity in cell temperature. The average cooling enhancement of pulsating flow ( $E_{puls-avg} = T_{cell-cont}/T_{cell-puls}$ ) was calculated to be 1.01, where  $T_{cell-cont}$  and  $T_{cell-puls}$  represent the average temperatures of the solar cell under continuous and pulsating flow, respectively. Additionally, a temperature contour map of the solar cell and cooling block was generated to gain a better understanding of the enhancement.



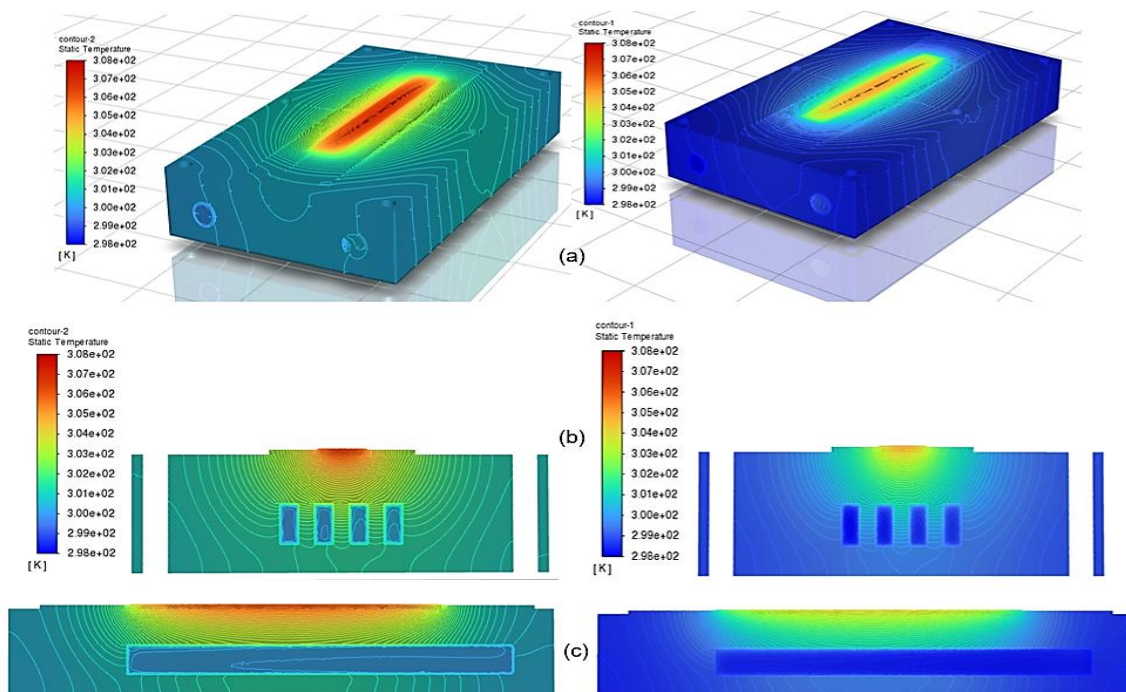
**Figure 4-5 Con-design solar cell temperature with continuous flow and pulsating flow at  $T = 2$  s,  $f = 0.5$ Hz, 30puls/minutes,  $Pr = 5.72$  and  $Pr = 5.62$ , respectively**

A temperature contour of the solar cell and cooling pad for both continuous flow and pulsating flow at a flow rate of 1L/m is depicted in Figures 4-6 and 4-7, respectively. Within an equal maximum and minimum temperature interval of 298K to 308K, the pulsating flow with a period of 2s and a frequency of 0.5Hz (Figure 4-6b) demonstrates superior cooling compared to continuous flow (Figure 4-6a).



**Figure 4-6 Solar cell temperature contours at 1L/m, 150suns concentration (a) Continuous flow, (b) Pulsating flow**

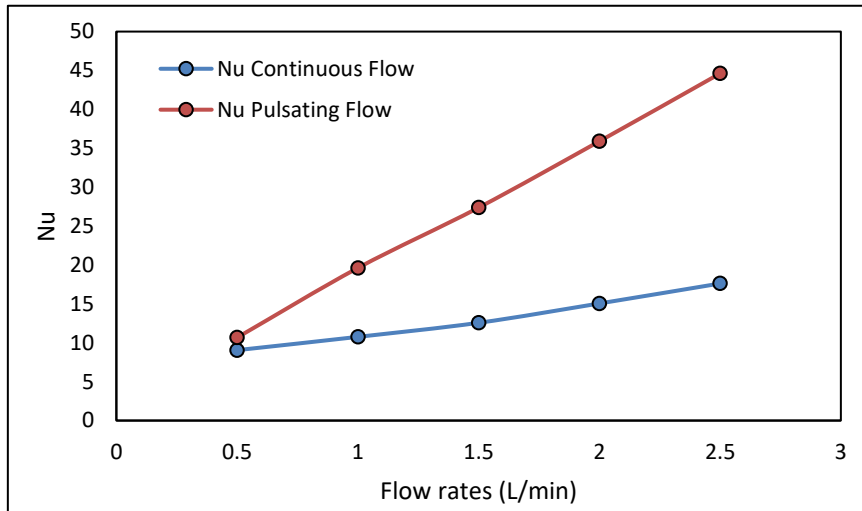
A complete 3D view of the temperature contour of the model for both continuous and pulsating flow at a flow rate of 1L/m is displayed in Figure 4-7a. Additionally, Figure 4-7b presents the 2D x-y center cut-view temperature contour of the model for continuous and pulsating flow at 1L/m. Figure 4-7c illustrates the 2D z-y center channel cut-view temperature contour of the cooling pad model for both continuous and pulsating flow at 1L/m. Within equal maximum and minimum temperature intervals of 298K to 308K, it is evident from the temperature contour that the pulsating flow with a period of 2s and a frequency of 0.5Hz, equivalent to 30 pulses per minute (Figure 4-7, right), exhibits superior cooling compared to continuous flow (Figure 4-7, left).



**Figure 4-7 Temperature contours at 1L/m, 150suns concentration conventional design (a) Complete 3D view (b) 2D x-y centre cut-view (c) 2D z-y centre channel cut-view**

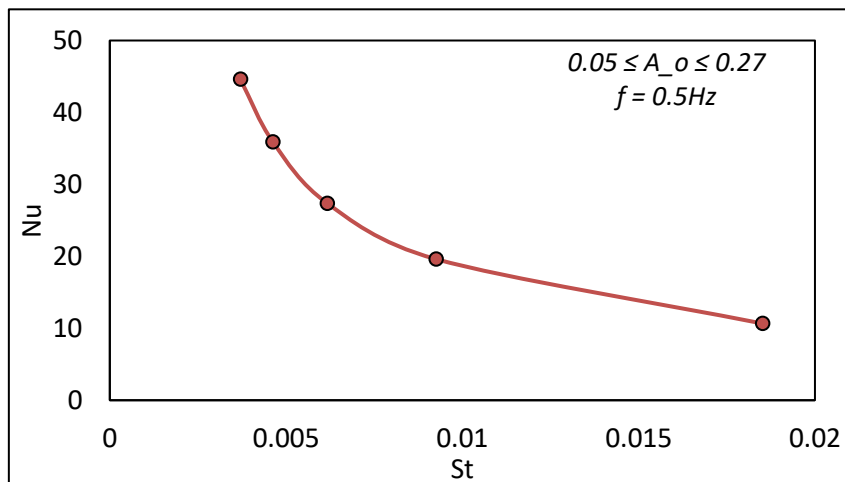
The Nusselt number is a crucial dimensionless parameter in heat transfer. Therefore, the Nusselt number was calculated using equation 3-9 for both continuous and pulsating flow using. In both flow regimes, an increase in the Nusselt number was observed. Figure 4-8 illustrates the variation of the Nusselt number with an increased flow rate from 0.5L/m to 2.5L/m for continuous steady

and pulsating flow at 30 pulses per minute. The Nusselt number ranges from 9.0 to 17.61 with continuous flow and from 10.66 to 44.62 with pulsating flow. This indicates that the pulsating flow exhibits higher convection compared to the continuous flow.



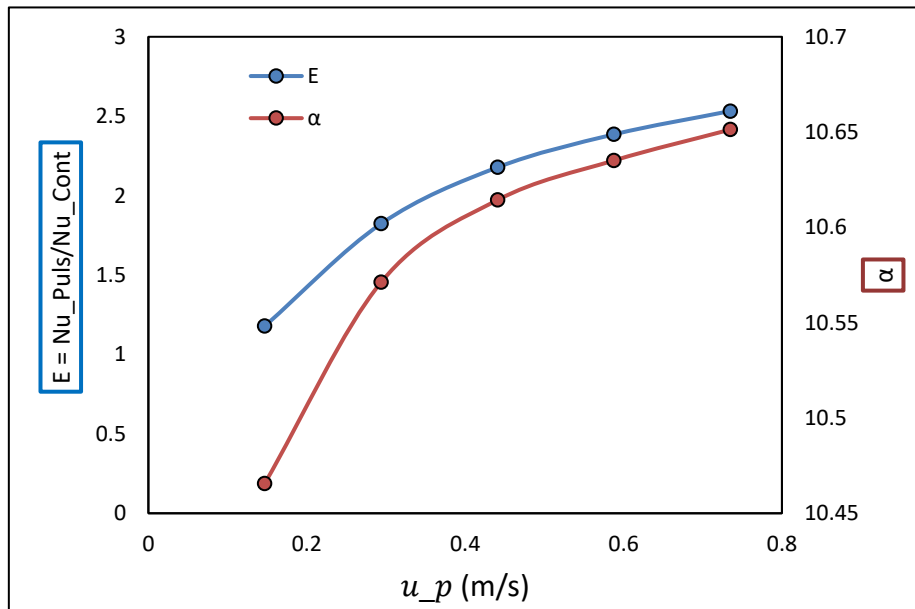
**Figure 4-8 Variation of Nusselt number with flow rate**

The Strouhal number describes the dynamics of oscillating flow in dimensionless analysis. An increase in the Strouhal number leads to a decrease in the Nusselt number at a frequency of 0.5 Hz and  $0.05 \leq A_o \leq 0.27$  pulsating amplitude. This finding aligns with the results reported in [180]. Figures 4-9 depict the variation in the Nusselt number with the Strouhal number, which was calculated using equations 3-20.



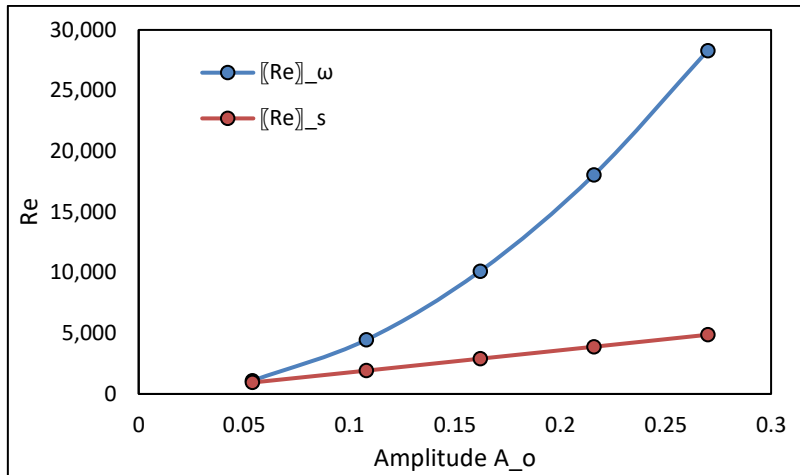
**Figure 4-9 Variation of Nusselt number against Strouhal number**

Figure 4-10 Shows the variation of heat transfer enhancement and Womersley number ( $\alpha$ ) with Instantaneous velocity ( $u_p$ ). The Womersley number indicates whether the uneven nature of fluid flow in pulsating flow is quasi-steady. With an increase in Instantaneous velocity ( $u_p$ ) from 0.14m/s to 0.73m/s, the Womersley number increase from 10.25 to 10.43. This means that the pulsating flow is associated with the plug-like flow. as such, the velocity profile is lower than the pulsating frequency. The heat transfer enhancement increased from 1.18 to 2.53. However, enhancement was observed from 0.5L/m to 2.5L/m (Figure 4-8). Maximum enhancement was recorded at 0.73m/s instantaneous velocity. Hence, the cooling was more effective with the pulsating flow and enhanced the cooling by 37.95%.



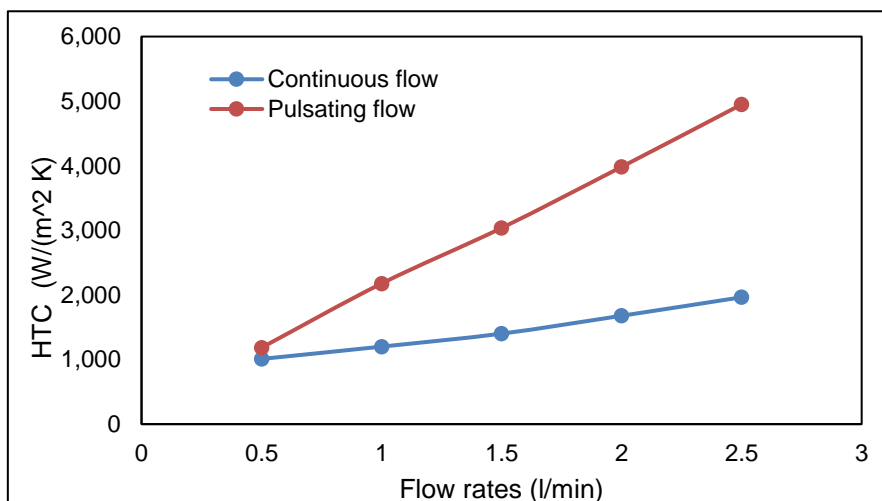
**Figure 4-10 Pulsating velocity against heat transfer enhancement and Womersley number**

The oscillating Reynolds number ( $Re_\omega$ ) and stable components Reynolds number ( $Re_s$ ) plot against velocity oscillating amplitude ( $A_o$ ) is displayed in Figure 4-11. With an increase in velocity oscillating amplitude from 0.05 to 0.27, the oscillating Reynolds number and stable components Reynolds number increases.



**Figure 4-11 Conventional design variation of oscillating Reynolds number ( $Re_\omega$ ), and stable components Reynolds number ( $Re_s$ ) against velocity oscillating amplitude at  $f = 0.5$**

In Figure 4-12, the relationship between the heat transfer coefficient and flow rate is depicted. Consistent with previous research [171], an increase in flow rate correlates with an increase in the heat transfer coefficient. The convective heat transfer is enhanced by promoting better fluid mixing and reducing the thickness of the thermal boundary layer. The pulsating flow shows higher flow turbulence and improved fluid mixing. Turbulent flow promotes greater fluid mixing and turbulence-induced fluctuations, which enhance heat transfer by facilitating better thermal contact between the fluid and the solid surface. Consequently, the convective heat transfer coefficient is further augmented.

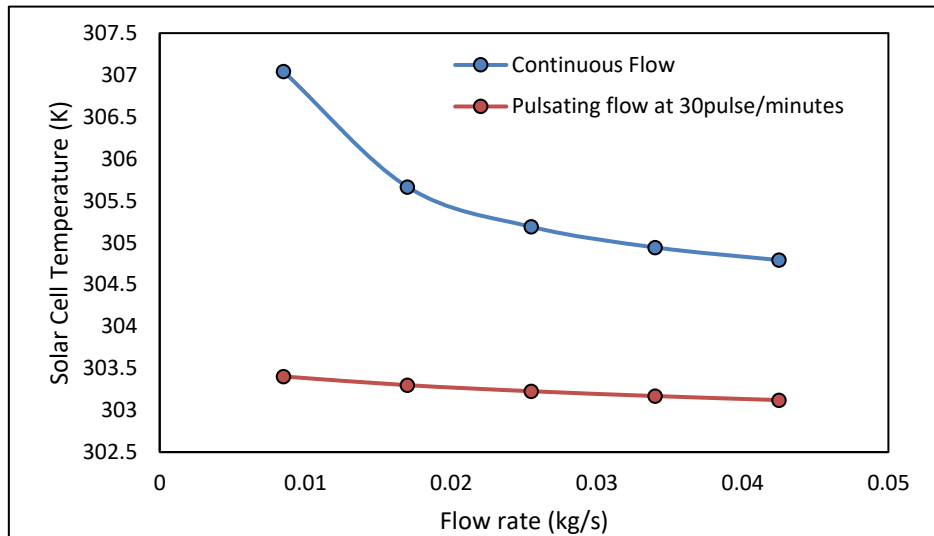


**Figure 4-12 Relationship of flow rate and heat transfer coefficient**



### 4.1.3 Parallel Design Without Baffles (Wout-B Design)

According to research, an increase in flow rate reduces cell temperature [120]. In this study, the solar cell temperature of both continuous and pulsing flows decreases as the flow rate increases. Figure 4–13 depicts the temperature of a solar cell versus the flow rate for both continuous and pulsing flow. It was discovered that the flow rate increased from 0.0085kg/s to 0.0425kg/s (5L/m to 2.5L/m). With uniform pulsing flow at 30 pulse/min, the temperature of the solar cell decreases from 303.40K to 303.12K and from 307.04K to 304.79K with continuous flow. The cell temperature is lower by 87.46% with pulsating flow compared to continuous flow. A comparison was made between the temperatures of a solar cell under continuous and pulsating flow conditions. Starting from an initial temperature of 298K, the temperature difference was found to be 6.79K for continuous flow and 5.12K for pulsating flow. Thus, more cell temperature uniformity was with the pulsating flow.



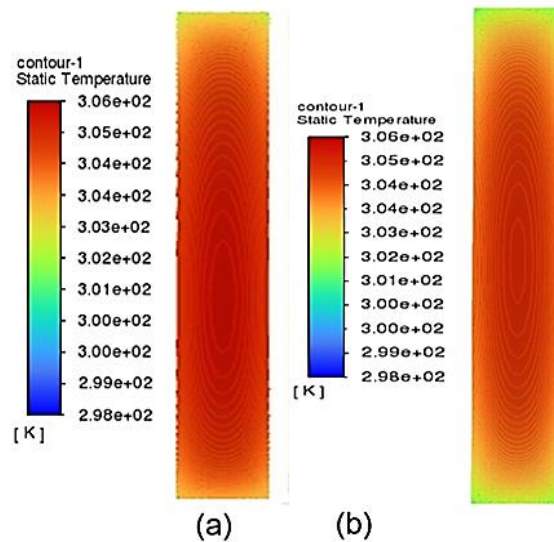
**Figure 4-13 Parallel Wout-B design solar cell temperature with continuous flow and pulsating flow at  $T = 2s$ ,  $f = 0.5Hz$ , 30puls/minutes,  $Pr = 5.70$  and  $Pr = 5.40$  respectively**

Comparing pulsating flow to continuous flow, the cell temperature is lower with the pulsing flow. The pulsating flow average cooling temperature enhancement ( $E_{puls-avg} = T_{cell-cont}/T_{cell-puls}$ ) was determined to be 1.01, where were  $T_{cell-cont}$  and  $T_{cell-puls}$  represent the average temperatures of the solar cell under



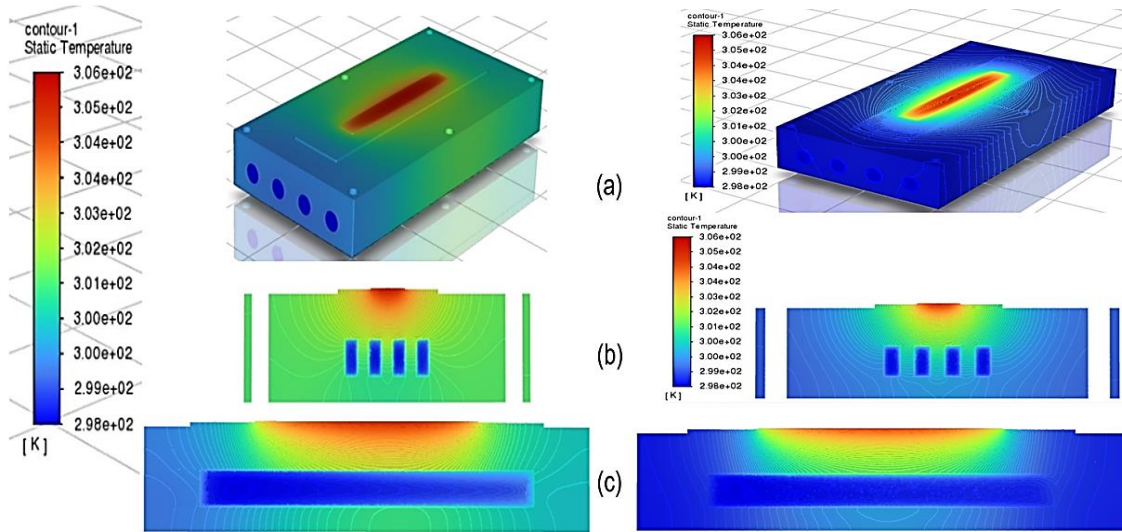
continuous and pulsating flow, respectively. A temperature contour map of the solar cell and cooling block was generated to understand the improvement better.

Figures 4-14 and 4-15 display a temperature contour of a solar cell and a cooling pad for both continuous and pulsating flow at a rate of 1L/m, respectively. Compared to continuous flow, pulsating flow with a period of 2 seconds and a frequency of 0.5Hz (Figure 4-14b) provides enhanced cooling at an equal maximum and lowest temperature range of 298K to 306K (Figure 4-14a).



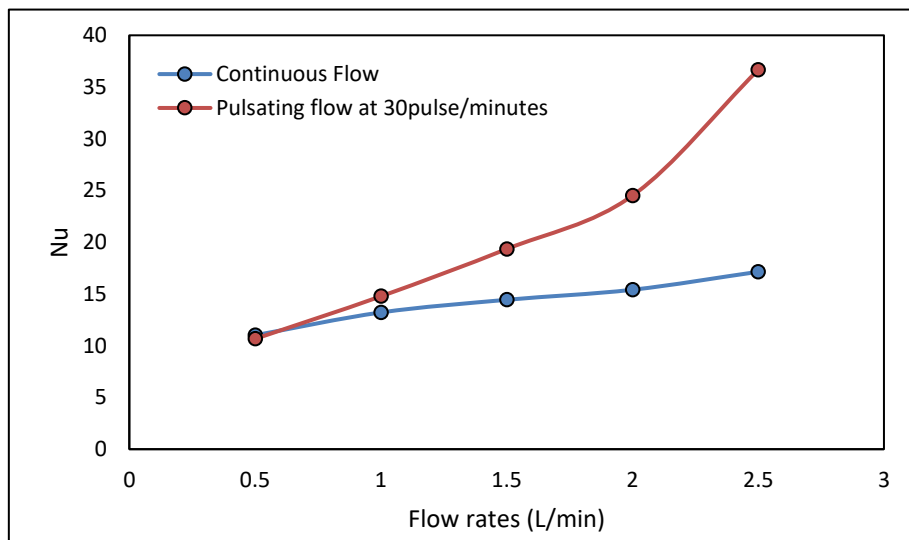
**Figure 4-14 Solar cell temperature contours at 1L/m, 150suns concentration (a) Continuous flow, (b) Pulsating flow**

Figure 4-15(a) depicts a 3D map of the temperature along the contour of the model for both continuous flow and pulsating flow at a rate of 1L/m. Figure 4-15(b) depicts the model's two-dimensional x-y centre cut-view temperature contour for both continuous and pulsating flow at a volumetric flow rate of one litre per minute. Figure 4-15(c) is a cutaway image of the centre channel in two dimensions showing the temperature contour of the cooling pad model for both continuous flow and pulsating. In comparison to continuous flow at equal maximum and lowest temperatures of 298K to 306K. The pulsating flow with a period of 2s and a frequency of 0.5hz, equal to 30 pulses per minute shown on the right of Figure 4-15, provides more effective cooling. This can be seen when compared with the temperature contour of Figure 4-15 on the left.



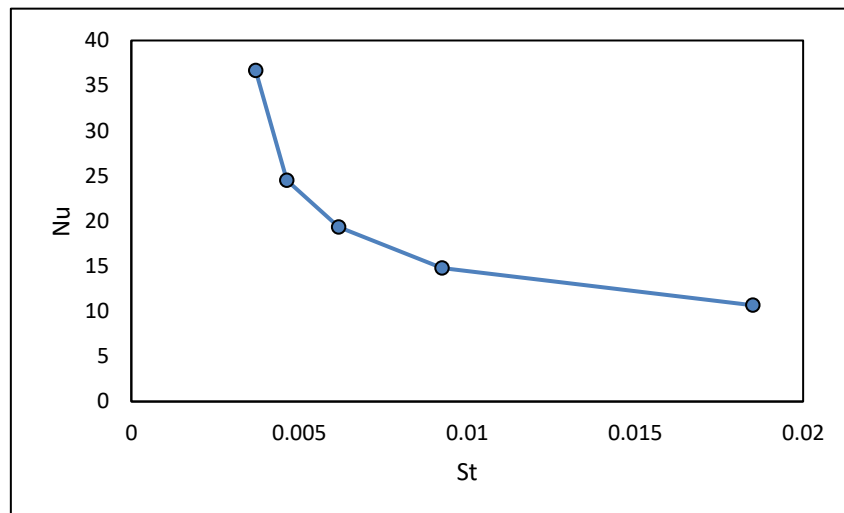
**Figure 4-15 Temperature contours at 1L/m, 150suns concentration parallel design without baffles (a) Complete 3D view, (b) 2D x-y centre cut-view (c) 2D z-y centre channel cut-view**

The Nusselt number was determined for continuous and uniform pulsing flows using equations 3-9. Figure 4-16 illustrates the Nusselt number as the flow rate increases from 5L/m to 2.5L/m for continuous steady flow and pulsating flow at 30 pulses/minute. In both flows, there was an increase in the Nusselt number. It ranges between 11.01 and 17.14 for continuous flow and between 10.66 to 36.66 for pulsating flow. This indicates that pulsating flow has more cooling effect than continuous flow.



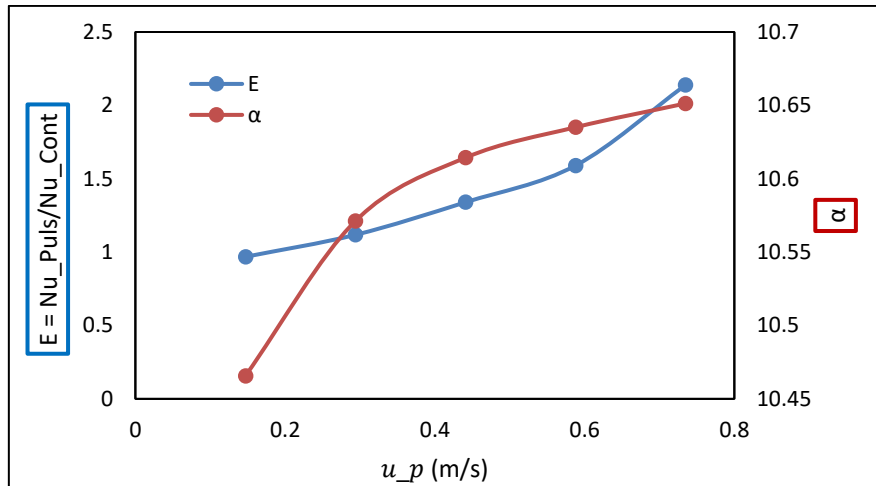
**Figure 4-16 Variation of Nusselt number with flow rate**

The dynamics of oscillating flow can be described using the Strouhal number in dimensionless analysis. Therefore, equation 3-20 was utilized to calculate the average Nusselt number, and a plot against the Strouhal number is presented in Figure 4-17. With a frequency of 0.5 Hz and a pulsing amplitude ranging from 0.05 to 0.27, a reduction in the Nusselt number is observed as the Strouhal number increases from 0.0037 to 0.0046, in agreement with [180]. These findings suggest the existence of an optimum Strouhal number that corresponds to an optimum Nusselt number.



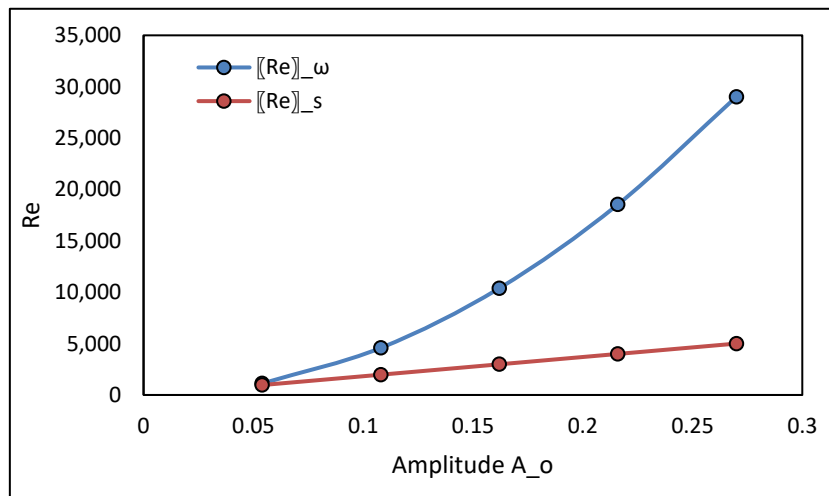
**Figure 4-17 Variation of Nusselt number against Strouhal number**

Variation of heat transfer enhancement ( $E$ ) and Womersley number ( $\alpha$ ) with Instantaneous velocity ( $u_p$ ) is seen in Figure 4-18. The Womersley number indicates whether the irregular profile of fluid flow in pulsing flow is constant. With an increase in instantaneous velocity from 0.14m/s to 0.73m/s, the Womersley number rises from 10.46 to 10.65. This indicates that the velocity profile is below the pulsing frequency. The enhancement ( $E$ ) of heat transfer with uniform pulsating (UP) flow in parallel design without baffles is 0.84 times lower the enhancement in conventional design. The enhancement varies from 0.96 to 2.14 with a velocity increase in parallel design without baffles. While a rise from 1.18 to 2.53 in the conventional design was obtained.



**Figure 4-18 Pulsating velocity against heat transfer enhancement and Womersley number**

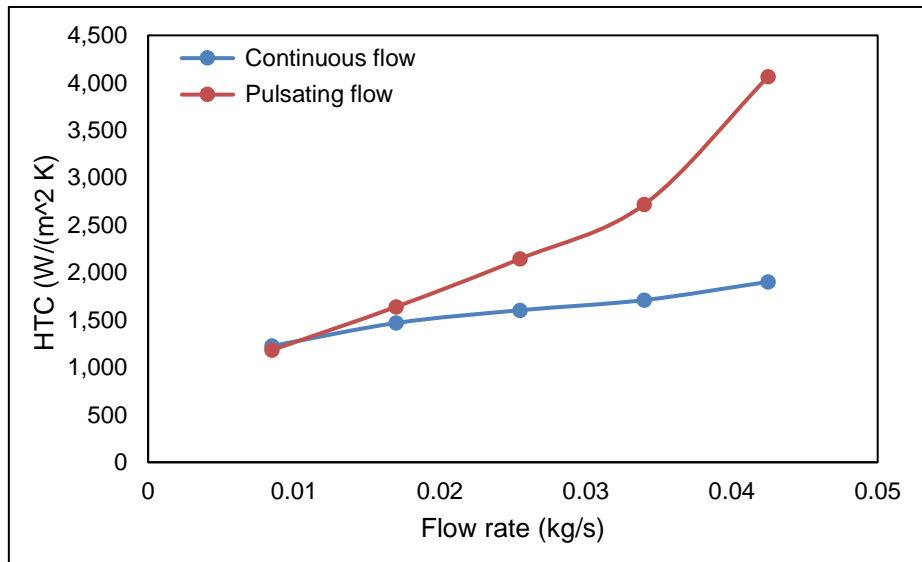
Figure 4-19 depicts the plot of the oscillating Reynolds number ( $Re_\omega$ ) and stable components Reynolds number ( $Re_s$ ) plot against velocity oscillating amplitude ( $A_o$ ). The oscillating Reynolds number and the stable components' Reynolds number increase when the velocity oscillation amplitude goes from 0.05 to 0.27.



**Figure 4-19 Parallel design without baffles variation of oscillating Reynolds number ( $Re_\omega$ ), and stable components Reynolds number ( $Re_s$ ) against velocity oscillating amplitude at  $f = 0.5$**

Figure 4-20 illustrates that an increase in flow rate is accompanied by an increase in the heat transfer coefficient, in line with previous research [171]. This relationship is attributed to improved fluid mixing, reduction in the thermal

boundary layer thickness, and enhanced convective heat transfer. The introduction of pulsating flow further augments the convective heat transfer coefficient by promoting turbulence and facilitating better thermal contact between the fluid and the solid surface. These findings provide valuable insights into optimizing heat transfer performance in various engineering applications.

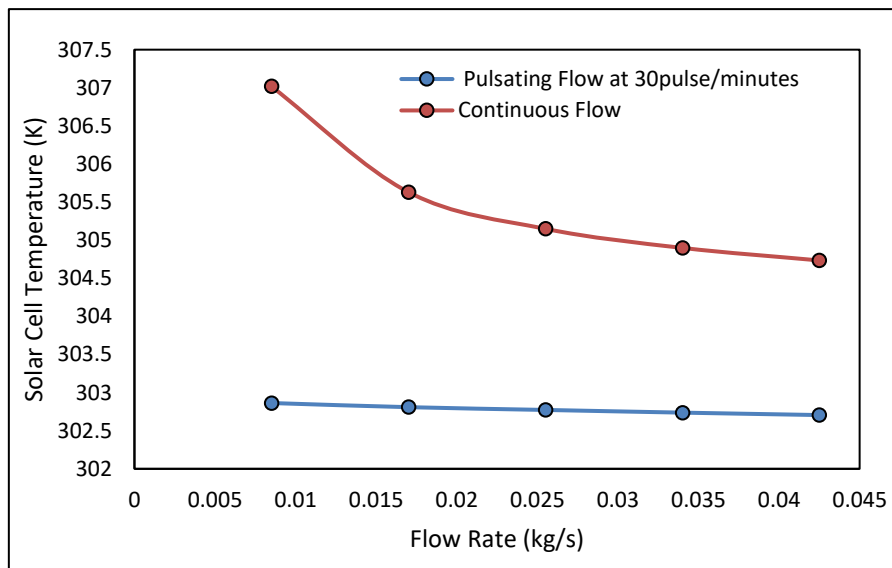


**Figure 4-20 Relationship of flow rate and heat transfer coefficient**

#### **4.1.4 Parallel Design With Baffles (WB-Design)**

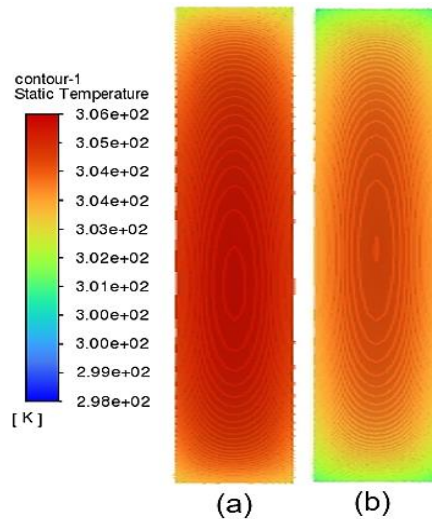
As the flow rate increases in this study, the solar cell temperature decreases for both continuous and pulsed flows. Previous research [120] also indicates that the cell's temperature decreases with an increase in flow rate. Figure 4-20 presents the relationship between the temperature of a solar cell and flow rate under both continuous and pulsed flow conditions. The study revealed that the flow rate increased from 0.0085kg/s to 0.0425kg/s (equivalent to 5L/m to 2.5L/m). With pulsed flow at 30 pulses per minute, the solar cell's temperature decreased from 302.86K to 302.71K, while during continuous flow, it decreased from 307.02K to 304.73K. Comparing the two flow conditions, the temperature of the cell was found to be 93.09% lower during pulsating flow than during continuous flow. Moreover, the temperature difference between the maximum and minimum recorded values for pulsating and continuous flow was determined to be 0.16 and 2.28, respectively. A lower cell temperature difference means that the cell

temperature uniformity. As such, pulsating flow is more effective.  $E_{puls-avg} = T_{cell-cont}/T_{cell-puls}$  It was calculated and found to be 14.49, where  $E_{puls-avg}$  is the pulsating flow average cooling enhancement,  $T_{cell-cont}$  and  $T_{cell-puls}$  the maximum and minimum values of the solar cell is lower with pulsating flow compared to continuous flow. This improvement is demonstrated in Figures 4-22 and 4-23, which depict temperature contour maps of the solar cell and cooling block, respectively



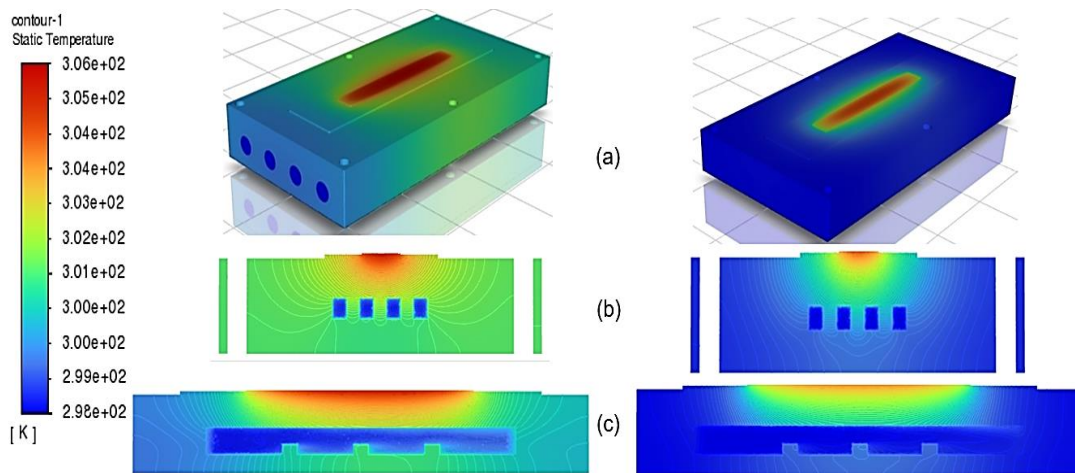
**Figure 4-21 Parallel WB-Design solar cell temperature with continuous flow and pulsating flow at  $T = 2s$ ,  $f = 0.5Hz$ , 30puls/minutes,  $Pr = 5.70$  and  $Pr = 5.40$ , respectively**

Figures 4-22 and 4-23 illustrate the temperature contour of a solar cell and cooling pad for both continuous and pulsed flow at a rate of 1L/m. These figures display the temperature contour ranging from 298K to 306K, representing equal maximum and minimum temperatures. When comparing continuous flow (Figure 4-22a) to pulsed flow with a duration of 2s and a frequency of 0.5 hertz (Figure 4-22b), it is evident that the latter offers improved cooling within the temperature range of 298K to 306K.



**Figure 4-22 Solar cell temperature contours at 1L/m, 150suns concentration (a) Continuous flow, (b) Pulsating flow**

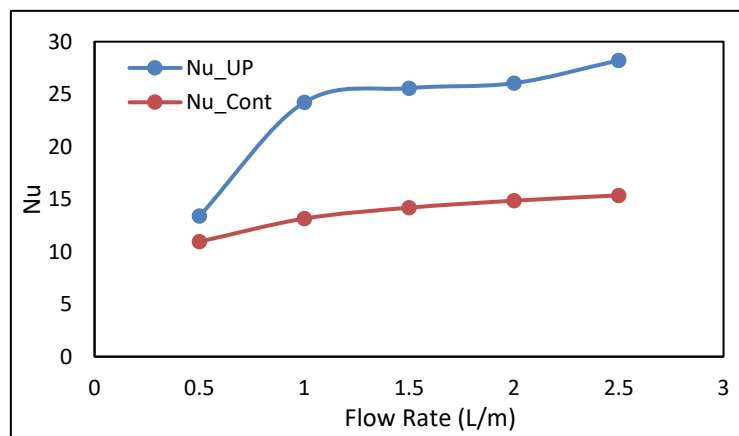
The temperature contour along the complete coupled models is shown in 3D in Figure 4-23(a) for both continuous and pulsed flow at a rate of 1L/m. Figure 4-23(b) shows the model's 2D x-y centre cut-view temperature contour for both continuous flow and pulsed flow, while a cut-view of the centre channel in 2D is shown in Figure 4-33c. Continuous flow is less efficient in cooling (Figure 4-23 left) than pulsed flow at the period of 2s and pulsating frequency of 0.5hertz (30 pulses per minute) seen on the right in Figure 4-23.



**Figure 4-23 Temperature contours at 1L/m, 150suns concentration parallel design (a) Complete 3D view, (b) 2D x-y centre cut-view (c) 2D z-y centre channel cut-view**



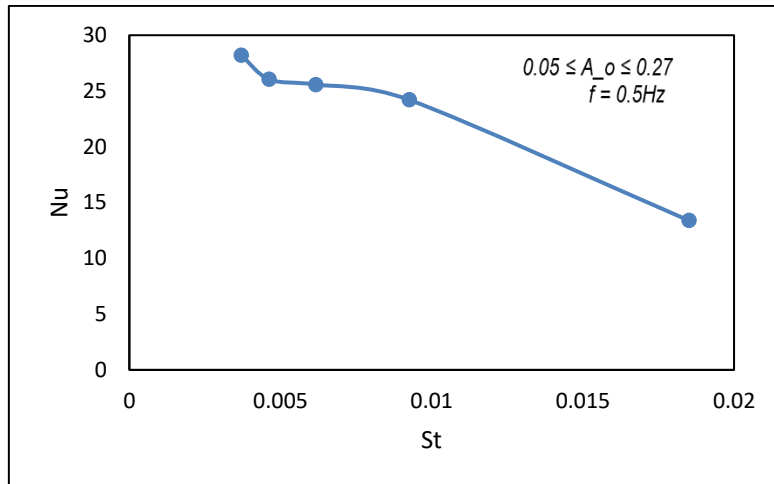
The Nusselt number is an essential dimensionless quantity in heat transfer. Equations 3-9 and 3-16 were thus used to get the Nusselt number for continuous and pulsating flows, respectively. Figure 4-24 shows how the Nusselt number varies when the flow rate drops from 0.5L/m to 2.5L/m for continuous steady flow and 30 pulses/minute for pulsating flow. The Nusselt number rose in each of the two flows. It varies from 10.95 to 15.36 for constant flow and from 13.38 to 28.21 for pulsating flow. Constant Nu was observed between 1L/m to 2L/m, then raise to a maximum at 2.5L/m. This shows that more convection occurs when the flow was pulsed than when the flow was continuous.



**Figure 4-24 Variation of Nusselt number with flow rate parallel WB-design**

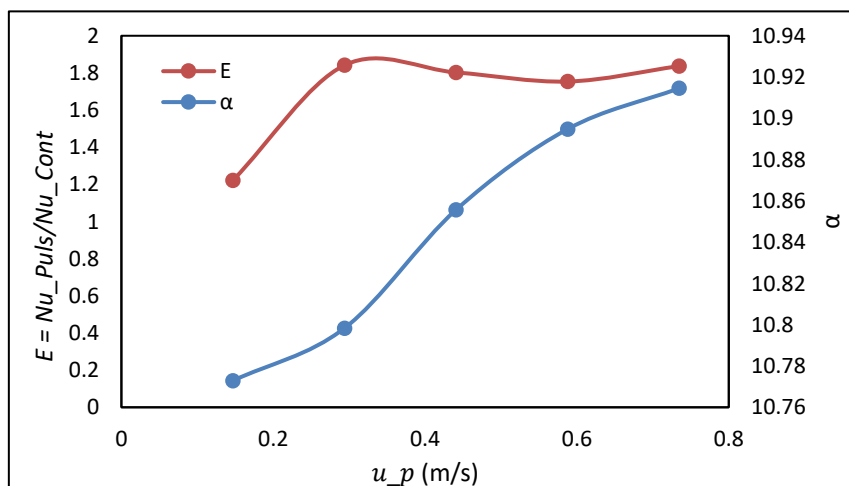
The oscillating flow dynamics may be described using the Strouhal number in dimensionless analysis. Equation 3-20 was used to compute the average Nusselt number, and a plot against the Strouhal number is shown in Figure 4-25, with a pulsing dimensionless amplitude range of  $0.05 \leq A_o \leq 0.27$  and frequency of 0.5Hz, a reduction in the Nusselt number occurs with an increase in the Strouhal number from 0.0037 to 0.0046, which agrees with [180]. However, a constant Nusselt number was observed with the Strouhal number increased between 0.0046 to 0.0061, and a sudden drop in the Nusselt number was observed with a further increase in the Strouhal number from 0.0080 to 0.0185. This result of Nusselt number fluctuation is compatible with [173,183]. The fluctuation could be the effect of baffles and pulsating nature of the flow. In addition, it also indicates that there exists an optimum Strouhal number to have an optimum Nusselt number.





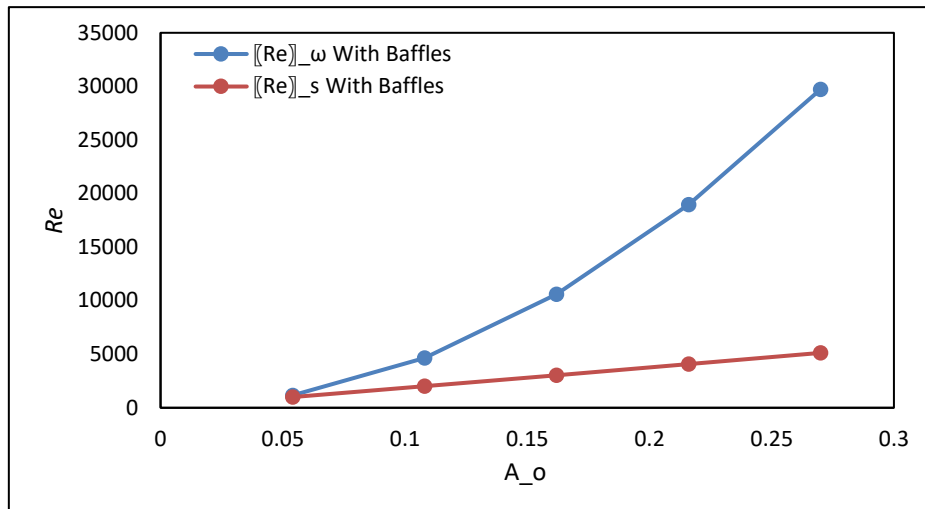
**Figure 4-25 Variation of Nusselt number with Strouhal number parallel WB-design**

Variation of heat transfer enhancement  $E$  and Womersley number ( $\alpha$ ) with Instantaneous velocity ( $u_p$ ) is displayed in Figure 4-26. The Womersley number indicates whether the distinctive character of fluid flow in pulsing flow is constant. With an increase in instantaneous velocity from 0.14m/s to 0.73m/s, the Womersley number rises from 10.77 to 10.91. This indicates that the velocity profile is below the pulsing frequency. The enhancement ( $E$ ) of heat transfer with uniform pulsating (UP) flow in parallel design with baffles is 5.3 times the enhancement in conventional design. The enhancement varies from 1.22 to 1.83, with maximum recorded at 0.29m/s instantaneous pulsating velocity in parallel design without baffles.



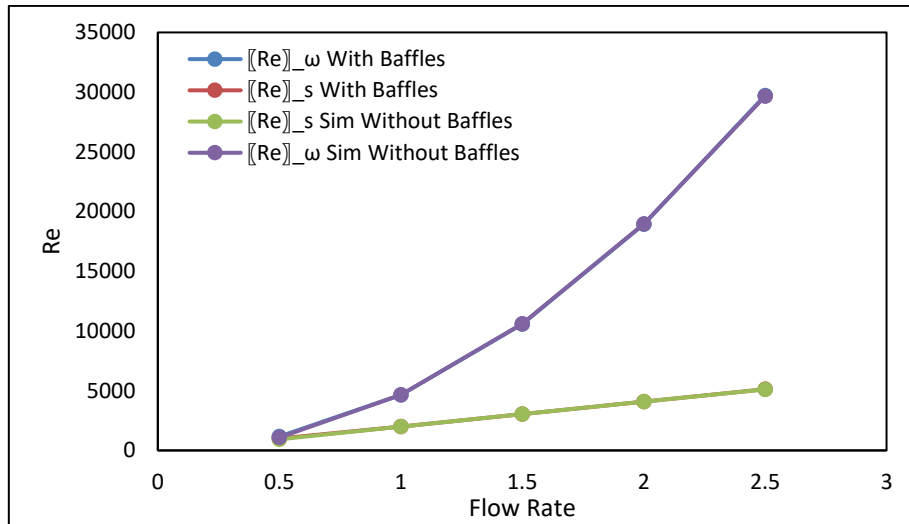
**Figure 4-26 Parallel WB-design pulsating velocity against enhancement and Womersley number**

Figure 4-27 depicts the plot of the oscillating Reynolds number ( $Re_\omega$ ) and stable components Reynolds number ( $Re_s$ ) plot against velocity oscillating amplitude ( $A_o$ ). The oscillating Reynolds number and the stable components' Reynolds number increase when the velocity oscillation value amplitude goes from 0.05 to 0.27. This result agrees with the parallel design without baffles of this study.



**Figure 4-27 Parallel WB-design pulsating amplitude at  $f = 0.5$  against oscillating Reynolds number ( $Re_\omega$ ), and stable components Reynolds number ( $Re_s$ ) plot against velocity oscillating amplitude**

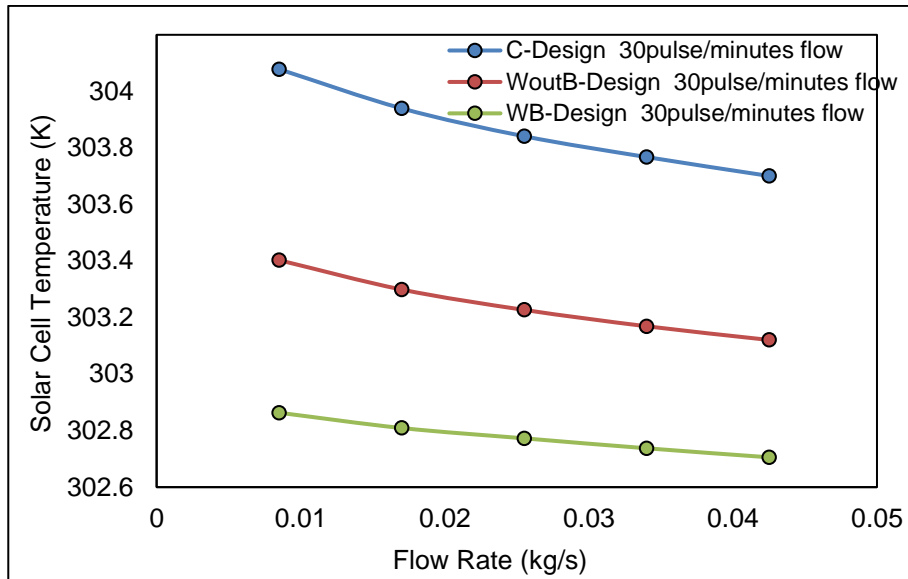
To validate the parallel design with baffles, a plot of both parallel designs a plot of the flow rate against oscillating Reynolds number ( $Re_\omega$ ) and stable components Reynolds number ( $Re_s$ ) is shown in Figure 4-28. In both situations, an increase in flow rate causes the Reynolds numbers to rise. Reynolds number increases with flow rate, according to research [181,182]. The stable components Reynolds number is a function of instantaneous pulsing velocity, while the oscillating Reynolds number depends on the dimensionless amplitude of the pulsation. Both designs agree.



**Figure 4-28 Variations of flow rate versus Reynolds number parallel WB-design**

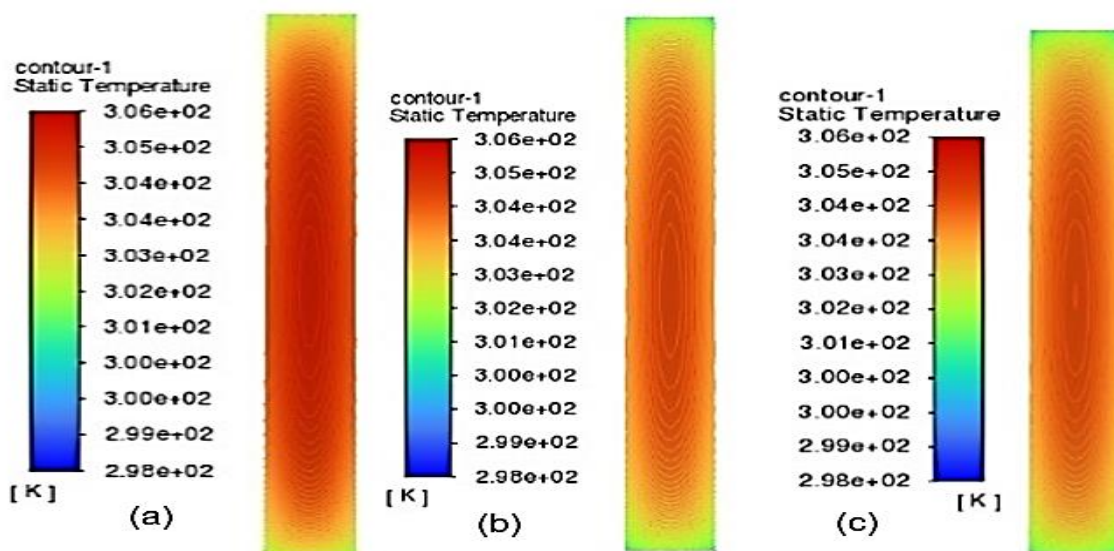
#### **4.1.5 Design Cross Comparison**

Increasing flow rate decreases cell temperature, a study shows [120]. Both continuous and pulsed flow lower solar cell temperature in this investigation. Figure 4–29 shows solar cell temperature against flow rate for the three designs considered in this research with the pulsed flow. With flow increased from 0.0085kg/s to 0.0425kg/s (5L/m to 2.5L/m). Solar cell temperature drops with 30puls/min pulsing flow from 304.07K to 303.70K, 303.40K to 303.12K and 302.86K to 302.70K for conventional design (C-Design), parallel design without baffles (WoutB-Design) and parallel design with baffles (WB-Design) respectively. To see the performance, a solar cell temperature contour map was displayed (figure 4-30). The solar cell temperature with the pulsating flow was cooled 52.65% more efficiently with WoutB-Design than with conventional design. The cell temperature was cooling with pulsating flow 57.08% more efficiently with the parallel WB-Design than conventional design.



**Figure 4-29 Design cross-comparison with pulsating flow variations of flow rate versus solar cell temperature**

The temperature contour of the solar cell as a design cross-comparison with the pulsating flow at 1L/m, period of 2s and frequency of 0.5hertz is displayed in Figures 4-30. At equal temperature intervals, the parallel design shows more temperature uniformity and lower solar cell temperature than the conventional design. This is compatible with the result plotted in Figure 4-29.



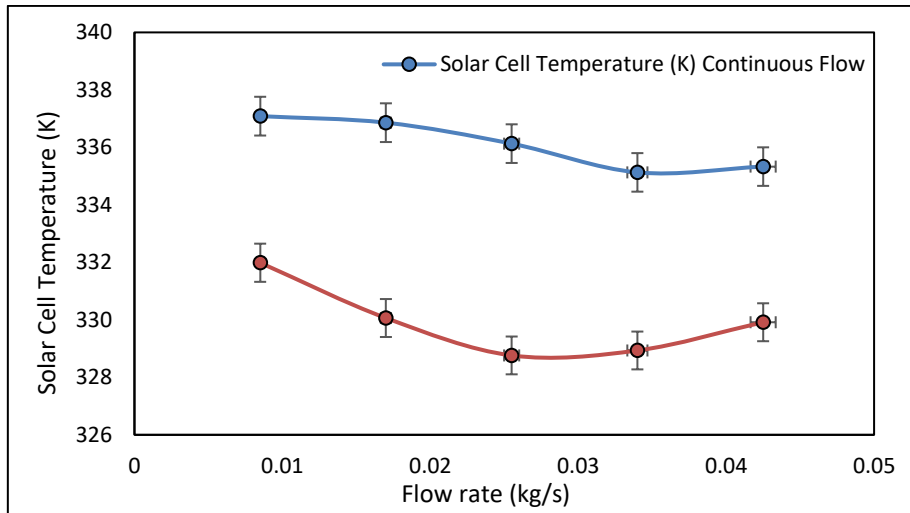
**Figure 4-30 Solar cell temperature contours at 1L/m, 150suns concentration, and 30puls/minutes and (a) Conventional design, (b) Parallel design without baffles and (c) Parallel design with baffles**

## **4.2 Experimental Results**

The experiment investigated both continuous and pulsating flow using a high-flux sun simulator considering the conventional design and parallel design without baffles. Three mode of flow was investigated continuous flow, uniform pulsating flow and bio-inspired pulsating flow. The bio-inspired cooling approach presented in this study is specifically applicable to the parallel design, unlike the constant pulsation method where all valves are simultaneously opened and closed, resulting in a complete flow pump to all channels simultaneously. In contrast, the bio-inspired pulsation concept involves pumping the total flow to two channels simultaneously, with two valves open and the other two closed.

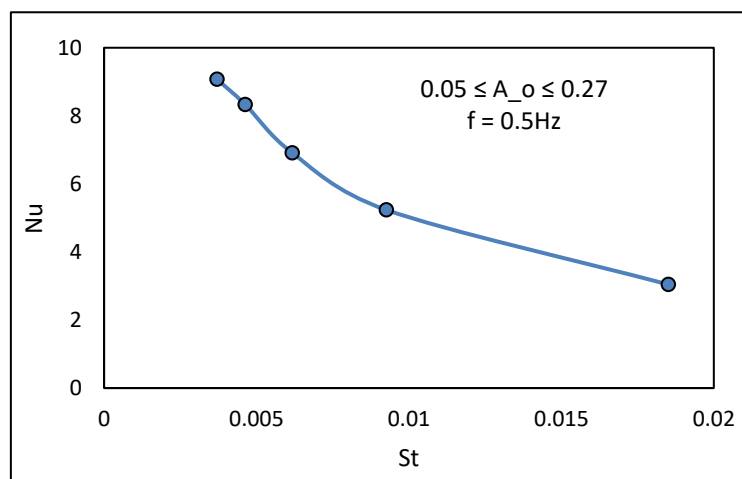
### **4.2.1 Conventional Design Experimental Result**

Figures 4-31 depict the relationship between solar cell temperature and flow rate for experiments conducted with both conventional and parallel design without baffles. [107] reported that an increase in flow rate results in a decrease in cell temperature. The results reveal that, in the C-design, the temperature of the solar cell is lower during pulsating flow compared to continuous flow. The with flow rate increases from 0.5L/m to 2.5L/m and uncertainty of  $\pm 0.2\%$ , the cell temperature decreases from 337.09K to 335.33K under continuous flow with uncertainty 2%. In contrast, the cell temperature decreases from 331.98K to 329.92K under uniform pulsating flow at a rate of 30 pulses per minute. The error bars indicated the uncertainty of the temperature sensor and flow meter. These findings demonstrate that the cell's temperature is lower with pulsating flow compared to continuous flow.



**Figure 4-31 Solar cell temperature with continuous flow and pulsating flow at  $T = 2s$ ,  $f = 0.5Hz$ , 30puls/minutes,  $Pr = 5.70$  and  $Pr = 5.40$ , respectively**

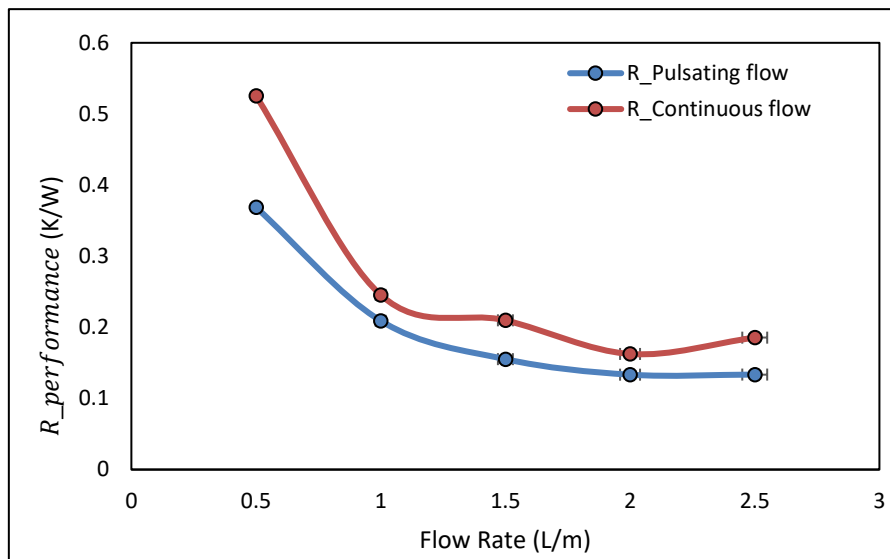
The Strouhal number is a dimensionless parameter that characterizes the dynamics of oscillating flow. In the context of this analysis, an increase in the Strouhal number corresponds to a decrease in the Nusselt number within the frequency range of 0.5 Hz and  $0.05 \leq A_o \leq 0.27$ , as supported by the findings reported in [180]. Figure 4-32 illustrates the relationship between the Nusselt number and the calculated Strouhal number, obtained using equations 3-20.



**Figure 4-32 Variation of Nusselt number against Strouhal number**

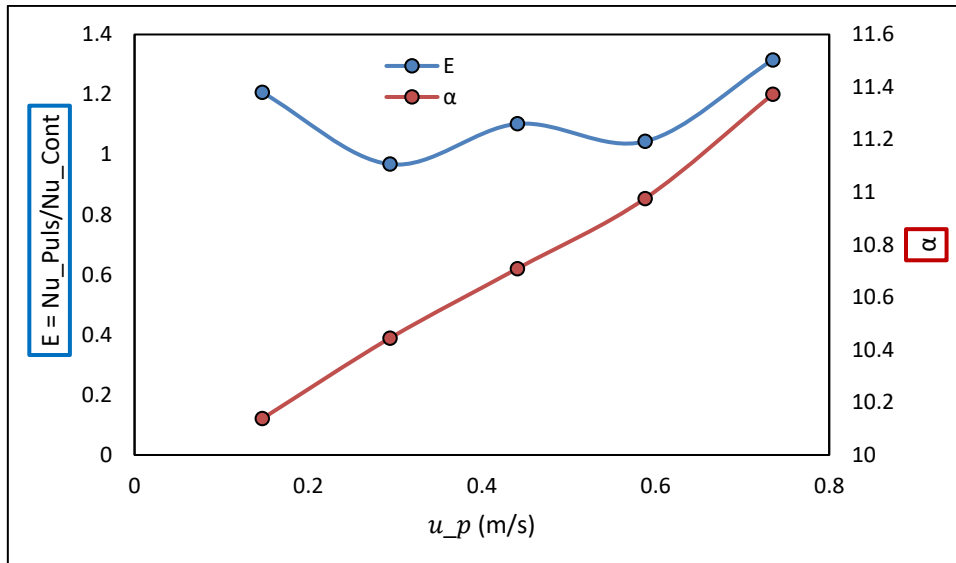
A more comprehensive measure of the system's thermal performance is provided by the overall thermal resistance as shown in Figure 4-33. This measure is

defined as  $R_{performance} = \Delta T/q$ , where  $q$  is the heat flux,  $\Delta T$  represents the temperature difference between the maximum cell temperature (as indicated by the thermocouple reading in the solar cell) and the fluid inlet temperature. The  $R_{performance}$  lower from 0.36K/W to 0.13K/W with an increase in flow rate from 0.5 to 2.5L/m with the pulsating flow. While  $R_{performance}$  lower from 0.52K/W to 0.16K/W. The lower thermal resistance justified the enhances cooling with pulsating flow.



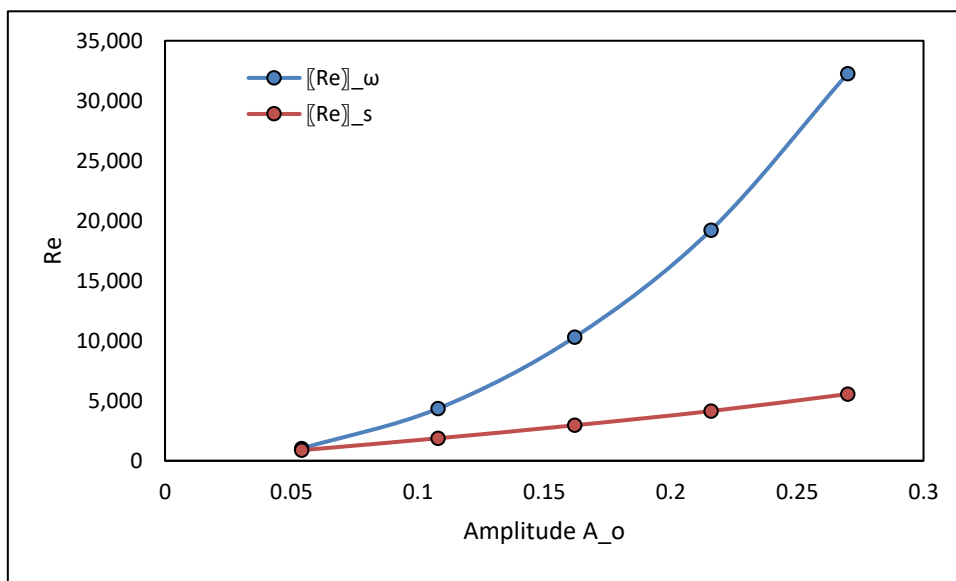
**Figure 4-33 Performance thermal resistance versus flow rate**

Figure 4-34 shows that the Womersley number ( $\alpha$ ) increases from 10.13 to 11.37 as the instantaneous velocity ( $u_p$ ) increases from 0.14 m/s to 0.73 m/s. This suggests that the velocity profile is below the pulsing frequency. The enhancement fluctuates between minimum value of 0.97 to a maximum of 1.32. These means that an optimum enhancement exist with increase in instantaneous velocity. Although, the pulsating flow demonstrates a greater reduction in solar cell temperature compared to non-pulsating flow.



**Figure 4-34 Pulsating velocity variation with cooling enhancement and Womersley number**

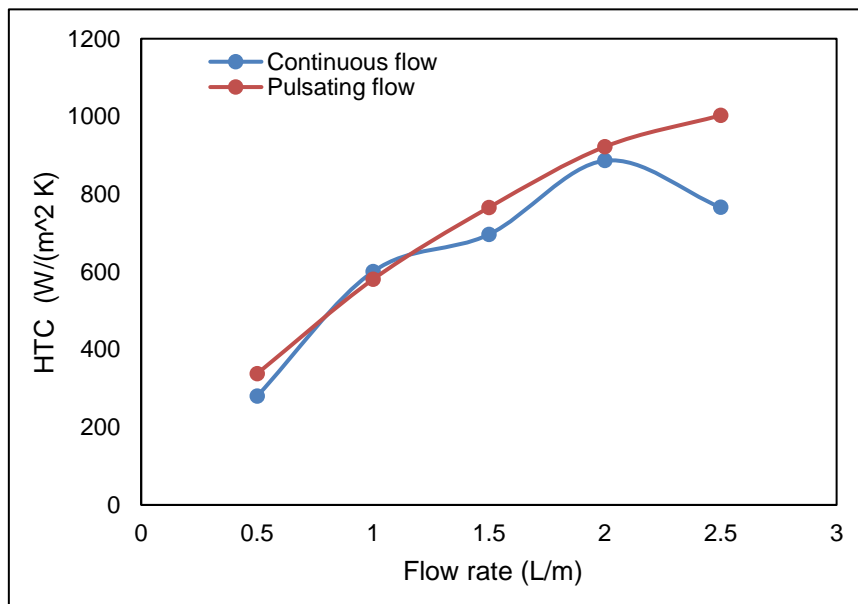
Figure 4-35 shows that the oscillating Reynolds number ( $Re_\omega$ ) and the stable components Reynolds number ( $Re_s$ ) increase with flow rate. This is in line with [181,182] research, which has shown that the Reynolds number increases with flow rate. The stable components Reynolds number is a function of the instantaneous pulsating velocity, while the oscillating Reynolds number depends on the dimensionless amplitude of the pulsation.



**Figure 4-35 Variations of Reynolds number versus pulsating amplitude**



The overall heat transfer coefficient tends to increase with higher coolant flow rates as shown in Figure 4-36. Increased flow rates enhance convective heat transfer through better fluid mixing and reduced thermal boundary layer thickness. With the pulsating flow, the turbulent flow enhances fluid mixing, promoting better thermal contact and heat transfer, enabling more efficient thermal energy exchange. However, continuous flow irregular pattern can be attributed to several factors. According to [3], this is an uncontrollable external factor. Their research stated that ambient temperature, dust accumulation, incident radiation rate, and wind velocity are uncontrollable factors. In contrast, the solar cell temperature is categorised controllable factor. The heat transfer coefficient is a function of both fluid and cooling pad temperatures. As such, there was a slight decrease in the experimental heat transfer coefficient at 2.5L/m, which is associated with increased ambient temperature. Optimal design should consider balancing flow rate to maximize heat transfer efficiency. Understanding this relationship is crucial for optimizing heat transfer systems in diverse engineering applications.

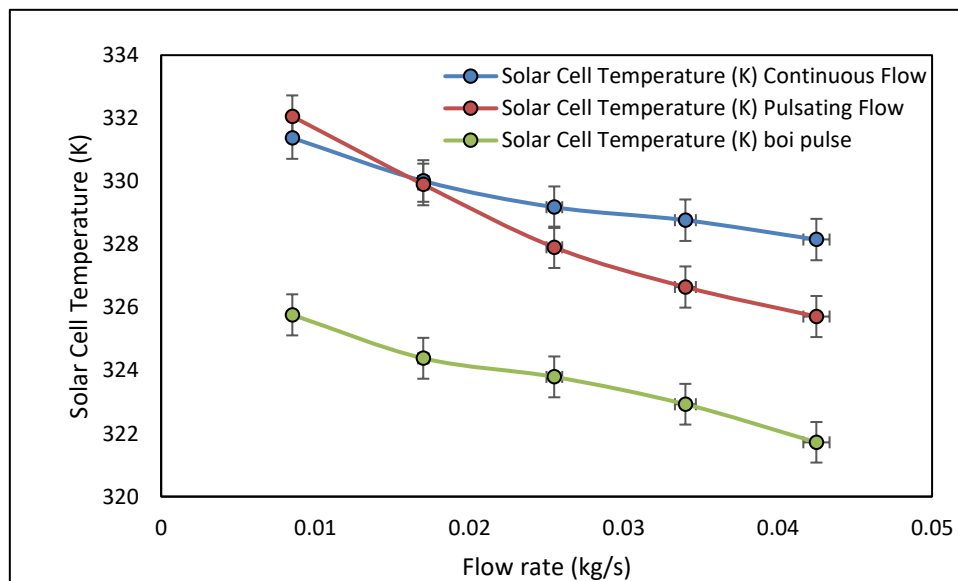


**Figure 4-36 Variations of flow rate versus heat transfer coefficient**

#### 4.2.2 Parallel Design Without Baffles Experimental Result

In this study, we introduced a bio-inspired cooling approach specifically applicable to the parallel design. Figure 4-29 shows the relationship between solar cell temperature and flow rate for experiments conducted with both conventional and parallel design without baffles. As reported in [107], an increase in flow rate results in a decrease in cell temperature.

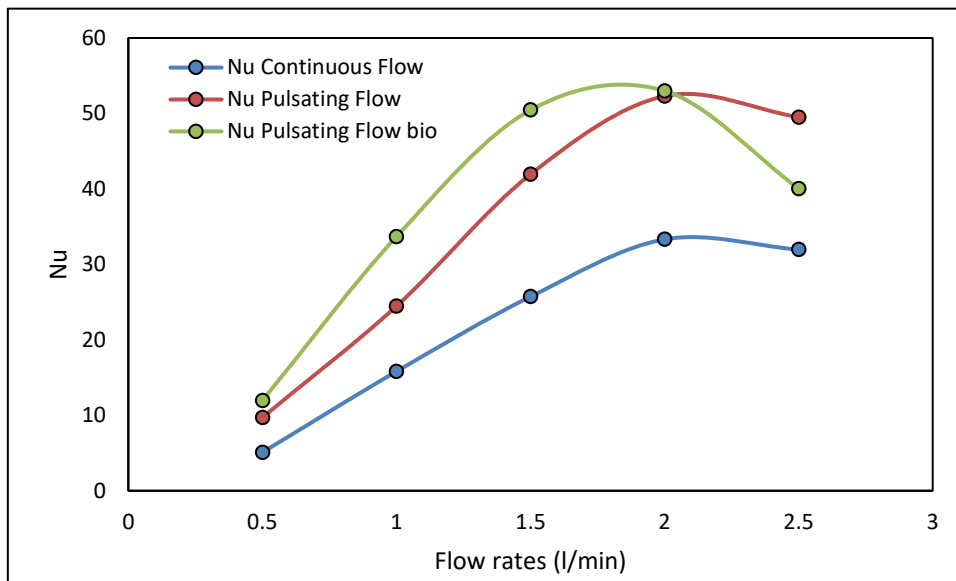
Figure 4-37 shows the results in the WoutB-design, the temperature of the solar cell is lower during pulsating flow compared to continuous flow. With a flow rate increase from 0.5L/m to 2.5L/m and uncertainty of  $\pm 0.2\%$ , the cell temperature decreases from 331.38K to 328.15K under continuous flow, with uncertainty of 2%. In contrast, at a rate of 30 pulses per minute the cell temperature decreases from 332.06K to 325.71K under uniform pulsating flow, and 325.76K and 321.72K with the bio-inspired pulsating flow. The error bars indicate the uncertainty of the temperature sensor and flow meter. These findings demonstrate that the cell's temperature is lower with pulsating flow compared to continuous flow.



**Figure 4-37 Solar cell temperature at 1L/m, 150suns concentration, and 30puls/minutes**

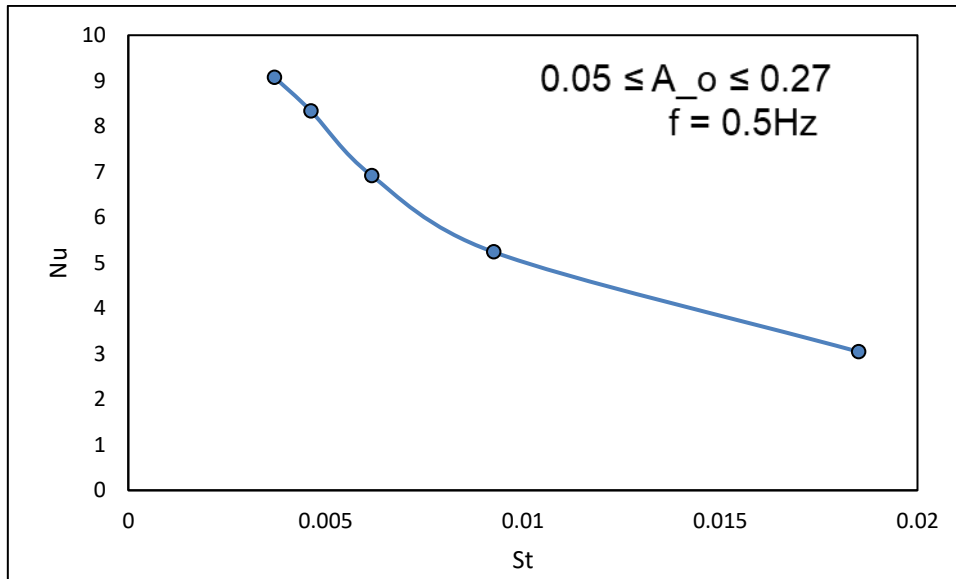
The Nusselt number was determined for continuous flow and uniform pulsating flow using equations 3-9. Figure 4-38 visually depicts the fluctuation of the Nusselt number as the flow rate increases from 0.5L/m to 2.5L/m for both

continuous flow and pulsating flow at 30 pulses per minute. Notably, in both flow conditions, an increase in the Nusselt number was observed. The Nusselt number ranged from 5.08 to 31.96 for continuous flow, 9.70 to 49.51 for uniform pulsating flow, while it ranged from 11.94 to 40.03 with bio-inspired flow. These results demonstrate that pulsating flow has a more pronounced cooling effect compared to continuous flow. Pulsating flow vibration was observed with uniform pulsation. At 2L/m, these vibration leads to cracks which have effect on the system integrating and may affect the result.



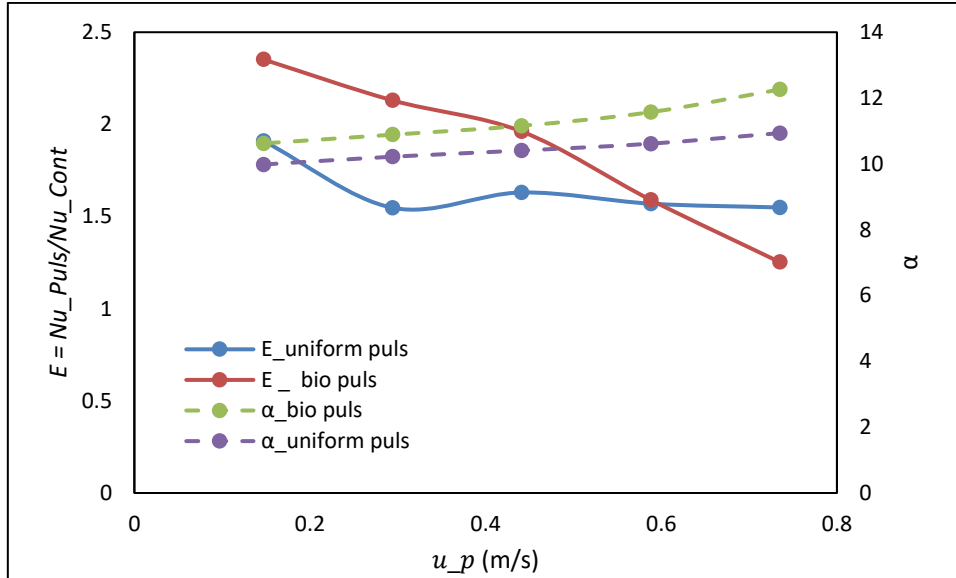
**Figure 4-38 Variation of Nusselt number against flow rate**

The Strouhal number, a dimensionless parameter that characterizes oscillating flow dynamics, exhibits an inverse relationship with the Nusselt number in the frequency range of 0.5 Hz and  $0.05 \leq A_o \leq 0.27$ , in line with the findings presented in [180]. This relationship is depicted in Figure 4-39, where the Nusselt number is plotted against the calculated Strouhal number, obtained through equations 3-20.



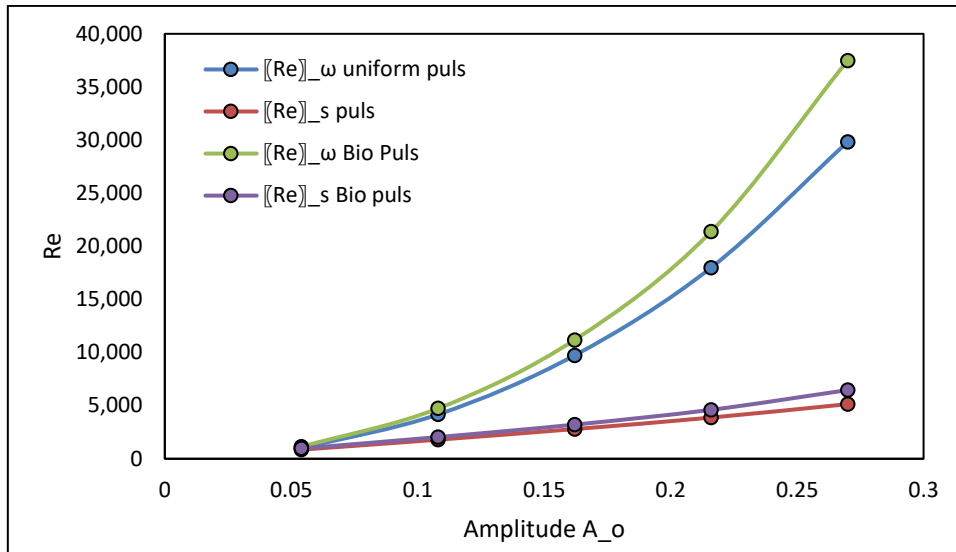
**Figure 4-39 Variation of Nusselt number against Strouhal number**

Figure 4-40 illustrates that the Womersley number ( $\alpha$ ) increases from 9.98 to 10.93 with uniform pulsating flow, and from 10.62 to 12.25 with bio-inspired pulsating flow, as the instantaneous velocity ( $u_p$ ) rises from 0.14m/s to 0.73m/s. This observation suggests that the velocity profile operates below the pulsing frequency. The heat transfer enhancement drops from a maximum of 1.55 to a minimum value of 1.91 with uniform pulsating flow, while it varies between a minimum value of 1.25 and a maximum of 2.35 with bio-inspired pulsating flow. Between 0.59m/s to 0.73m/s instantaneous velocity the bio-inspired pulsating flow enhancement was lower than the uniform pulsating flow. These means that the Womersley number ( $\alpha$ ) has effect in the colling enhancement. A higher Womersley number in the bio-inspired flow leads to the lower enhancement. These findings indicate the existence of an optimum enhancement with an increase in Womersley number and instantaneous velocity. Moreover, the pulsating flow demonstrates a greater reduction in solar cell temperature compared to non-pulsating flow.



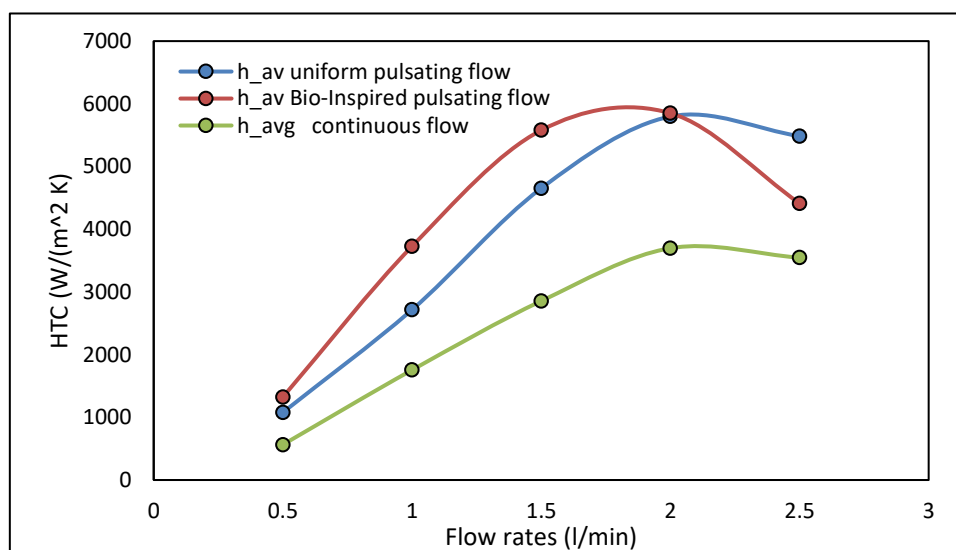
**Figure 4-40 Pulsating velocity variation with cooling enhancement and Womersley number**

Figure 4-41 provides valuable insights into the behaviours of oscillating Reynolds number ( $Re_{\omega}$ ) and stable components Reynolds number ( $Re_s$ ) in uniform and bio-inspired pulsating flow conditions. The results indicate a consistent rise in both  $Re_{\omega}$  and  $Re_s$  with increasing flow rate, in line with similar research [181,182]. Notably, the stable components Reynolds number is influenced by instantaneous pulsing velocity, reflecting the impact of stable flow components on overall flow dynamics. Conversely, the oscillating Reynolds number is dependent on the dimensionless amplitude of pulsation, indicating its influence on flow oscillations. Understanding the relationship between Reynolds numbers and flow rate is crucial for characterizing flow dynamics and predicting fluid behaviours in various pulsating flow scenarios. These insights contribute to the broader understanding of flow characteristics and assist in the design and optimization of systems involving pulsating flows.



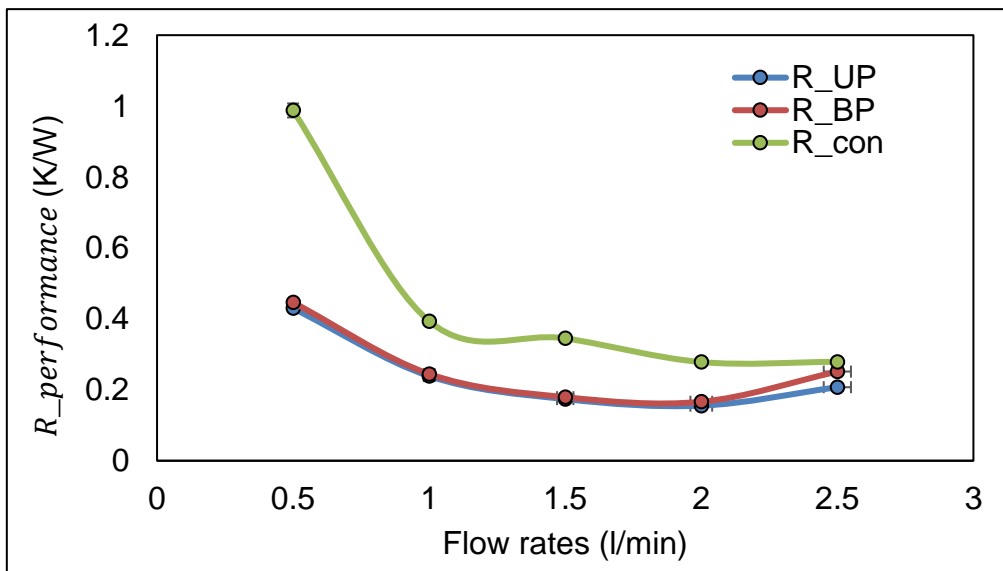
**Figure 4-41 Variations of Reynolds number versus pulsating amplitude**

Figure 4-42 illustrates that an increase in flow rate is accompanied by an increase in the heat transfer coefficient, in line with previous research [171]. This relationship is attributed to improved fluid mixing, reduction in the thermal boundary layer thickness, and enhanced convective heat transfer. The introduction of pulsating flow further augments the convective heat transfer coefficient by promoting turbulence and facilitating better thermal contact between the fluid and the solid surface. These findings provide valuable insights into optimizing heat transfer performance in various engineering applications.



**Figure 4-42 Variations of flow rate versus heat transfer coefficient parallel**

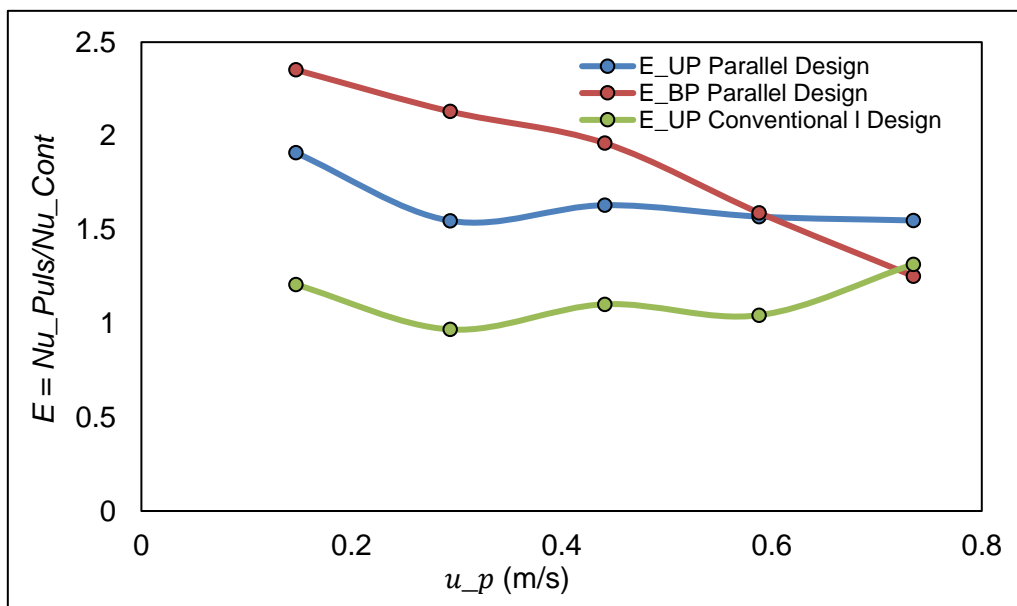
A further measure of the system's thermal performance is provided by the overall thermal resistance, known as  $R_{performance} = \Delta T/q$ . This measures the relationship between the temperature difference  $\Delta T$  and the heat flux ( $q$ ), where  $\Delta T$  represents the variation between the maximum cell temperature (determined by the thermocouple reading in the solar cell) and the fluid inlet temperature. Figure 4-43 shows that uniform pulsating flow leads to a reduction in  $R_{performance}$  from 0.43K/W to 0.21K/W as the flow rate increases from 0.5 L/m to 2.5 L/m. While, a reduction in  $R_{performance}$  from 0.446K/W to 0.25K/W was observed with bio-inspired pulsating flow. Similarly, with continuous flow,  $R_{performance}$  decreases from 0.99K/W to 0.28K/W. These lower thermal resistances justify the enhanced cooling achieved with pulsating flow. The presence of error bars in the serves to indicate the level of uncertainty associated with measurements.



**Figure 4-43 Performance thermal resistance versus flow rate**

Figure 4-44 provides a comparative analysis of the two pulsed flow approaches in terms of cooling enhancement ( $E$ ), based on conventional design and the parallel design without-baffles. The maximum enhancement achieved is 2.35 for the bio-inspired pulsating flow, 1.91 for uniform pulsating flow with the parallel design, and 1.32 for uniform pulsating flow with the conventional design. The bio-inspired pulsating flow with the parallel design demonstrates a remarkable efficiency of 28.28% compared to uniform pulsating flow with the conventional

design. Similarly, the uniform pulsating flow with the parallel design exhibits a 18.44% higher efficiency compared to uniform pulsating flow with the conventional design. Notably, the bio-inspired pulsating flow with the parallel design proves to be 10.37% more effective than uniform pulsating flow with the parallel design. However, at instantaneous velocity of 0.59m/s to 0.73m/s the bio-inspired pulsating flow enhancement was lower than the uniform pulsating flow parallel design. These is due to the higher Womersley number ( $\alpha$ ) obtained with the bio-inspired at higher flow rate. These means that the Womersley number ( $\alpha$ ) has effect in the colling enhancement.

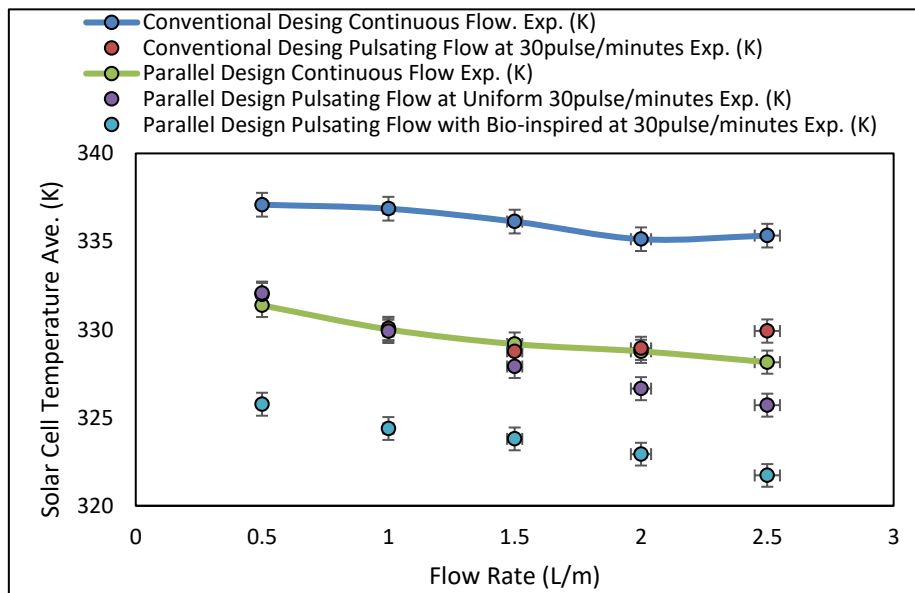


**Figure 4-44 Pulsating velocity variation with cooling enhancement and Womersley number**

Figures 4-45 show the solar cell temperature versus flow rate for conventional and parallel design without baffles design experiments. [107] reported that an increase in flow rate decrease cell. The result shows that the pulsating flow temperature is lower compared to continuous flow in the C-design. Similarly, in the C-design, with an increase in flow rate from 0.5L/m to 2.5L/m, the cell temperature drops from 337.09K to 335.33K with continuous flow. At the same time, cell temperature drops from 331.98K to 329.92K with the uniform pulsating flow at 30 puls/minute. This shows that the cell's temperature is lower with pulsating flow compared to the cell's continuous flow temperature. The parallel



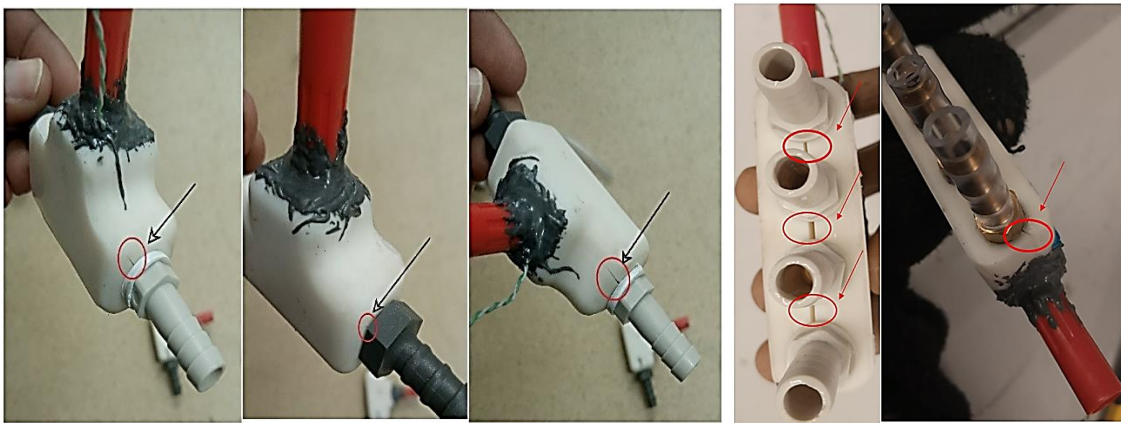
Wout-B design result shows that the solar cell temperature is higher with the uniform pulsating flow at 0.5L/m, slightly lower at 1L/m and then lower from 1L/m to 2.5L/m compared with continuous flow. In addition, the uniform pulsating flow with parallel Wout-B design cell temperature is lower than both continuous and uniform pulsating flow C-design. Parallel Wout-B design cell temperature drops from 331.37K to 335.33K and 332.06K to 325.71K with continuous flow and uniform pulsating flow, respectively. However, with the bio-inspired pulsating flow, the cell temperature drops 325.76K to 321.72K with an increase in flow rate from 0.5L/m to 2.5L/m. This means that the bio-inspired pulsating flow is more cooling efficient by 2.48% and 1.22% compared to uniform pulsating flow with C-design and parallel Wout-B design, respectively. The error bars along x-axis convey the level of uncertainty in the measured flow rates. This uncertainty can arise from factors such as meter calibration, flow disturbances, and measurement inaccuracies. Similarly, in the context of the temperature sensor. The error bars signify the potential deviation or variability in temperature readings due to factors such as sensor accuracy, calibration errors, and environmental conditions.



**Figure 4-45 Solar cell temperature conventional and parallel design without baffles experiment result.**

The experiment with uniform pulsating flow starts to decrease with an increase in flow rate from 1.5L/m to 2.5L/m. This keeps the cell average output power

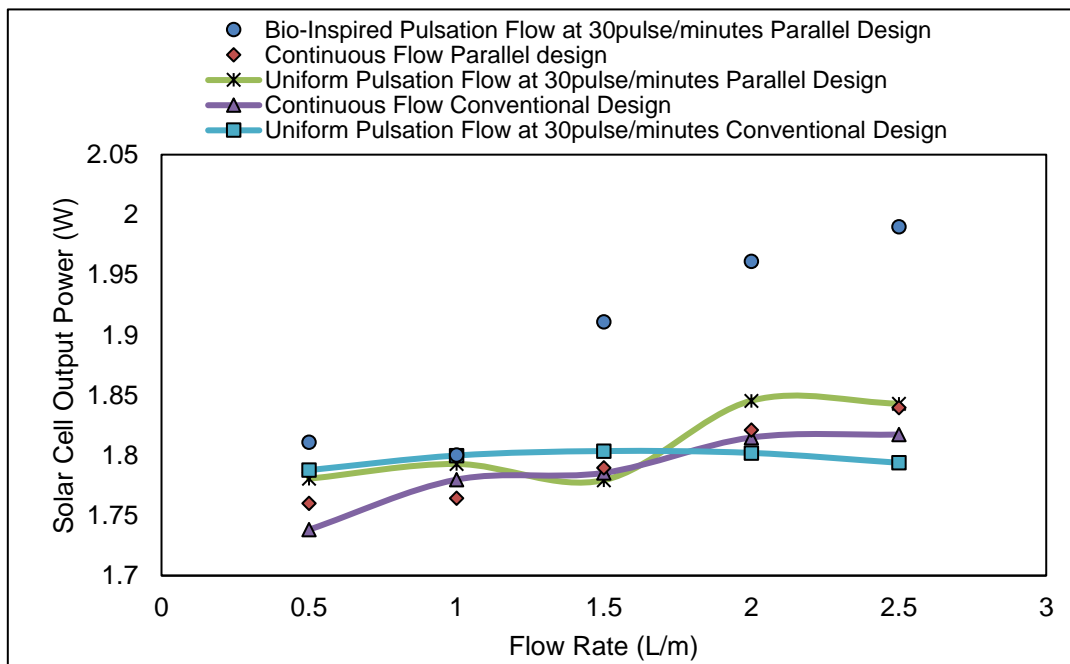
constant from 1.5L/m to 1.75L/m flow rate (Figure 4-47). The increase in cell temperature is due to extensive vibration experienced during the pulsating flow experiment approach adopted in this research. The vibration became more intense as the flow rate increased from 0.5-2.5L/m. In addition, between 1.5L/m to 2.5L/m, the vibration becomes intense, leading to cracks on the temperature sensor holders, as seen in Figure 4-46. That results in leakage and affects the pulsating flow's cooling capability during the experiment between 2L/m to 5L/m. The system's vibration has been highlighted as a challenge in applying pulsating flow [171,173]. This challenge was negligible with the parallel design of uniform pulsating flow and was not experienced with the bioinspired flow.



**Figure 4-46 Cracks on temperature sensor holder due to pulsating flow vibration of uniform pulsation at 30puls/minutes**

Figure 4-43 shows the solar cell output power versus flow rate, with an increase in flow rate from 0.5 to 2.5L/m, the solar cell power output increase for both continuous and pulsating flow, which agrees with [120]. The solar cell output power increase from 1.81W to 1.99W with bio-inspired cooling, 1.78W to 1.84W with parallel Wout-B design, and 1.78W to 1.79W with conventional design uniform pulsation flow, while 1.76W to 1.84W parallel Wout-B design and 1.74W to 1.81W C-design continuous flow. From 0.5-2.5L/m, the solar cell temperature decreased by 7.55% with 30pulse/minutes bio-Inspired pulsating flow compared to continuous flow using the parallel Wout-B design. In addition, the bio-Inspired pulsating flow was also more efficient by 7.39%, 8.68%, and 9.86% compared to parallel Wout-B design uniform pulsating flow, conventional design continuous

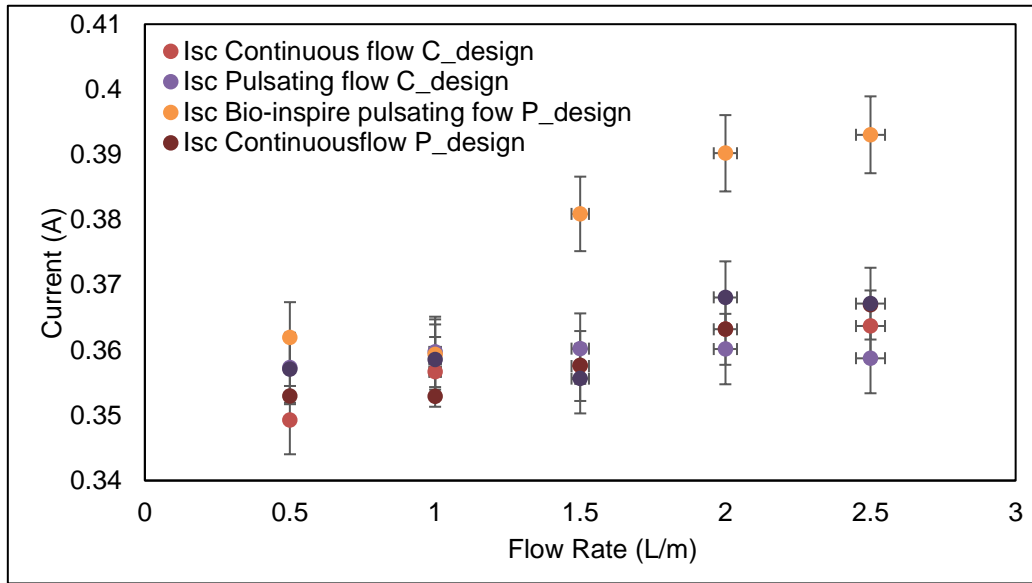
flow, and conventional design uniform pulsating flow, respectively. A 1.5% maximum cooling increase was recorded with uniform pulsating flow compared to continuous flow with the parallel Wout-B design. At the same time, a 2.67% maximum was obtained with parallel Wout-B design uniform pulsating flow compared to uniform pulsating flow C-design. The uniform pulsating flow C-design was 2.77% maximum efficient in cooling compared to C-design continuous flow.



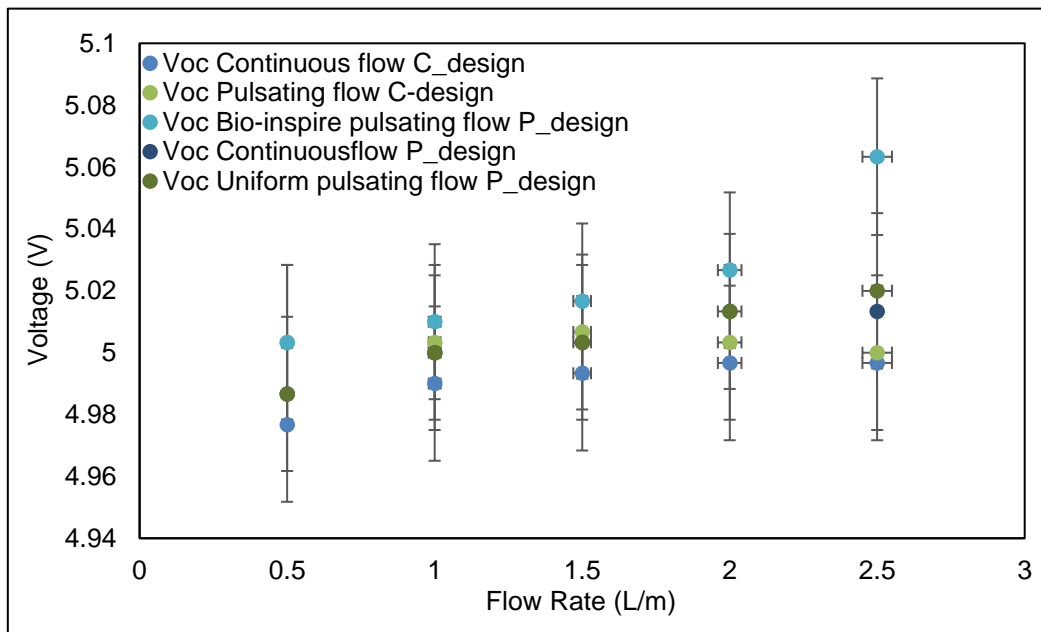
**Figure 4-47 Solar cell power output**

Figure 4-28 and Figure 4-29 shows the solar cell current and voltage versus flow rate, respectively. The error bars displayed in relation to the Multimeter readings indicate the level of uncertainty associated with these measurements. The error bars represent the potential deviation or variability in the measured values, considering factors such as the resolution and precision of the Multimeter, calibration errors, and possible environmental influences. The larger the error bars represent the uncertainty of the Multimeter, the greater the uncertainty in the recorded values, indicating a wider range of possible values. These error bars provide an indication of the range of values that could exist around the recorded data points. Furthermore, evaluating the uncertainties associated with Multimeter readings allows for an assessment of measurement accuracy and provides

insights into potential sources of error that may need to be addressed or minimized in future experimental setups. A maximum power point approach should be adapted not the Multimeter device. Another way could be connecting a load to the solar cell before measuring the current and voltages.



**Figure 4-48 Solar cell current versus flow rate**



**Figure 4-49 Solar cell voltage versus flow rate**

### 4.2.3 Error Analysis

The error analysis considers the measurement accuracy of the temperature logger, and the error of the flow sensor for each data point provided. Error analysis for each parameter as to be considered as follows:

1. Flow rate (L/min): The flow sensor has an error of 2%. Therefore, the maximum possible error in flow rate can be calculated as,

Maximum flow rate error = 2% of flow rate.

For each flow measurement the error can be calculated as:

Flow rate error = maximum flow rate error

2. Flow Rate (kg/s): Flow rate is given in l/min and must be converted to kg/s using the given conversion factor. The conversion factor is given as 1 l/min = 0.017 kg/s. To calculate the flow rate error (kg/s), we need to consider the flow rate error (l/min) and the conversion factor. The error can be calculated as

Flow rate error = Flow rate error (L/min) \* Conversion factor

The error analysis assumes that the errors are independent and randomly distributed. The calculated error for each of the data points are as follows, and the error has been reflected as error bars on the flow rate for each data:

Data point 1:

Flow rate error (l/min) = 2% of 2.5 = 0.05 l/min

Flow Error (kg/s) = 0.05 L/min \* 0.017 kg/s = 0.00085 kg/s

Data point 2:

Flow rate error (l/min) = 2% of 2 = 0.04 l/min

Flow Error (kg/s) = 0.04 L/min \* 0.017 kg/s = 0.00068 kg/s

Data point 3:

Flow rate error (l/min) = 2% of 1.5 = 0.03 l/min

Flow Error (kg/s) = 0.03 L/min \* 0.017 kg/s = 0.00051 kg/s

Data point 4:

Flow rate error (l/min) = 2% of 1 = 0.02 l/min

Flow Error (kg/s) = 0.02 L/min \* 0.017 kg/s = 0.00034 kg/s

Data point 5:

Flow rate error (l/min) = 2% of 0.5 = 0.01 l/min

Flow Error (kg/s) = 0.01 L/min \* 0.017 kg/s = 0.00017 kg/s

3. The measurement accuracy of the temperature logger is  $\pm 0.2\%$ . To calculate the error, we must consider the accuracy of the measurement as a percentage of the measured temperature.

Temperature error = (Measured temperature \* Measurement accuracy) / 100

The calculated error for each of the data points are as follows for the first set of data from the conventional design:

Data point 1:

Fluid inlet temperature error (K) =  $(296.0734 * 0.2) / 100 = 0.59$  K

Liquid outlet temperature error (K) =  $(297.4996 * 0.2) / 100 = 0.59$  K

Solar cell temperature error (K) =  $(329.9168 * 0.2) / 100 = 0.66$  K

Cooling pad temperature error (K) =  $(304.0738 * 0.2) / 100 = 0.61$  K

Data point 2:

Fluid inlet temperature error (K) =  $(296.4286 * 0.2) / 100 = 0.59$  K

Liquid outlet temperature error (K) =  $(298.1432 * 0.2) / 100 = 0.59$  K

Solar cell temperature error (K) =  $(328.9348 * 0.2) / 100 = 0.65$  K

Cooling pad temperature error (K) =  $(304.9088 * 0.2) / 100 = 0.61$  K

Data point 3:

Fluid inlet temperature error (K) =  $(296.6718 * 0.2) / 100 = 0.59$  K

Liquid outlet temperature error (K) =  $(298.6114 * 0.2) / 100 = 0.60$  K

Solar cell temperature error (K) =  $(328.7624 * 0.2) / 100 = 0.65$  K

Cooling pad temperature error (K) =  $(305.4294 * 0.2) / 100 = 0.61$  K

Data point 4:

Fluid inlet temperature error (K) =  $(296.8746 * 0.2) / 100 = 0.59$  K

Liquid outlet temperature error (K) =  $(299.108 * 0.2) / 100 = 0.59$  K

Solar cell temperature error (K) =  $(330.0638 * 0.2) / 100 = 0.66$  K

Cooling pad temperature error (K) =  $(305.8748 * 0.2) / 100 = 0.61$  K

Data point 5:

Fluid inlet temperature error (K) =  $(297.0572 * 0.2) / 100 = 0.59$  K

Liquid outlet temperature error (K) =  $(299.7244 * 0.2) / 100 = 0.60$  K

Solar cell temperature error (K) =  $(331.9864 * 0.2) / 100 = 0.66$  K

Cooling pad temperature error (K) =  $(306.48 * 0.2) / 100 = 0.61$  K

The same procedure was considered for each data to mitigate the errors. This has been reflected as error bars in the plot of temperature against flow rate for each component.

4. To perform the error analysis of the measurement taken with the Multimeter, we consider the accuracy specifications as highlighted in Appendix B, Table B7, which are  $\pm 1.5\%$  for DC current and  $\pm 0.5\%$  for DC voltage. Therefore, for a given data, the maximum potential error for each voltage ( $V_{oc}$ ) and current ( $I_{sc}$ ) measurement are  $V_{oc}$  [V] error =  $\pm 0.5\%$  of  $V_{oc}$  value, and  $I_{sc}$  [mA] error =  $\pm 1.5\%$  of  $I_{sc}$  value in all measurements.

To calculate the maximum potential error for each measurement for the first measurement of continuous flow:

*Voltage*

$V_{oc} = 4.97$  V,  $V_{oc}$  error =  $\pm 0.5\%$  of 4.97 =  $\pm 0.025$  V accurate in all data

*Current*

$I_{sc} = 348.2$  mA  $I_{sc}$  error =  $\pm 1.5\%$  of 348.2 =  $\pm 5.22$  mA accurate in all data

The error analysis assumes the maximum potential error based on the given accuracy specifications. Actual errors may be lower depending on the specific measurement values. The same calculations were applied to the rest of the measurements to determine the maximum potential errors for each voltage and current value in the data. This has been reflected as error bars in the plot of power against flow rate.

## 4.3 Validation

### 4.3.1 Conventional Validation

A further comparison between the simulation and experiment was conducted to obtain more validation. Figure 4-50 and Figure 4-51 show the pressure drops for both the continuous and pulsating flow, respectively; pressure drop was calculated using equation 3-10. With an increase in flow rate from 0.0085kg/s to 0.0425kg/s (0.5L/m to 2.5L/m), the pressure drops increase for simulation and experiment, respectively. This agrees with [120], where it was reported that an increase in flow rate pressure drop increase. It was observed that both simulation and experiments agree.

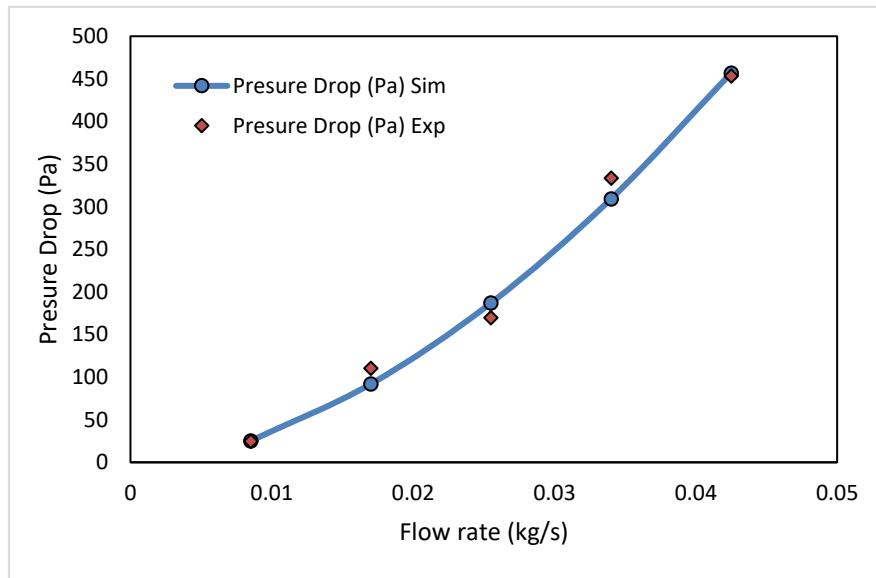
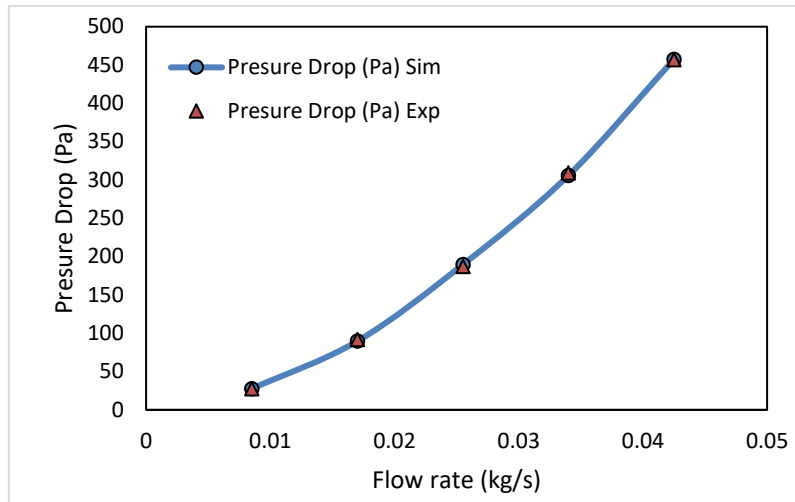


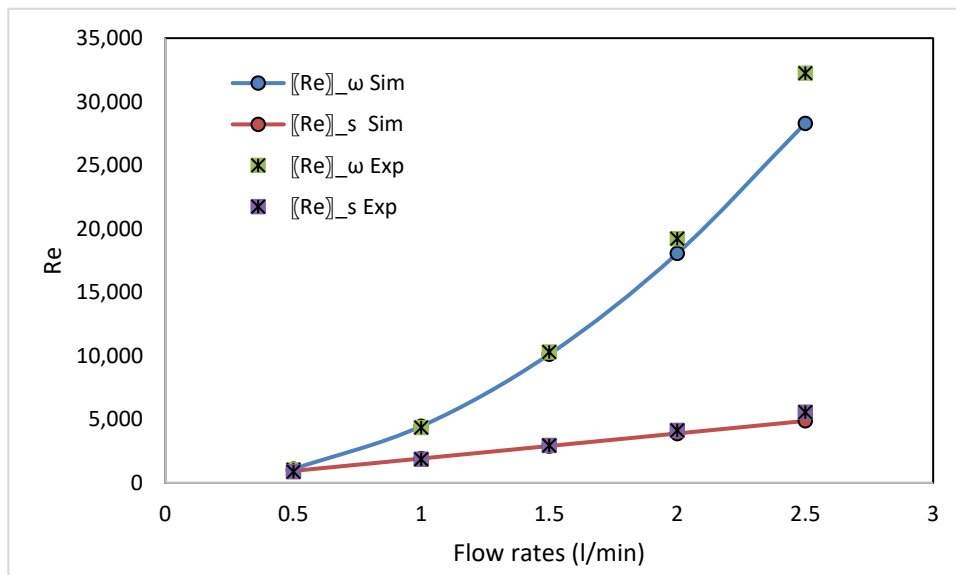
Figure 4-50 Pressure drops against flow rate continuous flow





**Figure 4-51 Pressure drops against flow rate pulsating flow**

Figure 4-52. Shows relationship flow rate versus oscillating Reynolds number ( $Re_{\omega}$ ) and stable components Reynolds number ( $Re_s$ ) for both simulation and experiment. In both cases, the Reynolds number increases with the flow rate increase. Research shows that an increase in flow rate increase Reynolds number [181,182]. The oscillating Reynolds number ( $Re_{\omega}$ ) is a function of the dimensionless amplitude of pulsation, while the stable components Reynolds number is a function of instantaneous pulsating velocity.



**Figure 4-52 Variations of flow rate versus Reynolds number**

### 4.3.2 Parallel Design Validation

Figure 4-53 and Figure 4-54 show the pressure drops for the experiment and simulation with continuous and pulsating flow, respectively. The pressure drop was calculated using equation 6, both simulation and experiments agree with an increase in flow rate from 0.5L/m to 2.5L/m. The resulting profile is consistent with the result reported in [120].

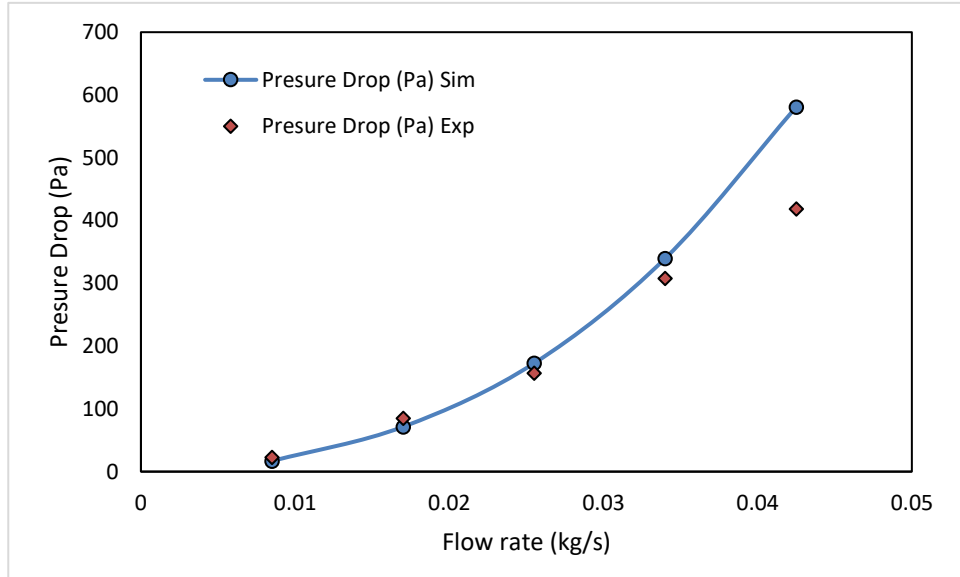


Figure 4-53 Pressure drops variation against flow rate continuous flow

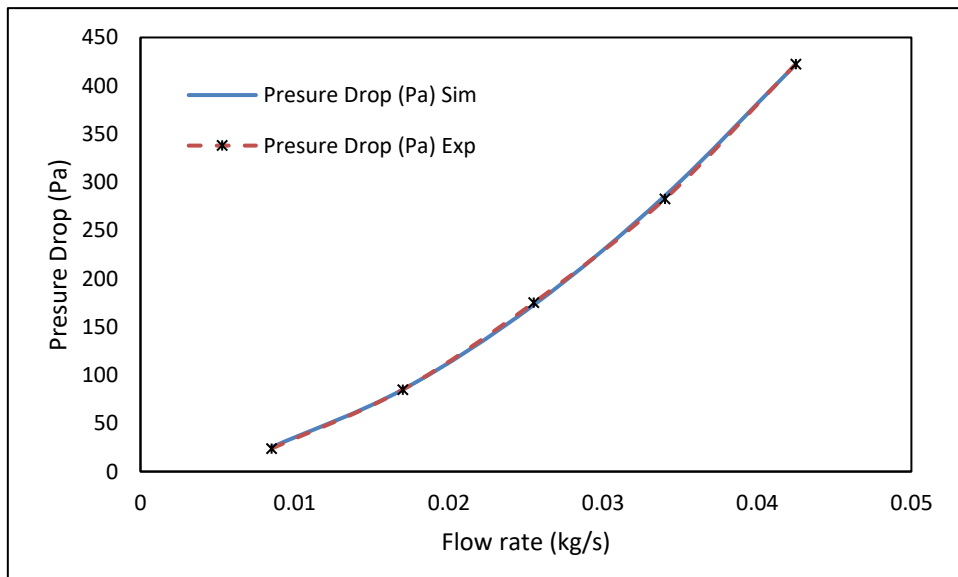
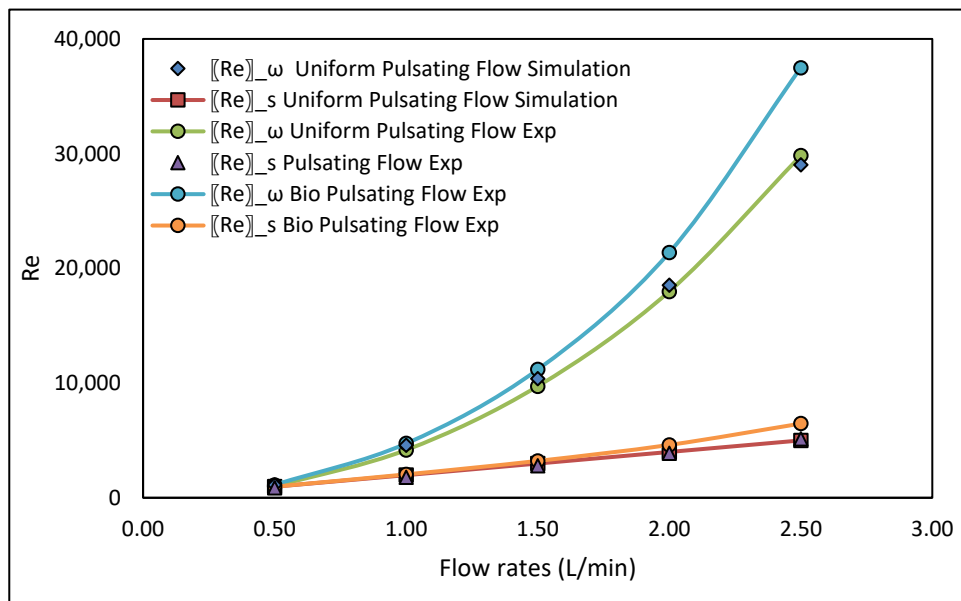


Figure 4-54 Pressure drops variation against flow rate pulsating flow

In both simulation and experiment, the connection between flow rate against oscillating Reynolds number ( $Re_\omega$ ) and stable components Reynolds number ( $Re_s$ ) is shown in Figure 4-55. An increase in flow rate increase the Reynolds numbers to rise as reported by [181, 182]. The stable components Reynolds number is a function of instantaneous pulsing velocity, while the oscillating Reynolds number depends on the dimensionless amplitude of the pulsation. Both simulation and experiment agree.



**Figure 4-55 Variations of flow rate versus Reynolds number**

## **5 CHAPTER FIVE**

### **5.1 Discussion, Future work, Recommendations and Conclusion**

#### **5.1.1 Discussion**

CPV cooling remains a challenging area of exploration for researchers. Multiple studies have highlighted the nonuniformity of concentrated solar cell temperatures, which lead to hot regions and cooled spots, necessitating further investigation. Generally, the current conventional cooling method relies on continuous flow, which increases the likelihood of nonuniform temperature distribution in CPV systems. Given the continuous changes in solar cell exposure to concentrated sunlight and the corresponding fluctuation in heat flux, there is a need for a more efficient CPV cooling approach that mitigates nonuniform temperature effects.

Despite the extensive research in this field, the application of bio-inspired cooling techniques, inspired by human thermoregulation, in a pulsating flow approach for CPV cooling has not been thoroughly studied. In this research, a similar approach utilizing control valves connected with Arduino was employed to regulate the pulsating flow. This offers researchers in the field of CPV cooling an opportunity to explore additional control parameters such as frequency, period, Womersley number, and Strouhal number to enhance cooling beyond just flow rate.

Implementing sensors in specific areas of the solar cell allows for targeted cooling, concentrating the coolant flow in regions with higher temperatures. This approach ensures that coolant is not wasted in areas where cooling is not required while effectively channelling it to areas that require cooling within the cell, thereby improving temperature uniformity. Moreover, this method reduces the amount of coolant used in CPV cooling, leading to enhanced performance as the coolant is utilized more efficiently in areas that require cooling the most, further enhancing uniformity.

Through the implementation of bio-inspired pulsating flow at a rate of 30 pulses per minute, the solar cell temperature was reduced by 1.96% compared to

continuous flow when utilizing the parallel Wout-B design. This reduction in temperature was observed across a flow rate range of 0.5 to 2.5 L/m. Furthermore, the bio-inspired pulsating flow outperformed uniform pulsating flow with the parallel Wout-B design, conventional design with continuous flow, and conventional design with uniform pulsating flow by 1.22%, 2.14%, and 4.00% in terms of cooling efficiency, respectively.

Comparing uniform pulsating flow to continuous flow using the parallel Wout-B design, a maximum cooling improvement of 0.74% was achieved. Additionally, when comparing uniform pulsating flow with the C-design with uniform pulsating flow parallel Wout-B design, a maximum improvement of 0.93% was observed. The C-design uniform pulsating flow was 1.90% more effective than the C-design continuous flow.

### **5.1.2 Future work and Recommendations**

Solar cells are recognized as one of the most significant sources of renewable energy due to their ability to directly convert sunlight into electricity. Consequently, concentrated solar cells (CPV) have garnered considerable attention in the literature surveyed in this research. The following recommendations, scale-up plans, and areas for future exploration are presented:

1. The current design employed in this research exhibits a thermal resistance of 0.039K/W, which is deemed excessive considering the size of the solar cell and the concentration area. Subsequent research should focus on reducing the thermal resistance by decreasing the thickness of the cooling pad cover from 10mm to 5mm or even lower. Reducing the distance between the concentrated solar cell and the cooling fluid passing through the cooling block enhances cooling efficiency.
2. Future research should explore different frequencies and periods using Computational Fluid Dynamics (CFD) to determine the optimum frequency and period for experimentation. The constant frequency of 0.5Hz and a period of 2s utilized in this study should serve as a starting point.

3. The parallel design with bio-inspired pulsating flow, which has demonstrated superior efficiency and exhibited no vibration in this research, should be employed. The use of uniform pulsation should be avoided as it is prone to vibration, which can adversely affect system stability and overall performance.
4. With a simulation set up of 200-time steps, 0.04s time step size (s) and 100 maximum iteration per time steps, the simulation time was approximately 3 days for every single trial) with 7cores processors PC. There was a challenge using Cranfield University high performance computer (HPC) to implement with the pulsating flow. Future work should consider limiting the simulation time by exploring how to employ pulsating simulation on HPC. The effect of simulation time on over all results can be studied to clearly understand the variation in the results comparison in Appendix E.
5. In CFD simulations, the use of the Shear Stress Transport (SST)  $k-\omega$  model is another method to explore. It has been reported to be more suitable for near-wall simulations than the  $k-\epsilon$  model employed in this research.
6. If the current high-flux sun simulator is utilized, the experiment should be conducted in a well-ventilated area to prevent sudden increases in ambient temperature due to prolonged concentration. The heat sinks dissipate heat from the cooling water, and their effectiveness is dependent on ambient temperature. Therefore, it is crucial to ensure that the heat sink is not compromised by ambient temperature fluctuations resulting from concentration.
7. Enhancing experimental accuracy can be achieved by placing a flow sensor at the inlet of each channel rather than using a collective flow sensor, as implemented in this research.
8. Exploring the use of nanofluids as coolants instead of water in conjunction with pulsating flow represents an area worth investigating. Previous

research has reported the advantages of utilizing nanofluids and ferrofluids, suggesting that solar cell cooling could be more efficient with their implementation.

9. Investigating CPV cooling integrated with Phase Change Materials (PCMs) or porous media in conjunction with pulsating flow is worthwhile. The effectiveness of cooling is influenced by environmental conditions surrounding the PCM and the positioning of the porous media along the channel.
10. Optimizing the position and number of baffles in the parallel design with baffles can enhance system effectiveness.
11. To improve the operational efficiency, a switch breaker should be utilized to connect the pump and solenoid valve. The current solenoid valve, which is off-to-closed, could be replaced with an off-to-open solenoid valve as an alternative solution.
12. Instead of relying solely on Multimeter readings, future research should consider adopting a Maximum Power Point approach for accurate measurement of solar cell performance. The MPP approach allows for determining the optimal operating conditions of the solar cell where maximum power output is achieved. By implementing this approach, researchers can obtain more precise and reliable measurements of voltage, current, and power output.
13. The economic aspect of introducing pulsating valves and electronic hardware to generate pulsating flow is another area of research to explore.

### **5.1.3 Conclusion**

The existing techniques employed for the cooling of concentrated photovoltaic (CPV) systems are predominantly based on continuous flow, which has been found to result in nonuniform temperature distribution issues across the solar cell. In light of this, the present review article puts forth an innovative approach centered around the utilization of pulsating flow for CPV cooling. The research

findings strongly support the viability of employing pulsating flow in the context of CPV cooling, aligning with the existing body of literature that underscores the superior cooling efficacy associated with pulsating flow as compared to the conventional continuous flow. The introduction of pulsating flow in CPV cooling not only addresses the aforementioned temperature nonuniformity concerns but also offers the potential for regulating additional parameters such as the frequency, period, and amplitude to optimise the cooling process, thus presenting promising avenues for future research and development.

The uniform pulsation approach implemented within the scope of this study demonstrates enhanced cooling performance in comparison to continuous flow. Conversely, bio-inspired cooling emerges as an even more effective cooling methodology when contrasted against uniform pulsation and continuous flow. Notably, the uniform pulsation approach is associated with significant vibrations during experimental operations, whereas the bio-inspired pulsation system experiences no such vibrations. This finding holds considerable significance for researchers exploring the realm of pulsating flow, as system vibrations have been recognized as a notable challenge encountered in pulsation flow studies. The integration of pulsating flow in CPV cooling thus presents a promising avenue for further advancements in the realm of cooling capability control and optimization within the context of CPV systems, warranting further investigation and exploration in future research pursuits.



## REFERENCES

1. Ankit., Sahoo SK., Sukchai S., Yanine FF. Review and comparative study of single-stage inverters for a PV system. *Renewable and Sustainable Energy Reviews*. Elsevier Ltd; 2018. pp. 962–986. Available at: DOI:10.1016/j.rser.2018.04.063 (Accessed: 19 May 2021)
2. Gul M., Kotak Y., Muneer T. Review on recent trend of solar photovoltaic technology. *Energy Exploration and Exploitation*. Multi-Science Publishing Co. Ltd; 1 July 2016; 34(4): 485–526. Available at: DOI:10.1177/0144598716650552 (Accessed: 26 May 2021)
3. Sharaf M., Huzayyin AS., Yousef MS. Performance enhancement of photovoltaic cells using phase change material (PCM) in winter. *Alexandria Engineering Journal*. 2022; 61(6). Available at: DOI:10.1016/j.aej.2021.09.044
4. Philipps SP., Bett AW. III-V Multi-junction solar cells and concentrating photovoltaic (CPV) systems. *Advanced Optical Technologies*. Walter de Gruyter GmbH; 2014. pp. 469–478. Available at: DOI:10.1515/aot-2014-0051
5. González M., Chan N., Ekins-Daukes NJ., Adams JGJ., Stavrinou P., Vurgaftman I., et al. Modeling and analysis of multijunction solar cells. *Physics and Simulation of Optoelectronic Devices XIX*. SPIE; 2011. p. 79330R. Available at: DOI:10.1117/12.875757
6. Rezk H., Hasaneen ES. A new MATLAB/Simulink model of triple-junction solar cell and MPPT based on artificial neural networks for photovoltaic energy systems. *Ain Shams Engineering Journal*. Ain Shams University; 2015. pp. 873–881. Available at: DOI:10.1016/j.asej.2015.03.001
7. Tan WC., Chong KK., Tan MH. Performance study of water-cooled multiple-channel heat sinks in the application of ultra-high concentrator photovoltaic system. *Solar Energy*. Elsevier Ltd; 2017; 147: 314–327. Available at: DOI:10.1016/j.solener.2017.03.040

8. Abo-Zahhad EM., Ookawara S., Radwan A., El-Shazly AH., ElKady MF. Thermal and structure analyses of high concentrator solar cell under confined jet impingement cooling. *Energy Conversion and Management*. Elsevier Ltd; 15 November 2018; 176: 39–54. Available at: DOI:10.1016/j.enconman.2018.09.005
9. Alzahrani M., Baig H., Shanks K., Mallick T. Estimation of the performance limits of a concentrator solar cell coupled with a micro heat sink based on a finite element simulation. *Applied Thermal Engineering*. Elsevier Ltd; 25 July 2020; 176. Available at: DOI:10.1016/j.applthermaleng.2020.115315
10. Du B., Hu E., Kolhe M. Performance analysis of water cooled concentrated photovoltaic (CPV) system. *Renewable and Sustainable Energy Reviews*. Elsevier Ltd; 2012. pp. 6732–6736. Available at: DOI:10.1016/j.rser.2012.09.007
11. Siefer G., Bett AW. Analysis of temperature coefficients for III-V multi-junction concentrator cells. *Progress in Photovoltaics: Research and Applications*. 2014; 22(5). Available at: DOI:10.1002/pip.2285
12. Babar M., Al-Ammar EA., Malik NH. Numerical Simulation Model of Multijunction Solar Cell Smart Integrated Energy Communities (Environmental pathways for sustainable energy services). View project Solar thermal energy View project. 2012. Available at: <https://www.researchgate.net/publication/233532728> (Accessed: 24 May 2021)
13. Azadinia M., Ameri M., Ghahrizjani RT., Fathollahi M. Maximizing the performance of single and multijunction MA and lead-free perovskite solar cell. *Materials Today Energy*. Elsevier Ltd; 1 June 2021; 20. Available at: DOI:10.1016/j.mtener.2021.100647 (Accessed: 30 July 2021)
14. Rauf S., Raza Kalair A., Khan N. Simulation design of multi-junction solar cell. *MedCeave Open access*. 2019; 3(1). Available at: DOI:10.15406/mojsp.2019.03.00031 (Accessed: 3 August 2021)
15. Saadah M., Hernandez E., Balandin AA. Thermal management of concentrated multi-junction solar cells with graphene-enhanced thermal interface materials.

Applied Sciences (Switzerland). MDPI AG; 7 June 2017; 7(6). Available at: DOI:10.3390/app7060589

16. Abo-Zahhad EM., Ookawara S., Radwan A., El-Shazly AH., El-Kady MF., Esmail MFC. Performance, limits, and thermal stress analysis of high concentrator multijunction solar cell under passive cooling conditions. *Applied Thermal Engineering*. Elsevier Ltd; 5 January 2020; 164. Available at: DOI:10.1016/j.applthermaleng.2019.114497 (Accessed: 6 August 2021)
17. Ogbomo OO., Amalu EH., Ekere NN., Olagbegi PO. A review of photovoltaic module technologies for increased performance in tropical climate. 2017. Available at: <https://www.sciencedirect.com/science/article/abs/pii/S1364032116308152?via%3Dihub> (Accessed: 19 May 2021)
18. Hadjida A., Bourahla M., Ertan Hb., Bekhti M. Analytical Modelling, Simulation and Comparative Study of Multi-Junction Solar Cells Efficiency. 2018; 8(4): 1824–1832. Available at: [https://www.researchgate.net/publication/330224747\\_Analytical\\_modelling\\_simulation\\_and\\_comparative\\_study\\_of\\_multi-junction\\_solar\\_cells\\_efficiency](https://www.researchgate.net/publication/330224747_Analytical_modelling_simulation_and_comparative_study_of_multi-junction_solar_cells_efficiency) (Accessed: 16 July 2021)
19. Awasthi A., Shukla AK., Murali Manohar SR., Dondariya C., Shukla KN., Porwal D., et al. Review on sun tracking technology in solar PV system. *Energy Reports*. Elsevier Ltd; 2020. pp. 392–404. Available at: DOI:10.1016/j.egy.2020.02.004 (Accessed: 20 July 2021)
20. Cui M., Chen N., Yang X., Wang Y., Bai Y., Zhang X. Thermal analysis and test for single concentrator solar cells. *Journal of Semiconductors*. 2009; 30(4). Available at: DOI:10.1088/1674-4926/30/4/044011
21. Bahaidarah HMS., Baloch AAB., Gandhidasan P. Uniform cooling of photovoltaic panels: A review. *Renewable and Sustainable Energy Reviews*. Elsevier Ltd; 2016. pp. 1520–1544. Available at: DOI:10.1016/j.rser.2015.12.064

22. Sharaf M., Yousef MS., Huzayyin AS. Review of cooling techniques used to enhance the efficiency of photovoltaic power systems. *Environmental Science and Pollution Research*. Springer Science and Business Media Deutschland GmbH; 2022. pp. 26131–26159. Available at: DOI:10.1007/s11356-022-18719-9
23. Xie WT., Dai YJ., Wang RZ., Sumathy K. Concentrated solar energy applications using Fresnel lenses: A review. *Renewable and Sustainable Energy Reviews*. August 2011; 15(6): 2488–2606. Available at: DOI:10.1016/j.rser.2011.03.031 (Accessed: 26 July 2021)
24. Abo-Zahhad EM., Ookawara S., Esmail MFC., El-Shazly AH., Elkady MF., Radwan A. Thermal management of high concentrator solar cell using new designs of stepwise varying width microchannel cooling scheme. *Applied Thermal Engineering*. Elsevier Ltd; 25 May 2020; 172. Available at: DOI:10.1016/j.applthermaleng.2020.115124
25. Ahmed A., Shanks K., Sundaram S., Mallick T. Energy and exergy analyses of new cooling schemes based on a serpentine configuration for a high concentrator photovoltaic system. *Applied Thermal Engineering*. Elsevier Ltd; 25 November 2021; 199. Available at: DOI:10.1016/j.applthermaleng.2021.117528
26. Xiao M., Tang L., Zhang X., Lun I., Yuan Y. A Review on Recent Development of Cooling Technologies for Concentrated Photovoltaics (CPV) Systems. *Energies*. MDPI AG; 6 December 2018; 11(12): 3416. Available at: DOI:10.3390/en11123416
27. Rawat P., Mehrotra S., Debbarma M., Sudhakar K. PERFORMANCE OF A SOLAR PANEL WITH WATER IMMERSION COOLING TECHNIQUE. 2014. Available at: [www.ijset.net](http://www.ijset.net)
28. Al-Amri F., Maatallah TS., Al-Amri OF., Ali S., Ali S., Ateeq IS., et al. Innovative technique for achieving uniform temperatures across solar panels using heat pipes and liquid immersion cooling in the harsh climate in the Kingdom of Saudi Arabia. *Alexandria Engineering Journal*. Elsevier B.V.; 1 February 2022; 61(2): 1413–1424. Available at: DOI:10.1016/j.aej.2021.06.046

29. Zhang J., Xuan Y. Performance improvement of a photovoltaic - Thermoelectric hybrid system subjected to fluctuant solar radiation. *Renewable Energy*. Elsevier Ltd; 2017; 113: 1551–1558. Available at: DOI:10.1016/j.renene.2017.07.003
30. Al-Nimr MA., Bukhari M., Mansour M. A combined CPV/T and ORC solar power generation system integrated with geothermal cooling and electrolyser/fuel cell storage unit. *Energy*. Elsevier Ltd; 2017; 133: 513–524. Available at: DOI:10.1016/j.energy.2017.05.142
31. Abdulmunem AR., Samin PM., Rahman HA., Hussien HA., Mazali II. Enhancing PV Cell's electrical efficiency using phase change material with copper foam matrix and multi-walled carbon nanotubes as passive cooling method. *Renewable Energy*. 2020; 160. Available at: DOI:10.1016/j.renene.2020.07.037
32. Nandurkar Y., Shrivastava RL., Soni VK. Improvement in Energy Efficiency of CPV Module by Way of various Active and Passive Cooling Techniques. *Journal of The Institution of Engineers (India): Series C*. 2022. Available at: DOI:10.1007/s40032-021-00765-w
33. Xu H., Wang N., Zhang C., Qu Z., Karimi F. Energy conversion performance of a PV/T-PCM system under different thermal regulation strategies. *Energy Conversion and Management*. 2021; 229. Available at: DOI:10.1016/j.enconman.2020.113660
34. Ranabhat K., Patrikeev L., Revina AA evna., Andrianov K., Lapshinsky V., Sofronova E. An introduction to solar cell technology. *Journal of Applied Engineering Science*. 2016; 14(4). Available at: DOI:10.5937/jaes14-10879
35. Aghenta LO., Iqbal MT. Development of an IoT Based Open Source SCADA System for PV System Monitoring. 2019 IEEE Canadian Conference of Electrical and Computer Engineering, CCECE 2019. 2019. Available at: DOI:10.1109/CCECE.2019.8861827
36. Singh BP., Goyal SK., Kumar P. Solar pv cell materials and technologies: Analyzing the recent developments. *Materials Today: Proceedings*. 2021. Available at: DOI:10.1016/j.matpr.2021.01.003

37. Mallick TK., Eames PC., Norton B. Using air flow to alleviate temperature elevation in solar cells within asymmetric compound parabolic concentrators. *Solar Energy*. 2007; 81(2). Available at: DOI:10.1016/j.solener.2006.04.003
38. Hersch P., Zweibel K., Energy Research Institute S. *Basic Photovoltaic Principles and Methods*. 1982. Available at: [https://www.google.com/url?sa=t&rct=j&q=&esrc=s&source=web&cd=&cad=rja&uact=8&ved=2ahUKEwjss7vXiufwAhVsC2MBHUOwAMsQFnoECAUQAA&url=https%3A%2F%2Fwww.nrel.gov%2Fdocs%2Flegosti%2Fold%2F1448.pdf&usg=AOvVaw0EI4XZ5eygNHH8qggtqEZ\\_](https://www.google.com/url?sa=t&rct=j&q=&esrc=s&source=web&cd=&cad=rja&uact=8&ved=2ahUKEwjss7vXiufwAhVsC2MBHUOwAMsQFnoECAUQAA&url=https%3A%2F%2Fwww.nrel.gov%2Fdocs%2Flegosti%2Fold%2F1448.pdf&usg=AOvVaw0EI4XZ5eygNHH8qggtqEZ_) (Accessed: 22 May 2021)
39. Nayan MF., Ullah SMS., Saif SN. Comparative analysis of PV module efficiency for different types of silicon materials considering the effects of environmental parameters. 2016 3rd International Conference on Electrical Engineering and Information and Communication Technology, iCEEICT 2016. Institute of Electrical and Electronics Engineers Inc.; 2017. Available at: DOI:10.1109/CEEICT.2016.7873089
40. Wilson GM., Al-Jassim M., Metzger WK., Glunz SW., Verlinden P., Xiong G., et al. The 2020 photovoltaic technologies roadmap. *Journal of Physics D: Applied Physics*. IOP Publishing Ltd; 2020. Available at: DOI:10.1088/1361-6463/ab9c6a
41. Itten R., Stucki M. Highly efficient 3rd generation multi-junction solar cells using silicon heterojunction and perovskite tandem: Prospective life cycle environmental impacts. *Energies*. 2017; 10(7). Available at: DOI:10.3390/en10070841
42. Ibrahim KA., Kim M., Kinuthia D., Hussaini ZA., Crawley F., Luo Z. High Performance Green Hydrogen Generation System. 2021 IEEE 20th International Conference on Micro and Nanotechnology for Power Generation and Energy Conversion Applications, PowerMEMS 2021. 2021. Available at: DOI:10.1109/PowerMEMS54003.2021.9658399
43. Wang S., Shi J., Chen HH., Schafer SR., Munir M., Stecker G., et al. Cooling design and evaluation for photovoltaic cells within constrained space in a

- CPV/CSP hybrid solar system. *Applied Thermal Engineering*. 2017; 110. Available at: DOI:10.1016/j.applthermaleng.2016.08.196
44. Royne A., Dey CJ., Mills DR. Cooling of photovoltaic cells under concentrated illumination: A critical review. *Solar Energy Materials and Solar Cells*. 2005; 86(4). Available at: DOI:10.1016/j.solmat.2004.09.003
  45. Tonui JK., Tripanagnostopoulos Y. Air-cooled PV/T solar collectors with low cost performance improvements. *Solar Energy*. 2007; 81(4). Available at: DOI:10.1016/j.solener.2006.08.002
  46. Radziemska E. Performance analysis of a photovoltaic-thermal integrated system. *International Journal of Photoenergy*. 2009; 2009. Available at: DOI:10.1155/2009/732093
  47. Anand S., Senthil Kumar M., Balasubramanian KR., Ajith Krishnan R., Maheswari L. An experimental study on thermal management of concentrated photovoltaic cell using loop heat pipe and heat sink. *Heat Transfer - Asian Research*. 2019; 48(6). Available at: DOI:10.1002/htj.21504
  48. Theristis M., Sarmah N., Mallick TK., O'Donovan TS. Design and numerical analysis of enhanced cooling techniques for a high concentration photovoltaic (HCPV) system. 27th European Photovoltaic Solar Energy Conference and Exhibition. 2012;
  49. Anderson WG., Dussinger PM., Sarraf DB., Tamanna S. Heat pipe cooling of concentrating photovoltaic cells. Conference Record of the IEEE Photovoltaic Specialists Conference. 2008. Available at: DOI:10.1109/PVSC.2008.4922577
  50. Faghri A. HEAT PIPES: REVIEW, OPPORTUNITIES AND CHALLENGES. *Frontiers in Heat Pipes*. 20 April 2014; 5(1). Available at: DOI:10.5098/fhp.5.1
  51. Zhang Y., Faghri A. Advances and unsolved issues in pulsating heat pipes. *Heat Transfer Engineering*. January 2008; 29(1): 20–44. Available at: DOI:10.1080/01457630701677114

52. Yousefi T., Mousavi SA., Farahbakhsh B., Saghir MZ. Experimental investigation on the performance of CPU coolers: Effect of heat pipe inclination angle and the use of nanofluids. *Microelectronics Reliability*. 2013; 53(12). Available at: DOI:10.1016/j.microrel.2013.06.012
53. Zhu K., Zheng M., Wang B., Dai B., Wang Y., Wei J., et al. Experimental Study of Energy Saving Performances in Chip Cooling by using Heat Sink with Embedded Heat Pipe. *Energy Procedia*. 2017. Available at: DOI:10.1016/j.egypro.2017.03.1046
54. Li J., Li X., Zhou G., Liu Y. Development and evaluation of a supersized aluminum flat plate heat pipe for natural cooling of high power telecommunication equipment. *Applied Thermal Engineering*. 2021; 184. Available at: DOI:10.1016/j.applthermaleng.2020.116278
55. Behi H., Behi M., Karimi D., Jaguemont J., Ghanbarpour M., Behnia M., et al. Heat pipe air-cooled thermal management system for lithium-ion batteries: High power applications. *Applied Thermal Engineering*. 2021; 183. Available at: DOI:10.1016/j.applthermaleng.2020.116240
56. He Z., Xi H., Ding T., Wang J., Li Z. Energy efficiency optimization of an integrated heat pipe cooling system in data center based on genetic algorithm. *Applied Thermal Engineering*. 2021; 182. Available at: DOI:10.1016/j.applthermaleng.2020.115800
57. Huang HJ., Shen SC., Shaw HJ. Design and fabrication of a novel hybrid-structure heat pipe for a concentrator photovoltaic. *Energies*. 2012; 5(11). Available at: DOI:10.3390/en5114340
58. Lee D il., Baek SW. Development of a heating system using CPV technology and heat pipes. *Environmental Progress & Sustainable Energy*. 8 July 2015; 34(4): 1197–1207. Available at: DOI:10.1002/ep.12082
59. Shittu S., Li G., Zhao X., Akhlaghi YG., Ma X., Yu M. Comparative study of a concentrated photovoltaic-thermoelectric system with and without flat plate heat



- pipe. *Energy Conversion and Management*. 2019; 193. Available at: DOI:10.1016/j.enconman.2019.04.055
60. Lee D il., Baek SW. Development of hybrid device for photovoltaic power generation and heating. *Transactions of the Korean Society of Mechanical Engineers, B*. 2014; 38(11). Available at: DOI:10.3795/KSME-B.2014.38.11.907
  61. Alizadeh H., Ghasempour R., Shafii MB., Ahmadi MH., Yan WM., Nazari MA. Numerical simulation of PV cooling by using single turn pulsating heat pipe. *International Journal of Heat and Mass Transfer*. 2018; 127. Available at: DOI:10.1016/j.ijheatmasstransfer.2018.06.108
  62. Gilmore N., Timchenko V., Menictas C. Microchannel cooling of concentrator photovoltaics: A review. *Renewable and Sustainable Energy Reviews*. 2018. Available at: DOI:10.1016/j.rser.2018.04.010
  63. Said Z., Allagui A., Abdelkareem MA., Alawadhi H., Elsaid K. Acid-functionalized carbon nanofibers for high stability, thermoelectrical and electrochemical properties of nanofluids. *Journal of Colloid and Interface Science*. 2018; 520. Available at: DOI:10.1016/j.jcis.2018.02.042
  64. Alirezaie A., Hajmohammad MH., Alipour A., salari M. Do nanofluids affect the future of heat transfer?“A benchmark study on the efficiency of nanofluids”. *Energy*. 2018; 157. Available at: DOI:10.1016/j.energy.2018.05.060
  65. Gupta M., Singh V., Kumar S., Kumar S., Dilbaghi N., Said Z. Up to date review on the synthesis and thermophysical properties of hybrid nanofluids. *Journal of Cleaner Production*. 2018. Available at: DOI:10.1016/j.jclepro.2018.04.146
  66. Sharaf OZ., Taylor RA., Abu-Nada E. On the colloidal and chemical stability of solar nanofluids: From nanoscale interactions to recent advances. *Physics Reports*. 2020. Available at: DOI:10.1016/j.physrep.2020.04.005
  67. Javed S., Ali HM., Babar H., Khan MS., Janjua MM., Bashir MA. Internal convective heat transfer of nanofluids in different flow regimes: A comprehensive review. *Physica A: Statistical Mechanics and its Applications*. 2020. Available at: DOI:10.1016/j.physa.2019.122783

68. Said Z., Hachicha AA., Aberoumand S., Yousef BAA., Sayed ET., Bellos E. Recent advances on nanofluids for low to medium temperature solar collectors: energy, exergy, economic analysis and environmental impact. *Progress in Energy and Combustion Science*. 2021. Available at: DOI:10.1016/j.pecs.2020.100898
69. Cotfas DT., Mahmoudinezhad S., Rezanian A., Cotfas PA., Rosendahl L. Effect of Phase Change Material on Performance of Hybrid Photovoltaic-Thermoelectric System under Low Concentration Ratio. 2021 International Aegean Conference on Electrical Machines and Power Electronics, ACEMP 2021 and 2021 International Conference on Optimization of Electrical and Electronic Equipment, OPTIM 2021. Institute of Electrical and Electronics Engineers Inc.; 2021. pp. 1–7. Available at: DOI:10.1109/OPTIM-ACEMP50812.2021.9590022
70. Maatallah T., Zachariah R., Al-Amri FG. Exergo-economic analysis of a serpentine flow type water based photovoltaic thermal system with phase change material (PVT-PCM/water). *Solar Energy*. 2019; 193. Available at: DOI:10.1016/j.solener.2019.09.063
71. Chávez-Urbiola EA., Vorobiev Y v., Bulat LP. Solar hybrid systems with thermoelectric generators. *Solar Energy*. 2012; 86(1). Available at: DOI:10.1016/j.solener.2011.10.020
72. Yousef MS., Hassan H. Energetic and exergetic performance assessment of the inclusion of phase change materials (PCM) in a solar distillation system. *Energy Conversion and Management*. 2019; 179. Available at: DOI:10.1016/j.enconman.2018.10.078
73. Yousef MS., Hassan H. An experimental work on the performance of single slope solar still incorporated with latent heat storage system in hot climate conditions. *Journal of Cleaner Production*. 2019; 209. Available at: DOI:10.1016/j.jclepro.2018.11.120
74. Yousef MS., Hassan H. Energy payback time, exergoeconomic and enviroeconomic analyses of using thermal energy storage system with a solar

- desalination system: An experimental study. *Journal of Cleaner Production*. 2020; 270. Available at: DOI:10.1016/j.jclepro.2020.122082
75. Pause B. Phase change materials and their application in coatings and laminates for textiles. *Smart Textile Coatings and Laminates*. 2018. Available at: DOI:10.1016/B978-0-08-102428-7.00008-0
  76. Mohamed SA., Al-Sulaiman FA., Ibrahim NI., Zahir MH., Al-Ahmed A., Saidur R., et al. A review on current status and challenges of inorganic phase change materials for thermal energy storage systems. *Renewable and Sustainable Energy Reviews*. 2017. Available at: DOI:10.1016/j.rser.2016.12.012
  77. Nomura T., Sheng N., Zhu C., Saito G., Hanzaki D., Hiraki T., et al. Microencapsulated phase change materials with high heat capacity and high cyclic durability for high-temperature thermal energy storage and transportation. *Applied Energy*. 2017; 188. Available at: DOI:10.1016/j.apenergy.2016.11.025
  78. Senthilkumar M., Balasubramanian KR., Kottala RK., Sivapirakasam SP., Maheswari L. Characterization of form-stable phase-change material for solar photovoltaic cooling. *Journal of Thermal Analysis and Calorimetry*. Springer Science+Business Media B.V.; 1 September 2020; 141(6): 2487–2496. Available at: DOI:10.1007/s10973-020-09521-1
  79. Hasan A., McCormack SJ., Huang MJ., Norton B. Evaluation of phase change materials for thermal regulation enhancement of building integrated photovoltaics. *Solar Energy*. September 2010; 84(9): 1601–1612. Available at: DOI:10.1016/j.solener.2010.06.010
  80. Huang MJ., Eames PC., Norton B., Hewitt NJ. Natural convection in an internally finned phase change material heat sink for the thermal management of photovoltaics. *Solar Energy Materials and Solar Cells*. 2011; 95(7). Available at: DOI:10.1016/j.solmat.2011.01.008
  81. Nada SA., El-Nagar DH., Hussein HMS. Improving the thermal regulation and efficiency enhancement of PCM-Integrated PV modules using nano particles.

Energy Conversion and Management. 2018; 166. Available at: DOI:10.1016/j.enconman.2018.04.035

82. Xu Y., Chen M., Ning X., Chen X., Sun Z., Ma Y., et al. Influences of coupling agent on thermal properties, flammability and mechanical properties of polypropylene/thermoplastic polyurethanes composites filled with expanded graphite. *Journal of Thermal Analysis and Calorimetry*. 2014; 115(1). Available at: DOI:10.1007/s10973-013-3243-8
83. Zhang N., Yuan Y., Cao X., Du Y., Zhang Z., Gui Y. Latent Heat Thermal Energy Storage Systems with Solid–Liquid Phase Change Materials: A Review. *Advanced Engineering Materials*. 2018. Available at: DOI:10.1002/adem.201700753
84. Pang S., Tsao HN., Feng X., Mullen K. Patterned graphene electrodes from solution-processed graphite oxide films for organic field-effect transistors. *Advanced Materials*. 2009; 21(34). Available at: DOI:10.1002/adma.200803812
85. Jesumathy S., Udayakumar M., Suresh S. Experimental study of enhanced heat transfer by addition of CuO nanoparticle. *Heat and Mass Transfer/Waerme- und Stoffuebertragung*. 2012; 48(6). Available at: DOI:10.1007/s00231-011-0945-y
86. Shastry DMC., Arunachala UC. Thermal management of photovoltaic module with metal matrix embedded PCM. *Journal of Energy Storage*. 2020; 28. Available at: DOI:10.1016/j.est.2020.101312
87. Lee DY., Vafai K. Comparative analysis of jet impingement and microchannel cooling for high heat flux applications. *International Journal of Heat and Mass Transfer*. 1999; 42(9). Available at: DOI:10.1016/S0017-9310(98)00265-8
88. Liu YH., Song SJ., Lo YH. Jet impingement heat transfer on target surfaces with longitudinal and transverse grooves. *International Journal of Heat and Mass Transfer*. 2013; 58(1–2). Available at: DOI:10.1016/j.ijheatmasstransfer.2012.11.042

89. Rattner AS. General Characterization of Jet Impingement Array Heat Sinks with Interspersed Fluid Extraction Ports for Uniform High-Flux Cooling. *Journal of Heat Transfer*. 2017; 139(8). Available at: DOI:10.1115/1.4036090
90. Barrau J., Perona A., Dollet A., Rosell J. Outdoor test of a hybrid jet impingement/micro-channel cooling device for densely packed concentrated photovoltaic cells. *Solar Energy*. Elsevier Ltd; 2014; 107: 113–121. Available at: DOI:10.1016/j.solener.2014.05.040
91. Hasan HA., Sopian K., Jaaz AH., Al-Shamani AN. Experimental investigation of jet array nanofluids impingement in photovoltaic/thermal collector. *Solar Energy*. 2017; 144. Available at: DOI:10.1016/j.solener.2017.01.036
92. Awad M., Radwan A., Abdelrehim O., Emam M., Shmroukh AN., Ahmed M. Performance evaluation of concentrator photovoltaic systems integrated with a new jet impingement-microchannel heat sink and heat spreader. *Solar Energy*. 2020; 199. Available at: DOI:10.1016/j.solener.2020.02.078
93. Ewe WE., Fudholi A., Sopian K., Asim N. Modeling of bifacial photovoltaic-thermal (PVT) air heater with jet plate. *International Journal of Heat and Technology*. 2021; 39(4). Available at: DOI:10.18280/ijht.390409
94. Liu L., Zhu L., Wang Y., Huang Q., Sun Y., Yin Z. Heat dissipation performance of silicon solar cells by direct dielectric liquid immersion under intensified illuminations. *Solar Energy*. 2011; 85(5). Available at: DOI:10.1016/j.solener.2011.02.007
95. Wang Y., Fang Z., Zhu L., Huang Q., Zhang Y., Zhang Z. The performance of silicon solar cells operated in liquids. *Applied Energy*. 2009; 86(7–8). Available at: DOI:10.1016/j.apenergy.2008.08.020
96. Mehrotra S., Rawat P., Debbarma M., Sudhakar K. Performance of a solar panel with water immersion cooling technique. *Int J Sci Environ Technol*. 2014; 3(3): 1161–1172.
97. Chinamhora T., Cheng G., Tham Y., Irshad W. PV Panel Cooling System for Malaysia Climate Conditions Porous material View project thin film View project.

Proceedings of the international conference on energy and sustainability. Karachi, Pakistan. 2013. Available at: <https://www.researchgate.net/publication/332668789>

98. Zhu L., Boehm RF., Wang Y., Halford C., Sun Y. Water immersion cooling of PV cells in a high concentration system. *Solar Energy Materials and Solar Cells*. 2011; 95(2). Available at: DOI:10.1016/j.solmat.2010.08.037
99. Rosa-Clot M., Rosa-Clot P., Tina GM., Scandura PF. Submerged photovoltaic solar panel: SP2. *Renewable Energy*. 2010; 35(8). Available at: DOI:10.1016/j.renene.2009.10.023
100. Han X., Wang Y., Zhu L. Electrical and thermal performance of silicon concentrator solar cells immersed in dielectric liquids. *Applied Energy*. 2011; 88(12). Available at: DOI:10.1016/j.apenergy.2011.05.037
101. Sun Y., Wang Y., Zhu L., Yin B., Xiang H., Huang Q. Direct liquid-immersion cooling of concentrator silicon solar cells in a linear concentrating photovoltaic receiver. *Energy*. Elsevier Ltd; 1 February 2014; 65: 264–271. Available at: DOI:10.1016/j.energy.2013.11.063
102. Han X., Wang Y., Zhu L. The performance and long-term stability of silicon concentrator solar cells immersed in dielectric liquids. *Energy Conversion and Management*. 2013; 66. Available at: DOI:10.1016/j.enconman.2012.10.009
103. Xin G., Wang Y., Sun Y., Huang Q., Zhu L. Experimental study of liquid-immersion III-V multi-junction solar cells with dimethyl silicon oil under high concentrations. *Energy Conversion and Management*. 2015; 94. Available at: DOI:10.1016/j.enconman.2015.01.063
104. Kang X., Wang Y., Huang Q., Cui Y., Shi X., Sun Y. Study on direct-contact phase-change liquid immersion cooling dense-array solar cells under high concentration ratios. *Energy Conversion and Management*. 2016; 128. Available at: DOI:10.1016/j.enconman.2016.09.073
105. Saxena A., Deshmukh S., Nirali S., Wani S. Laboratory based Experimental Investigation of Photovoltaic (PV) Thermo-control with Water and its Proposed

Real-time Implementation. *Renewable Energy*. 2018; 115. Available at: DOI:10.1016/j.renene.2017.08.029

106. Dadsetani R., Sheikhzadeh GA., Hajmohammadi MR., Safaei MR. Introduce a novel configuration of microchannel and high-conductivity inserts for cooling of disc-shaped electronic components. *International Journal of Numerical Methods for Heat and Fluid Flow*. 2020; 30(6). Available at: DOI:10.1108/HFF-02-2019-0105
107. Alugoju UK., Dubey SK., Javed A. Optimization of converging and diverging microchannel heat sink for electronic chip cooling. *IEEE Transactions on Components, Packaging and Manufacturing Technology*. 2020; 10(5). Available at: DOI:10.1109/TCPMT.2020.2985402
108. Fábregas J., Santamaría H., Buelvas E., Saulpérez., Díaz C., Carpintero J., et al. COMPUTATIONAL FLUID DYNAMICS MODELING OF MICROCHANNELS COOLING FOR ELECTRONIC MICRODEVICES. *IIUM Engineering Journal*. 2022; 23(1). Available at: DOI:10.31436/IIUMEJ.V23I1.2113
109. Sohail Murshed SM., Nieto de Castro CA. A critical review of traditional and emerging techniques and fluids for electronics cooling. *Renewable and Sustainable Energy Reviews*. 2017. Available at: DOI:10.1016/j.rser.2017.04.112
110. Meral ZK., Parlak N. EXPERIMENTAL RESEARCH AND CFD SIMULATION OF CROSS FLOW MICROCHANNEL HEAT EXCHANGER. *Journal of Thermal Engineering*. 2021; 7(2). Available at: DOI:10.18186/THERMAL.872366
111. Huang B., Li H., Xu T. Experimental investigation of the flow and heat transfer characteristics in microchannel heat exchangers with reentrant cavities. *Micromachines*. 2020; 11(4). Available at: DOI:10.3390/M11040403
112. Tiwari R., Andhare RS., Shooshtari A., Ohadi M. Development of an additive manufacturing-enabled compact manifold microchannel heat exchanger. *Applied Thermal Engineering*. January 2019; 147: 781–788. Available at: DOI:10.1016/j.applthermaleng.2018.10.122

113. Reddy KS., Lokeswaran S., Agarwal P., Mallick TK. Numerical investigation of micro-channel based active module cooling for solar CPV system. *Energy Procedia*. 2014. Available at: DOI:10.1016/j.egypro.2014.07.283
114. Radwan A., Ookawara S., Ahmed M. Analysis and simulation of concentrating photovoltaic systems with a microchannel heat sink. *Solar Energy*. 2016; 136. Available at: DOI:10.1016/j.solener.2016.06.070
115. Shittu S., Li G., Zhao X., Zhou J., Ma X., Akhlaghi YG. Experimental study and exergy analysis of photovoltaic-thermoelectric with flat plate micro-channel heat pipe. *Energy Conversion and Management*. 2020; 207. Available at: DOI:10.1016/j.enconman.2020.112515
116. Khan MG., Fartaj A. A review on microchannel heat exchangers and potential applications. *International Journal of Energy Research*. 2011. Available at: DOI:10.1002/er.1720
117. Hasan MI., Rageb AA., Yaghoubi M., Homayoni H. Influence of channel geometry on the performance of a counter flow microchannel heat exchanger. *International Journal of Thermal Sciences*. August 2009; 48(8): 1607–1618. Available at: DOI:10.1016/j.ijthermalsci.2009.01.004
118. Mokrani O., Bourouga B., Castelain C., Peerhossaini H. Fluid flow and convective heat transfer in flat microchannels. *International Journal of Heat and Mass Transfer*. 2009; 52(5–6). Available at: DOI:10.1016/j.ijheatmasstransfer.2008.08.022
119. Soliman AMA., Hassan H. Effect of heat spreader size, microchannel configuration and nanoparticles on the performance of PV-heat spreader-microchannels system. *Solar Energy*. 2019; 182. Available at: DOI:10.1016/j.solener.2019.02.059
120. Yang K., Zuo C. A novel multi-layer manifold microchannel cooling system for concentrating photovoltaic cells. *Energy Conversion and Management*. 2015; 89. Available at: DOI:10.1016/j.enconman.2014.09.046



121. Islam K., Riggs B., Ji Y., Robertson J., Spitler C., Romanin V., et al. Transmissive microfluidic active cooling for concentrator photovoltaics. *Applied Energy*. 2019; 236. Available at: DOI:10.1016/j.apenergy.2018.12.027
122. Siyabi I al., Khanna S., Sundaram S., Mallick T. Experimental and numerical thermal analysis of multi-layered microchannel heat sink for concentrating photovoltaic application. *Energies*. 2019; 12(1). Available at: DOI:10.3390/en12010122
123. Rozsas G., Bogнар G., Takacs G., Szabo PG., Plesz B. Process and measurement of electroplated back-contact integrated microchannel cooling devices for CPV cells. 2020 26th International Workshop on Thermal Investigations of ICs and Systems, THERMINIC 2020 - Proceedings. 2020. Available at: DOI:10.1109/THERMINIC49743.2020.9420517
124. Zhang H., Yan S., Wang T., Wu Y., Zhao X., Zhao N. Enhanced Heat Transfer of Carbon Nanotube Nanofluid Microchannels Applied on Cooling Gallium Arsenide Cell. *Journal of Thermal Science*. 2020; 29(6). Available at: DOI:10.1007/s11630-020-1303-5
125. Farahani SD., Alibeigi M., Zakinia A., Goodarzi M. The effect of microchannel-porous media and nanofluid on temperature and performance of CPV system. *Journal of Thermal Analysis and Calorimetry*. 2021; Available at: DOI:10.1007/s10973-021-11087-5
126. Elqady Hl., Radwan A., Ali AYM., Rabie M., Abo-Zahhad EM., Ookawara S., et al. Concentrator photovoltaic thermal management using a new design of double-layer microchannel heat sink. *Solar Energy*. 2021; 220. Available at: DOI:10.1016/j.solener.2021.02.003
127. Yu H., Zhuang J., Li T., Li W., He T., Mao N. Influence of transient heat flux on boiling flow pattern in a straight microchannel applied in concentrator photovoltaic systems. *International Journal of Heat and Mass Transfer*. 2022; 190. Available at: DOI:10.1016/j.ijheatmasstransfer.2022.122792

128. Rupp ME., Heermann J., Uphoff ME. Need for a reliable system to measure body temperature. *American Journal of Infection Control*. 2004. Available at: DOI:10.1016/j.ajic.2003.06.005
129. Childs C. Body temperature and clinical thermometry. *Handbook of Clinical Neurology*. 2018. Available at: DOI:10.1016/B978-0-444-64074-1.00029-X
130. Lim CL., Byrne C., Lee JKW. Human thermoregulation and measurement of body temperature in exercise and clinical settings. *Annals of the Academy of Medicine Singapore*. 2008.
131. Gisolfi C., Robinson S. Relations between physical training, acclimatization, and heat tolerance. *Journal of applied physiology*. 1969; 26(5). Available at: DOI:10.1152/jappl.1969.26.5.530
132. Romanovsky AA. Skin temperature: Its role in thermoregulation. *Acta Physiologica*. 2014. Available at: DOI:10.1111/apha.12231
133. Fiala D., Havenith G., Bröde P., Kampmann B., Jendritzky G. UTCI-Fiala multi-node model of human heat transfer and temperature regulation. *International Journal of Biometeorology*. Springer New York LLC; 19 April 2012; 56(3): 429–441. Available at: DOI:10.1007/S00484-011-0424-7/TABLES/4 (Accessed: 28 May 2022)
134. Fiala D., Psikuta A., Jendritzky G., Paulke S., Nelson DA., van Marken Lichtenbelt WD., et al. Physiological modeling for technical, clinical and research applications. *Frontiers in Bioscience - Scholar*. 2010; 2 S(3). Available at: DOI:10.2741/s112
135. Katic K., Zeiler W., Boxem G. Thermophysiological models: A first comparison. Fifth German-Austrian IBPSA Conference, At RWTH Aachen University, Aachen, Germany. 2014.
136. Lai D., Chen Q. A two-dimensional model for calculating heat transfer in the human body in a transient and non-uniform thermal environment. *Energy and Buildings*. 2016; 118. Available at: DOI:10.1016/j.enbuild.2016.02.051

137. Dang SN., Xue HJ., Zhang XY., Qu J., Zhong CW., Chen SY. Three-dimensional human thermoregulation model based on pulsatile blood flow and heating mechanism. *Chinese Physics B*. 2018; 27(11). Available at: DOI:10.1088/1674-1056/27/11/114402
138. Binney N. The function of the heart is not obvious. *Studies in History and Philosophy of Science Part C :Studies in History and Philosophy of Biological and Biomedical Sciences*. 2018; 68–69. Available at: DOI:10.1016/j.shpsc.2018.05.003
139. Akdag U., Akcay S., Demiral D. Heat transfer enhancement with laminar pulsating nanofluid flow in a wavy channel. *International Communications in Heat and Mass Transfer*. 2014; 59. Available at: DOI:10.1016/j.icheatmasstransfer.2014.10.008
140. Naphon P., Wiriyasart S. Experimental study on laminar pulsating flow and heat transfer of nanofluids in micro-fins tube with magnetic fields. *International Journal of Heat and Mass Transfer*. 2018; 118. Available at: DOI:10.1016/j.ijheatmasstransfer.2017.10.131
141. Kim SY., Kang BH., Hyun JM. Heat transfer from pulsating flow in a channel filled with porous media. *International Journal of Heat and Mass Transfer*. 1994; 37(14). Available at: DOI:10.1016/0017-9310(94)90304-2
142. Huang X., Li P., Tan Y. Time-dependent heat transfer analysis of ellipsoidal protruded microchannel with multiple pulsating jets. *Applied Thermal Engineering*. 2022; 210. Available at: DOI:10.1016/j.applthermaleng.2022.118348
143. Zhang L., Tian L., Zhang A., Chen H. Effects of the shape of tube and flow field on fluid flow and heat transfer. *International Communications in Heat and Mass Transfer*. 2020; 117. Available at: DOI:10.1016/j.icheatmasstransfer.2020.104782
144. Ye Q., Zhang Y., Wei J. A comprehensive review of pulsating flow on heat transfer enhancement. *Applied Thermal Engineering*. 2021; 196. Available at: DOI:10.1016/j.applthermaleng.2021.117275

145. Navickaitė K., Mocerino A., Cattani L., Bozzoli F., Bahl C., Liltrop K., et al. Enhanced heat transfer in tubes based on vascular heat exchangers in fish: Experimental investigation. *International Journal of Heat and Mass Transfer*. 2019; 137. Available at: DOI:10.1016/j.ijheatmasstransfer.2019.03.067
146. Akachi Hisateru. US 4921041 A - Structure of a heat pipe . 1990. Available at: <https://www.lens.org/lens/patent/151-789-425-811-172/frontpage> (Accessed: 29 May 2022)
147. Nikolayev VS. Physical principles and state-of-the-art of modeling of the pulsating heat pipe: A review. *Applied Thermal Engineering*. Pergamon; 1 August 2021; 195: 117111. Available at: DOI:10.1016/j.applthermaleng.2021.117111 (Accessed: 29 May 2022)
148. Zhang Y., Faghri A. Advances and Unsolved Issues in Pulsating Heat Pipes. *Heat Transfer Engineering*. 14 January 2008; 29(1): 20–44. Available at: DOI:10.1080/01457630701677114
149. Khandekar S., Dollinger N., Groll M. Understanding operational regimes of closed loop pulsating heat pipes: an experimental study. *Applied Thermal Engineering*. April 2003; 23(6): 707–719. Available at: DOI:10.1016/S1359-4311(02)00237-5
150. Khandekar S., Groll M. On the Definition of Pulsating Heat Pipes: An overview. *Proc. 5th Minsk International Seminar (Heat Pipes, Heat Pumps and Refrigerators)*. 2003; 3.
151. Liu X., Sun Q., Zhang C., Wu L. High-speed visual analysis of fluid flow and heat transfer in oscillating heat pipes with different diameters. *Applied Sciences (Switzerland)*. 2016; 6(11). Available at: DOI:10.3390/app6110321
152. Kim J., Kim SJ. Experimental investigation on working fluid selection in a micro pulsating heat pipe. *Energy Conversion and Management*. 2020; 205. Available at: DOI:10.1016/j.enconman.2019.112462
153. Kim W., Kim SJ. Effect of reentrant cavities on the thermal performance of a pulsating heat pipe. *Applied Thermal Engineering*. 2018; 133. Available at: DOI:10.1016/j.applthermaleng.2018.01.027

154. Kim W., Kim SJ. Effect of a flow behavior on the thermal performance of closed-loop and closed-end pulsating heat pipes. *International Journal of Heat and Mass Transfer*. 2020; 149. Available at: DOI:10.1016/j.ijheatmasstransfer.2019.119251
155. Youn YJ., Kim SJ. Fabrication and evaluation of a silicon-based micro pulsating heat spreader. *Sensors and Actuators, A: Physical*. 2012; 174(1). Available at: DOI:10.1016/j.sna.2011.12.006
156. Skullong S., Promvong P., Thianpong C., Pimsarn M. Heat transfer and turbulent flow friction in a round tube with staggered-winglet perforated-tapes. *International Journal of Heat and Mass Transfer*. 2016; 95. Available at: DOI:10.1016/j.ijheatmasstransfer.2015.12.007
157. Singh S., Singh SK., Mali HS., Dayal R. Numerical investigation of heat transfer in structured rough microchannels subjected to pulsed flow. *Applied Thermal Engineering*. 2021; 197. Available at: DOI:10.1016/j.applthermaleng.2021.117361
158. Elshafei EAM., Safwat Mohamed M., Mansour H., Sakr M. Experimental study of heat transfer in pulsating turbulent flow in a pipe. *International Journal of Heat and Fluid Flow*. 2008; 29(4). Available at: DOI:10.1016/j.ijheatfluidflow.2008.03.018
159. Hemmat Esfe M., Bahiraei M., Torabi A., Valadkhani M. A critical review on pulsating flow in conventional fluids and nanofluids: Thermo-hydraulic characteristics. *International Communications in Heat and Mass Transfer*. 2021; 120. Available at: DOI:10.1016/j.icheatmasstransfer.2020.104859
160. Yellin EL. Laminar-turbulent transition process in pulsatile flow. *Circulation research*. 1966; 19(4). Available at: DOI:10.1161/01.RES.19.4.791
161. Khandekar S., Charoensawan P., Groll M., Terdtoon P. Closed loop pulsating heat pipes - Part B: Visualization and semi-empirical modeling. *Applied Thermal Engineering*. 2003; 23(16). Available at: DOI:10.1016/S1359-4311(03)00168-6
162. Tan L., Yuan Y., Huang C. CFD modelling on flow field characteristics of engine cooling water jacket and its cooling performance improvement based on coolant

transport path analysis method. Proceedings of the Institution of Mechanical Engineers, Part A: Journal of Power and Energy. SAGE Publications Ltd; 2022; Available at: DOI:10.1177/09576509221116503

163. Altaç Z., Mahir N. A comparative assessment of turbulent forced convection heat transfer from a single cylinder using RANS and les models. *Isi Bilimi Ve Teknigi Dergisi/ Journal of Thermal Science and Technology*. 2018; 38(1).
164. Afroz F., Sharif MAR. Numerical investigation of heat transfer from a plane surface due to turbulent annular swirling jet impingement. *International Journal of Thermal Sciences*. 2020; 151. Available at: DOI:10.1016/j.ijthermalsci.2019.106257
165. Montorfano D., Gaetano A., Barbato MC., Ambrosetti G., Pedretti A. CPV cells cooling system based on submerged jet impingement: CFD modeling and experimental validation. *AIP Conference Proceedings*. 2014. Available at: DOI:10.1063/1.4897046
166. Lee SS., Lai SO., Chong KK. A study on cooling of concentrator photovoltaic cells using CFD. *ICIMTR 2012 - 2012 International Conference on Innovation, Management and Technology Research*. 2012. Available at: DOI:10.1109/ICIMTR.2012.6236427
167. al Siyabi I., Shanks K., Mallick T., Sundaram S. Indoor and outdoor characterization of concentrating photovoltaic attached to multi-layered microchannel heat sink. *Solar Energy*. Elsevier Ltd; 15 May 2020; 202: 55–72. Available at: DOI:10.1016/j.solener.2020.03.101
168. Siyabi I al., Khanna S., Sundaram S., Mallick T. Experimental and numerical thermal analysis of multi-layered microchannel heat sink for concentrating photovoltaic application. *Energies*. MDPI AG; 1 January 2019; 12(1). Available at: DOI:10.3390/en12010122
169. Jiang PX., Fan MH., Si GS., Ren ZP. Thermal-hydraulic performance of small scale micro-channel and porous-media heat-exchangers. *International Journal of*

Heat and Mass Transfer. 2001; 44(5). Available at: DOI:10.1016/S0017-9310(00)00169-1

170. Olayiwola BO., Schaldach G., Walzel P. IMECE 2010-38596 CFD SIMULATIONS OF FLOW AND HEAT TRANSFER IN A ZIGZAG CHANNEL WITH FLOW PULSATION. Available at: [http://asmedigitalcollection.asme.org/IMECE/proceedings-pdf/IMECE2010/44441/1531/2710150/1531\\_1.pdf](http://asmedigitalcollection.asme.org/IMECE/proceedings-pdf/IMECE2010/44441/1531/2710150/1531_1.pdf)
171. Ye Q., Zhang Y., Wei J. A comprehensive review of pulsating flow on heat transfer enhancement. Applied Thermal Engineering. Elsevier Ltd; 1 September 2021; 196. Available at: DOI:10.1016/j.applthermaleng.2021.117275
172. Wang X., Zhang N. Numerical analysis of heat transfer in pulsating turbulent flow in a pipe. International Journal of Heat and Mass Transfer. September 2005; 48(19–20): 3957–3970. Available at: DOI:10.1016/j.ijheatmasstransfer.2005.04.011
173. Kurtulmuş N., Sahin B. Experimental investigation of pulsating flow structures and heat transfer characteristics in sinusoidal channels. International Journal of Mechanical Sciences. Elsevier Ltd; 1 February 2020; 167. Available at: DOI:10.1016/j.ijmecsci.2019.105268
174. Ahmed HE., Ahmed MI., Seder IMF., Salman BH. Experimental investigation for sequential triangular double-layered microchannel heat sink with nanofluids. International Communications in Heat and Mass Transfer. Elsevier Ltd; 1 October 2016; 77: 104–115. Available at: DOI:10.1016/j.icheatmasstransfer.2016.06.010
175. Haibullina A., Khairullin A., Balzamov D., Ilyin V., Bronskaya V., Khairullina L. Local Heat Transfer Dynamics in the In-Line Tube Bundle under Asymmetrical Pulsating Flow. Energies. MDPI; 1 August 2022; 15(15). Available at: DOI:10.3390/en15155571
176. Bayomy AM., Saghir MZ. Heat transfer characteristics of aluminum metal foam subjected to a pulsating/steady water flow: Experimental and numerical

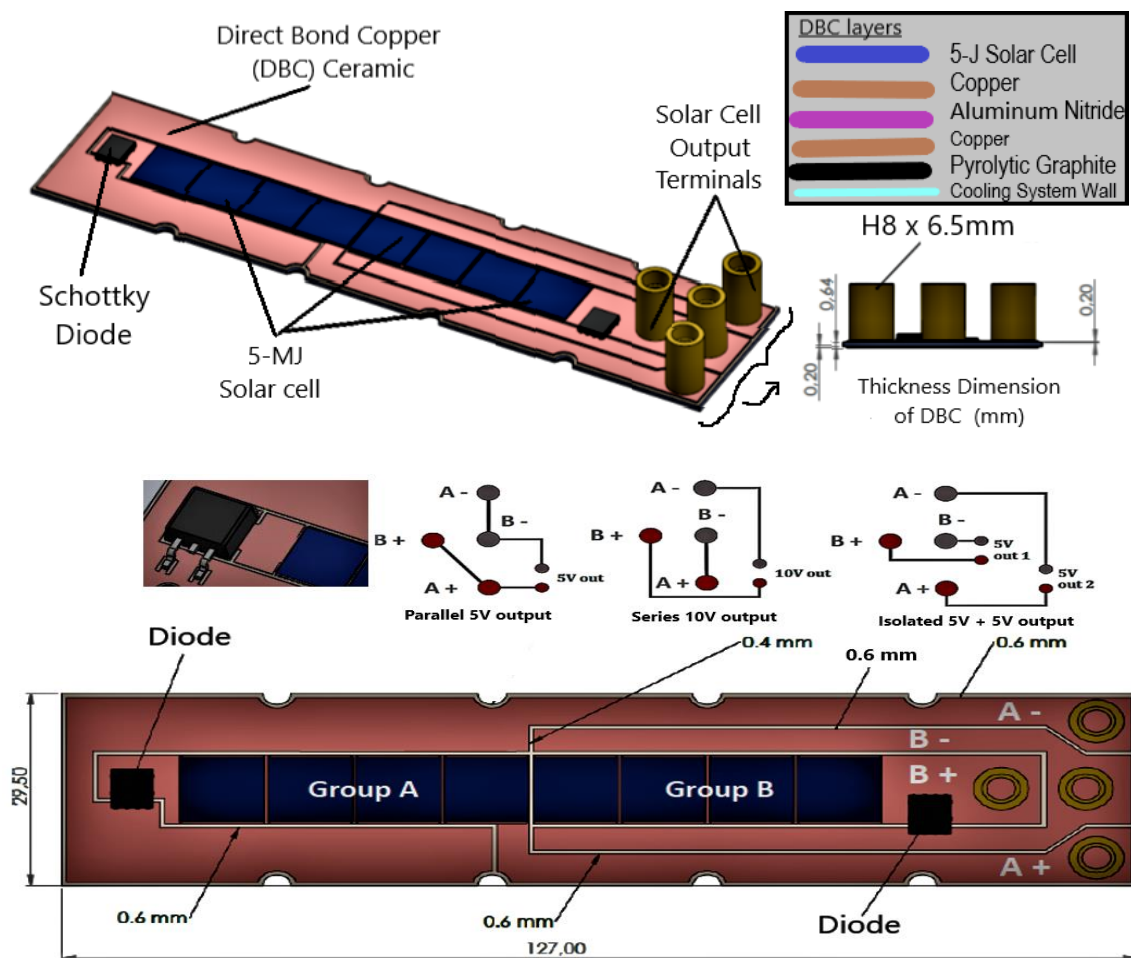
approach. *International Journal of Heat and Mass Transfer*. 2016; 97. Available at: DOI:10.1016/j.ijheatmasstransfer.2016.02.009

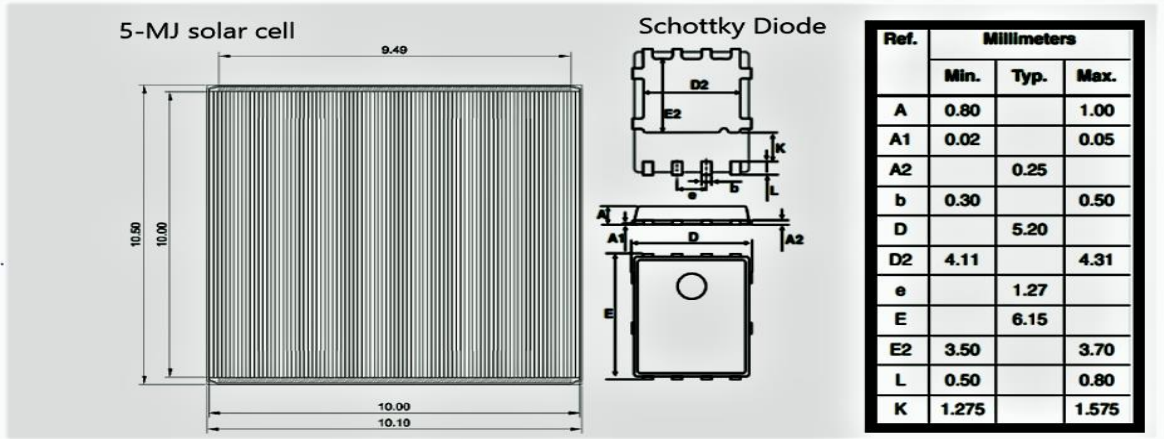
177. Siyabi I al., Khanna S., Sundaram S., Mallick T. Experimental and numerical thermal analysis of multi-layered microchannel heat sink for concentrating photovoltaic application. *Energies*. 2019; 12(1). Available at: DOI:10.3390/en12010122
178. Khanna S., Sharma V. Explicit Analytical Expression for Solar Flux Distribution on an Undelected Absorber Tube of Parabolic Trough Concentrator Considering Sun-Shape and Optical Errors. *Journal of Solar Energy Engineering, Transactions of the ASME*. 2016; 138(1). Available at: DOI:10.1115/1.4032122
179. Ansari D., Kim KY. Performance analysis of double-layer microchannel heat sinks under non-uniform heating conditions with random hotspots. *Micromachines*. 2017; 8(2). Available at: DOI:10.3390/mi8020054
180. Chamkha AJ., Selimefendigil F. Forced convection of pulsating nanofluid flow over a backward facing step with various particle shapes. *Energies*. 2018; 11(11). Available at: DOI:10.3390/en11113068
181. Gao X., Zhang Y., Hu Z., Huang Y. Numerical investigation on the influence of surface flow direction on the heat transfer characteristics in a granite single fracture. *Applied Sciences (Switzerland)*. 2021; 11(2). Available at: DOI:10.3390/app11020751
182. Anusha G. KPS. Heat Transfer Analysis of Gasketed Plate Heat Exchanger. *International Journal For Technological Research In Engineering*. 2016; 5(9).
183. Al-Sumaily GF., Thompson MC. Forced convection from a circular cylinder in pulsating flow with and without the presence of porous media. *International Journal of Heat and Mass Transfer*. 2013; 61(1). Available at: DOI:10.1016/j.ijheatmasstransfer.2013.01.067



## Appendix A Specification of Multijunction Solar cell

The multijunction solar cell has 8 cells arranged and wired on a DBC in groups A and B, with 4 cells on each. The total active area of the cell is about 830mm<sup>2</sup> (10mm x 83mm) having a wiring of 5V, 10V and 5V+5V connections with four pots A+, A-, B+ and B-.





## Appendix B Components Specifications

### B.1 Solenoids Valve

Voltage	12V DC
Maximum operation temperature	+60°C
Minimum operation temperature	-20°C
Maximum working pressure	10 bars
Thread size	1/8in
Number of ports	2
Default valve position	NC
Operation	Direct

### B.2 Control Valve

Connection port thread	G 1/8
Maximum flow rate	7.8 L/min
Body material	Steel
Seal material	Nitrile rubber
Thread size	1/8in
Maximum operation temperature	+100°C
Minimum operation temperature	-20°C

### B.3 Arduino

Microcontroller	ATmega2560
Operating voltage	5 V
Input voltage (recommended)	7-12 V
Input voltage (limits)	6-20 V
Digital I/O pins	54 (of which 14 provide PWM output)
Analog input pins	16
DC current per I/O pin	40 mA
DC current for 3.3 V pin	50 mA
Flash memory	256 KB of which 8 KB used by bootloader
SRAM	8 KB
EEPROM	4 KB
Clock Speed	16 MHz

#### B.4 Water Flow Sensor

Model Number	FS200A
Working flow rate	0.5-30 L/min
Error	2%
Maximum water pressure	1.2 MPa
Maximum operation temperature	+100°C
Minimum operation temperature	0°C
Thread size	1/2in

#### B.5 Temperature Logger

Number of Input Channels	8
Sensor Type	B, E, J, K, N, R, S, T
Interface Type	USB
Data Logger Type	Temperature
Maximum Temperature Measurement	+1200 (J) °C, +1300 (N) °C, +1370 (K) °C, +1760 (S) °C, +1820 (B) °C, +400 (T) °C, +910 (E) °C
Power Source	USB
Best Temperature Measurement Accuracy	±0.2%
Model Number	USB TC-08
Alarm	Yes
Includes	Software
Temperature Measurement Resolution	0.025°C

## B.6 Thermocouple

Probe Thermocouple type	K
For Use With	Pico Technology TC-08 Thermocouple Data Logger
Moulded flat	pin mini plug
Cable length	1m (3ft)
Probe diameter	1.5 mm
Probe material	Stainless steel
Maximum temperature sensed	+350 °C
Minimum temperature sensed	-60°C

## B.7 Handheld Digital Multimeter

Attribute	Value
Multimeter Type	Handheld
True RMS	Yes
Functions Measured	AC Current, AC Voltage, Continuity, DC Current, DC Voltage, Diode, Resistance

Absolute Maximum DC Voltage Measurement	600V dc
Absolute Maximum Resistance Measurement	2M $\Omega$
Absolute Maximum DC Current Measurement	10A dc
Absolute Maximum AC Voltage Measurement	600V ac
Absolute Maximum AC Current Measurement	10A ac
Dimensions	67 x 46 x 120mm
Length	67mm
Width	46mm
Best AC Current Accuracy	$\pm 2\%$
Best DC Current Accuracy	$\pm 1.5\%$
Best AC Voltage Accuracy	$\pm 1\%$
Best DC Voltage Accuracy	$\pm 0.5\%$
Best Resistance Measurement Accuracy	$\pm 1\%$
Safety Category Voltage	600V
Battery Type	1.5 V AAA

## Appendix C Pulsating Programme Arduino Code

## Code-Bio-Inspired\_and\_Uniform\_Pulsation | Arduino 1.8.18

File Edit Sketch Tools Help

```
Code-Bio-Inspired_and_Uniform_Pulsation §
/*Uniform and Bio-Inspired Pulsating Flow Programme*/
/*Definition of pins for the solenoids*/
    int Pin_solenoid_1= 2;
    int Pin_solenoid_2= 3;
    int Pin_solenoid_3= 4;
    int Pin_solenoid_4= 5;
    int Pin_solenoid_5= 6;

#define ONE_WIRE_BUS 8
int toggle1;

OneWire oneWire(ONE_WIRE_BUS);

DallasTemperature sensors(&oneWire);

void setup() {

/*Define the pins for the flow sensor*/
    pinMode(Pin_solenoid_1, OUTPUT);
    pinMode(Pin_solenoid_2, OUTPUT);
    pinMode(Pin_solenoid_3, OUTPUT);
    pinMode(Pin_solenoid_4, OUTPUT);
    pinMode(Pin_solenoid_5, OUTPUT);

    Serial.begin(9600);
    noInterrupts();
//set timer1 interrupt at 1Hz
    TCCR1A = 0;// set entire TCCR1A register to 0
    TCCR1B = 0;// same for TCCR1B
    TCNT1 = 0;//initialize counter value to 0
    // set compare match register for 1hz increments
    OCR1A = 15624;// = (16*10^6) / (1*1024) - 1 (must be <65536)
    // turn on CTC mode
    TCCR1B |= (1 << WGM12);
    // Set CS12 and CS10 bits for 1024 prescaler
    TCCR1B |= (1 << CS12) | (1 << CS10);
```



```

Code-Bio-Inspired_and_Uniform_Pulsation $
TCCR1B |= (1 << WGM12);
// Set CS12 and CS10 bits for 1024 prescaler
TCCR1B |= (1 << CS12) | (1 << CS10);
// enable timer compare interrupt
TIMSK1 |= (1 << OCIE1A);
interrupts();
}
void loop (){
}
ISR(TIMER1_COMPA_vect){//timer1 interrupt 1Hz toggles pin 13 (LED)
//generates pulse wave of frequency 1Hz/2 = 0.5Hz (takes two cycles for full wave- toggle high then toggle low)
// For Continuous flow Set all valves open (i.e HIGH) by setting digitalWrite 'if toggle' valve open (HIGH),
//   and all the digitalWrite 'else toggle1'close (HIGH)
// For uniform pulsating flow set all the digitalWrite 'if toggle' valve open (HIGH),
//   and all the digitalWrite 'else toggle1'close (LOW)>
//For Bio-Inspired pulsating flow set two digitalWrite 'if toggle' valve open (HIGH),
//   and the other two digitalWrite 'else toggle1'close (LOW)

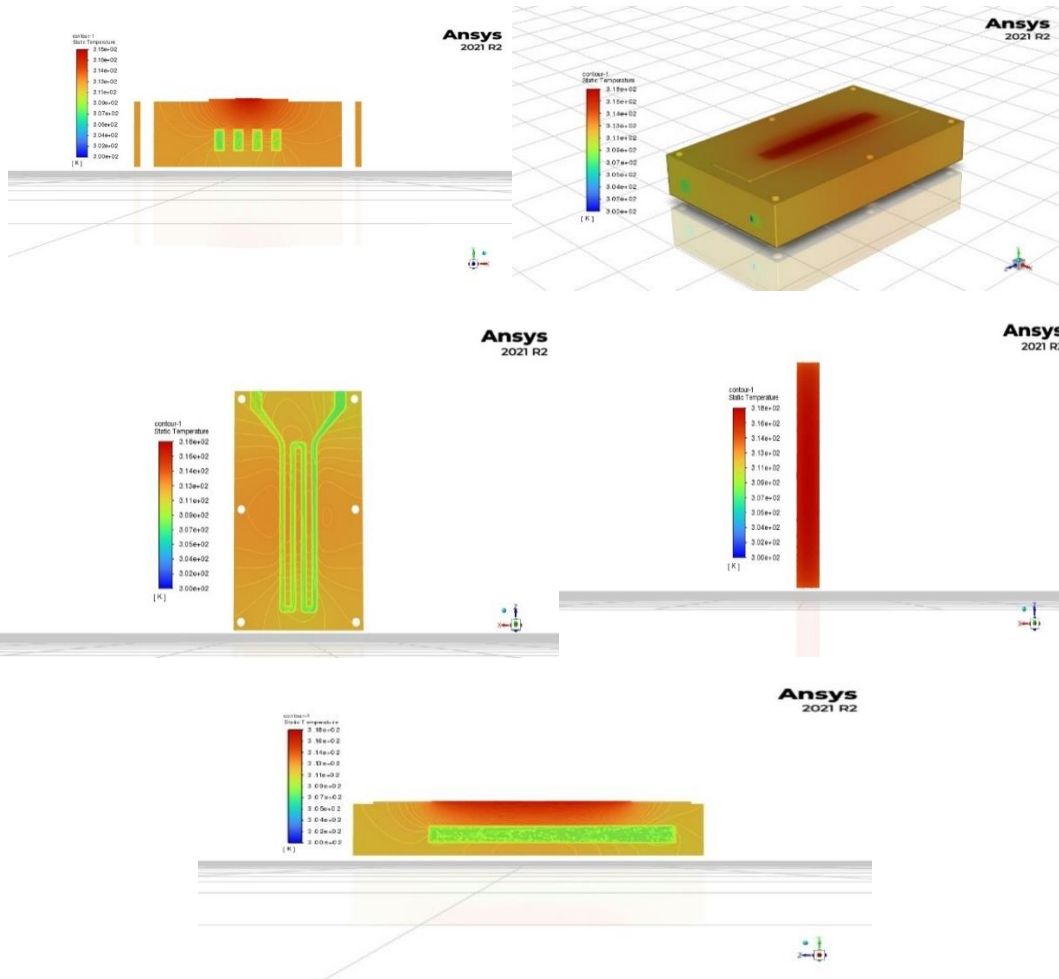
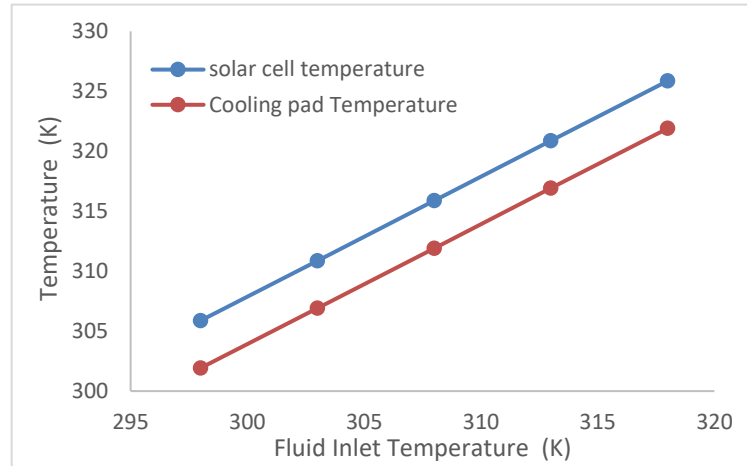
if (toggle1){
  digitalWrite(2,HIGH);
  digitalWrite(3,HIGH);
  digitalWrite(4,HIGH);
  digitalWrite(5,HIGH);
  digitalWrite(6,LOW);
  toggle1 = 0;
}
else{
  digitalWrite(2,LOW);
  digitalWrite(3,LOW);
  digitalWrite(4,LOW);
  digitalWrite(5,LOW);
  digitalWrite(6,HIGH);
  toggle1 = 1;
}
}

```

# Appendix D Inlet Temperature Effect and Temperature Contours

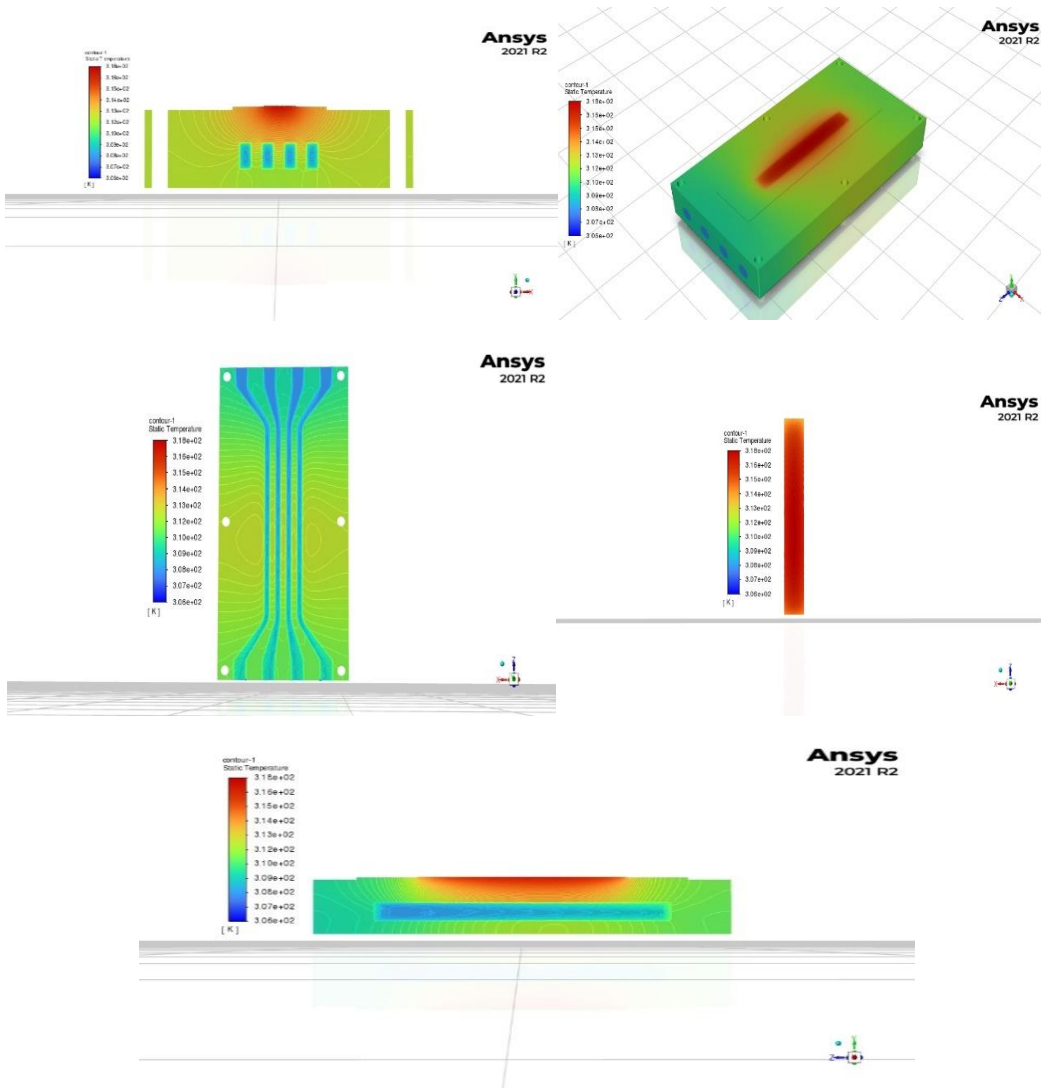
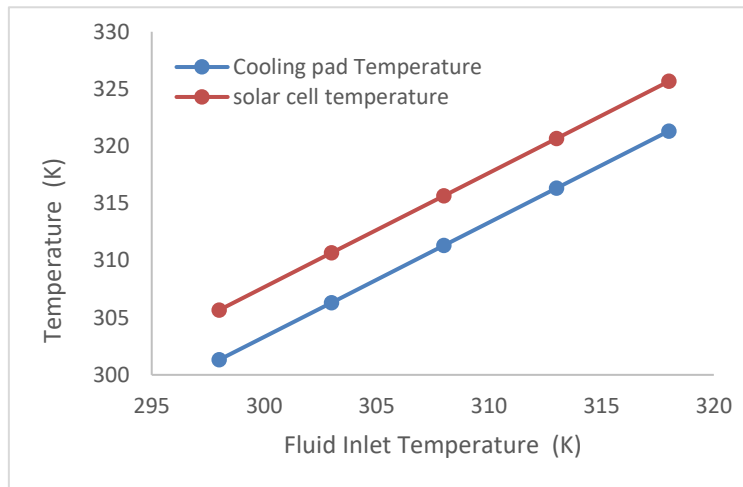
Temperature contours and the effect of cooling water inlet temperature increase for the three designs.

## D.1 Conventional Design

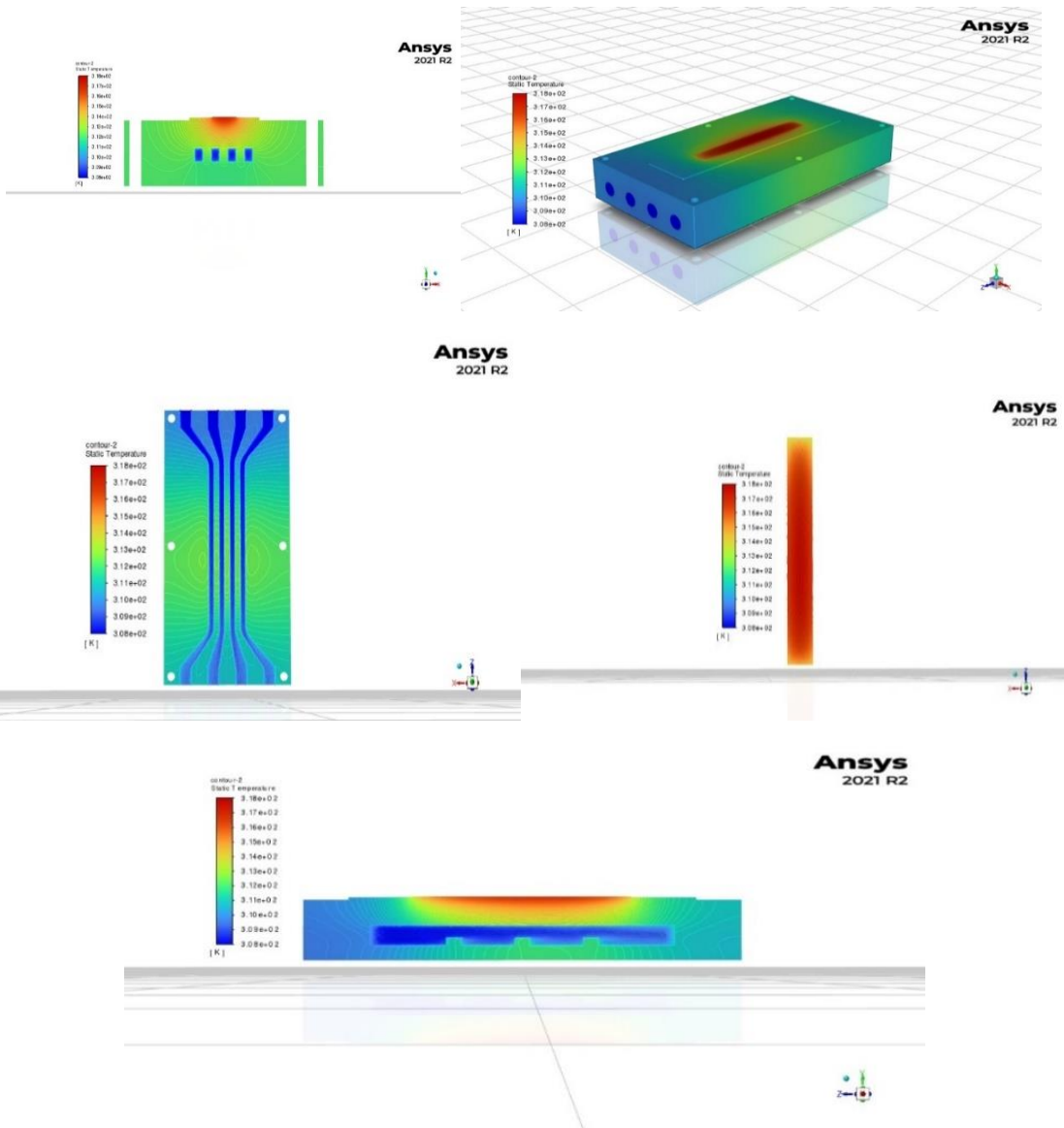
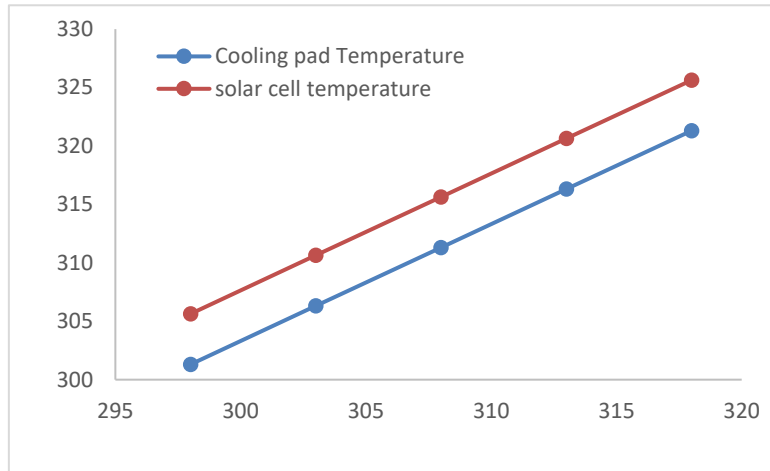




## D.2 Parallel Design Without Baffles



### D.3 Parallel Design with Baffles



## Appendix E Simulation Rerun Comparison

Rerun results comparison based on *Number of time steps/ Time step size (s)/ Maximum iteration per time steps per.* Where 200/0.04/100 stands for Number of time steps/ Time step size (s)/ Maximum iteration per time steps per.

